PROCESSING AND CHARACTERIZATION OF NEW $(M_xNb_{1-x})_2AlC$, $(M_xV_{1-x})_2AlC$, AND $(M_xV_{1-x})_3AlC_2$ MAX PHASE SOLID SOLUTIONS WITH M = Ti, Fe, Co, Ni

A Dissertation

by

ZEYI TAN

Submitted to the Graduate and Professional School of
Texas A&M University
in partial fulfillment of the requirements for the degree of

DOCTOR OF PHILOSOPHY

Chair of Committee,	Miladin Radovic
Committee Members,	Raymundo Arroyave
	Ankit Srivastava
	Micah J. Green
Head of Department,	Ibrahim Karaman

May 2022

Major Subject: Materials Science and Engineering

ABSTRACT

Over the last two decades, a family of ternary carbides and nitrides commonly referred to as MAX phases has gathered tremendous attention of scientists and engineers. Thanks to their layered crystal structure consisting of by ceramic-like M-X layers interleaved with metal-like A layers, MAX phases combine properties of both metals and ceramics. In addition, alloying with other elements on M, A, and X sites provide the extra potential for optimizing and tailoring their properties for various applications.

Among all MAX phases, Nb-Al-C and V-Al-C are of special interest in this dissertation work for two reasons. First, they are considered to be good candidates for high-temperature applications, and secondly, previous computational results suggest that they can accommodate more late transition metals in solid solution, unlike much more studied Ti-Al-C MAX phases. Among all other reaction sintering techniques used in fabricating MAX phases, Pulse Electric Current Sintering (PECS) was selected for synthesis of Nb- and V-based MAX phases in this study, because of rapid heating and cooling rates and easy operational control of the grain size in the sintered material.

This dissertation starts by investigating how excess of Al powder used in synthesis of Nb_2AlC affects its final phase composition. Once obtaining the optimal sintering conditions of synthesizing phase-pure Nb_2AlC, the recipe was employed to fabricate phase-pure $(Ti_xNb_{1-x})_2AlC$ solid solutions with x = 0-1. The microstructure and room temperature mechanical properties of $(Ti_xNb_{1-x})_2AlC$ solid solutions were also further characterized. Motivated by introducing magnetism into MAX phases, the research

expanded to study of the phase stability of the Nb-Al-C system alloyed with Fe, Co, and Ni. Although no quaternary carbides with MAX phase structure were detected in Nb-Fe-Al-C, Nb-Ni-Al-C and Nb-Co-Al-C systems, we report for the first time on formation of new η-carbides in those systems.

Since $(V_xTi_{1-x})_2AlC$ solid solutions have been successfully synthesized and characterized in the past, the focus of this study is on (i) synthesis of higher order MAX phase solid solutions from V-Ti-Al-C system, and (ii) synthesis and characterization of $(V_xFe_{1-x})_2AlC$. Herein we report for the first time on synthesis of $(V_xTi_{1-x})_3AlC_2$ solid solution with x up to 0.9, which is particularly important because V_3AlC_2 does not exist. On the other hand, unlike in the case of Nb-Fe-Al-C system, we showed formation of $(V_xFe_{1-x})_2AlC$ with x=0.03 and characterized its magnetic properties.

High-entropy MAX phase is a new emerging area starting from 2020. In the remainder of this dissertation, the current research progress on this topic and future research directions are discussed in more detail.

DEDICATION

To my parents, my friends and all people helped me.

ACKNOWLEDGEMENTS

I would like to express the deepest appreciation to my committee chair Dr. Miladin Radovic for his continuous guidance and support during my years as a doctoral student. Without his innovative ideas and persistent tutoring, I could not have imagined pursue of Ph.D. degree would be such a great experience.

I also would like to thank my committee members Dr. Raymundo Arroyave, Dr. Ankit Srivastava, and Dr. Micah Green for giving me helpful suggestions during my Ph.D. work.

Support of this thesis research by U.S. National Science foundation through grants #1729350 and #1760859 is greatly appreciated.

I truly appreciate all help from collaborators from Texas A&M University and other research institutes. I want to thank Dr. Anup Bandyopadhyay from Materials Development and Characterization Centre at Texas A&M University for his instructions on how to use PECS, tube furnace, and sample preparation for SQUID. Thanks go to Dr.Sisi Xiang, Dr. Yordanos Bisrat, Dr. Winson Kuo, Dr. Andrew Mott from Materials Characterization Facility at Texas A&M University for the HR-S/TEM images collection, training of SEM, EDS, EBSD, and WDS. My great appreciation also goes to Dr. Prashant Singh, Texas A&M University, for his DFT simulation work. I also want to thank Dr. Maxim Sokol, Tel Aviv University, and Dr. Michel Barsoum, Drexel University for their help on paper preparation.

Thanks also go to my teammates and my colleagues. I want to thank Dr. Yexiao Chen, Dr. Huili Gao, Vrushali Kotasthane, , Oscar Huang, Marco Martinez, Dong Gi Ha,

Zhiqiang Zhan，Xiaofei Zhao, Huaixuan Cao, Ian Echols, Dustin Holta, Wanmei Sun, Evan Prehn and Muhammad Anas who made my stay and study more enjoyable and provided me with useful perspectives on my research. In addition, I want to express my sincere gratitude to all faculty and staff in Materials Science and Engineering Department for making my study in Texas A&M University a great learning experience.

Last but not least, I express my deepest gratitude to my mother and father for their encouragement, support, and patience during all these years. A lot of thanks to my fiancée Weiyi Zhou for her understanding and tolerance in these years. I will never forget you staying with me until 4 am in MCF while I was collecting SEM images for my thesis research - that's the most beautiful picture I will remember in my life.

CONTRIBUTORS AND FUNDING SOURCES

Contributors

This work was supervised by a thesis committee consisting of Professors Radovic, Arroyave and Srivastava of the Department of Materials Science and Engineering, and Professor Green of the Department of Chemical Engineering.

The Wavelength Dispersive Microprobe (WDS) data represented in Chapter 2 was collected in part by Dr. Andrew Mott of the Materials Characterization Facility. The Transmission Electron Microscope (TEM) images and High-Resolution Scanning Transmission Electron Microscopy (HR-S/TEM) images shown in Chapter 2 was collected by Dr. Maxim Sokol of Drexel University and Dr. Winson Kuo of the Materials Characterization Facility, respectively. The RUS data represented in this work were collected by Dong Gi Ha of Texas A&M University. The HR-S/TEM images shown in Chapter 5 were collected by Dr. Jun Lu of Linköping University, and the magnetic measurement was conducted in part by Dr. Anup Bandyopadhyay of Texas A&M University. DFT simulation was conducted by Dr. Prashant Singh of Ames Laboratory. All HR-S/TEM images represented in Chapter 6 were collected by Dr.Sisi Xiang of Materials Characterization Facility. All other work conducted for the thesis was completed by the student independently.

Funding Sources

This work was supported by US National Science Foundation through grants #1729350 and #1760859 awarded to Texas A&M University.

NOMENCLATURE

2D	Two-dimension
AFM	Anti-ferromagnetic
Al_2O_3	Alumina
ADF	Annular Dark Field
BSE	Backscatter Electron
E	Elastic Modulus
EDM	Electrical Discharge Machining
EDS	Energy Dispersive Spectroscopy
FE	Field Emission
FM	Ferromagnetic
FIB	Focused Ion Beam
HAADF	High-angle Annular Dark Field
HE	High Entropy
HR-S/TEM	High Resolution Scanning Transmission Electron Microscopy
HIPing	Hot Isostatic Pressing
HP	Hot Pressing
MAX	$M_{n+1}AX_n$ (n = 1,2,3)
ME	Medium Entropy
MTS	Materials Test System
NM	Non-magnetic
PM	Paramagnetic

PBE	Perdew, Burke, and Ernzerhof
PECS	Pulse Electric Current Sintering
PECSed	Pulse Electric Current Sintered
RUS	Resonant Ultrasound Spectroscopy
SEM	Scanning Electron Microscopy
SQUID	Superconducting Quantum Interference Device
SPS	Spark Plasma Sintering
SPSed	Spark Plasma Sintered
SQS	Special Quasi-random Supercell
T	Temperature
TDOS	Total Density of States
TEC	Thermal Expansion Coefficient
TEM	Transmission Electron Microscopy
UHP-Ar	Ultra-high Purity Argon
VASP	Vienna *Ab-initio* Simulation Package
WDS	Wavelength Dispersive Spectroscopy
XRD	X-ray Diffraction

TABLE OF CONTENTS

Page

LIST OF FIGURES

Page

LIST OF TABLES

Page

1. INTRODUCTION

1.1. Properties and Applications of MAX Phases

MAX phases are a family of nano-laminated carbides and/or nitrides with a general chemical formula of $M_{n+1}AX_n$ (n = 1-3), where M is an early transition metal, A stands mostly for group 13-16 elements, and X refers to carbon and/or nitrogen [1–4]. MAX phases crystallize in the hexagonal *P6₃/mmc* structure with layers of strongly bonded M_6X octahedra that are interleaved with layer of weakly bonded A elements. Based on the number of multiple M layers in between the separating A layers, MAX phases can be categorized as M_2AX (211), M_3AX_2 (312) and M_4AX_3 (413), **Figure 1.1** [5]**.** The corresponding crystal structures observed by atomic resolution TEM are shown in **Figure 1.2**. Noted here, a higher-order (n > 3) MAX phase was discovered in 2010 [6], where 5 bright M-layers were interleaved by separating dark A-layers (**Figure 1.2-d**).

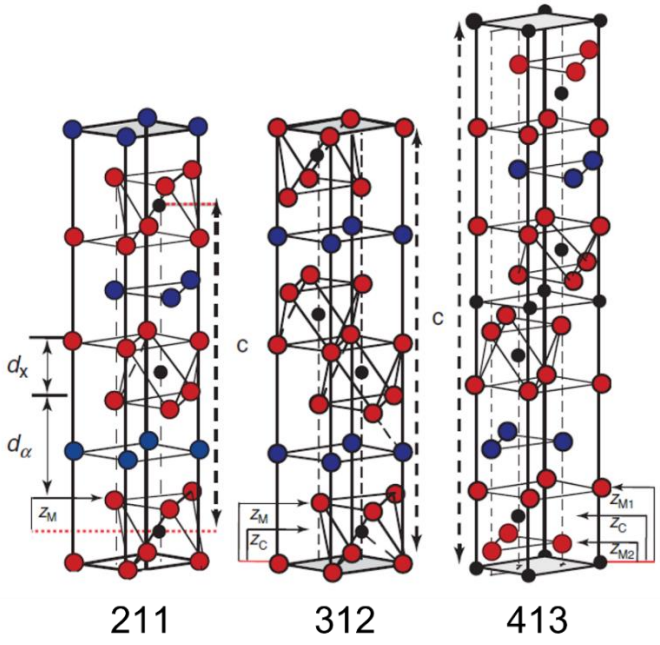

Figure 1-1 Unit cells of 211, 312, and 413 MAX phases, where M, A, and X atoms are represented as red, blue, and black balls, respectively, adapted from [5]**.**

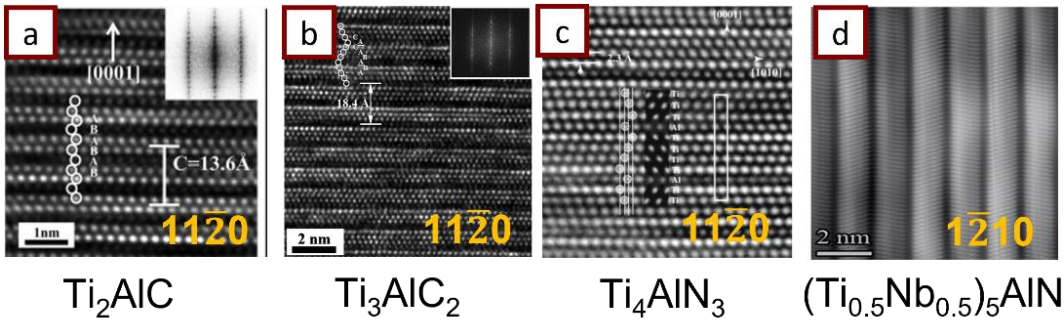

Figure 1-2 Atomic crystal structures of (a) 211: Ti_2AlC; (b) 312: Ti_3AlC_2; (c) 413: Ti_4AlN_3; and (d) 514: $(Ti_{0.5}Nb_{0.5})_5AlN_4$, adapted from [4,6,7].

Al	Si	P	S
Ti_2AlC V_2AlC Cr_2AlC Nb_2AlC Ta_2AlC Ti_2AlN Zr_2AlC Hf_2AlC Ti_3AlC_2 Ta_3AlC_2 Zr_3AlC_2	Ti_3SiC_2 Ti_4SiC_3 $Ti_5Si_2C_3$ $Ti_7Si_2C_5$ Hf_3AlC_2 $Ti_5Al_2C_3$ Ti_4AlN_3 Ta_6AlC_5 Ta_4AlC_3 Nb_4AlC_3 V_4AlC_3	V_2PC Nb_2PC	Ti_2SC Zr_2SC $Nb_2SC_{0.4}$ Nb_2SC Hf_2SC
Ga	Ge	As	Zn
Ti_2GaC V_2GaC Cr_2GaC Nb_2GaC Mo_2GaC Ta_2GaC Mn_2GaC Ti_2GaN Cr_2GaN V_2GaN Ti_3GaC_2 Ta_4GaC_3 Ti_4GaC_3	Ti_2GeC V_2GeC Cr_2GeC Nb_2GeC Ti_3GeC_2 Ti_4GeC_3	V_2AsC Nb_2AsC	Ti_2ZnC Ti_3ZnC_2 Ti_2ZnN V_2ZnC
In	Sn	Precious metals	Others
Sc_2InC Ti_2InC Zr_2InC Nb_2InC Hf_2InC Ti_2InN Zr_2InN Ti_3InC_2	Ti_2SnC Hf_2SnN Zr_2SnC Ti_3SnC_2 Nb_2SnC Zr_3SnC_2 Hf_2SnC Hf_3SnC_2 Lu_2SnC Ti_7SnC_6	Mo_2AuC Ti_3AuC_2 Ti_3IrC_2	Ti_2CdC
Tl	Pb		
Ti_2TlC Zr_2TlC Hf_2TlC Zr_2TlN	Ti_2PbC Zr_2PbC Hf_2PbC		

Figure 1-3 List of ternary MAX phases found to date. Image was adapted from [8].

Regarding MAX phase's history, most of 211 phases and two 312 phases were discovered by Nowotny's group in 1967 – 1970. Between 1996 and 1999, Dr. Barsoum *et al.* found the combination of metallic and ceramic properties of these phases and named them as $M_{n+1}AX_n$. Up to now, over 80 ternary MAX phases have been experimentally synthesized (**Figure 1.3**) [8]. Among them, Ti_2AlC [9], Ti_3AlC_2, Ti_3SiC_2, and Cr_2AlC have been investigated extensively so far. However, considerably less studies focused on Nb_2AlC and V_2AlC, and even less on Nb_4AlC_3 and V_4AlC_3 as potentially the most refractory MAX phases [10–12] In addition, Nb_3AlC_2 and V_3AlC_2 have never been synthesized, although computational studies suggests that V_3AlC_2 is could be a stable phase [13].

MAX phases are attracting more attention since they show a very unique combination of ceramic- and metallic-like properties. For example, they are elastically stiff like a corresponding binary transition metal carbides/nitrides with good thermal and electrical conductivities. In addition, MAX phases are resistant to thermal shocks and have outstanding corrosion and oxidation resistance at high temperatures (**Figure 1.4-a**), making them as good candidates for high temperature applications [3,4,14,15]. In contrast to traditional ceramic materials, MAX phases are readily machinable with simple tools such as a hack-saw (**Figure 1.4-b**) [4,16,17]. This integration of properties can be attributed to MAX phase's unique layered atomic structure, where M-X layers which are connected by mostly strong covalent M-X bonds are intercalated A-layers via weaker metallic M-A bonds.

Figure 1-4 (a) Ti_2AlC-based heating element at 1450 °C in air; (b) Articles made by MAX phases. Images were adapted from [5]**.**

1.2. Nb- and V- based MAX Phase Solid Solutions

One of the fascinating aspects of MAX phases is that they provide a plenty of potential opportunities for alloying them with either single or multiple elements on M, A and X sites to tune their properties. The list of the MAX phases solid solution synthesized thus far incudes not only elements that normally form pure (or end-member) MAX phases (**Figure 1.3**), but also some that do not form pure MAX phases, such as late transition metals and lanthanides (**Figure 1.5**). For instance, alloying Mn on the M-site of Cr_2AlC would introduce the magnetism into final sample and the evidence of Mn existing on the M-site is shown in **Figure 1.6** [18]; by substituting a secondary element (Ge, Ga, etc.) on the A-site, the resultant MAX phase solid solutions have noticeable advancement in mechanical properties [4,19]; in the case of $Ti_{n+1}AN_n$, replacing N atoms by C atoms on the X-site resulted in an increase in both bulk moduli and lattice parameters [20].

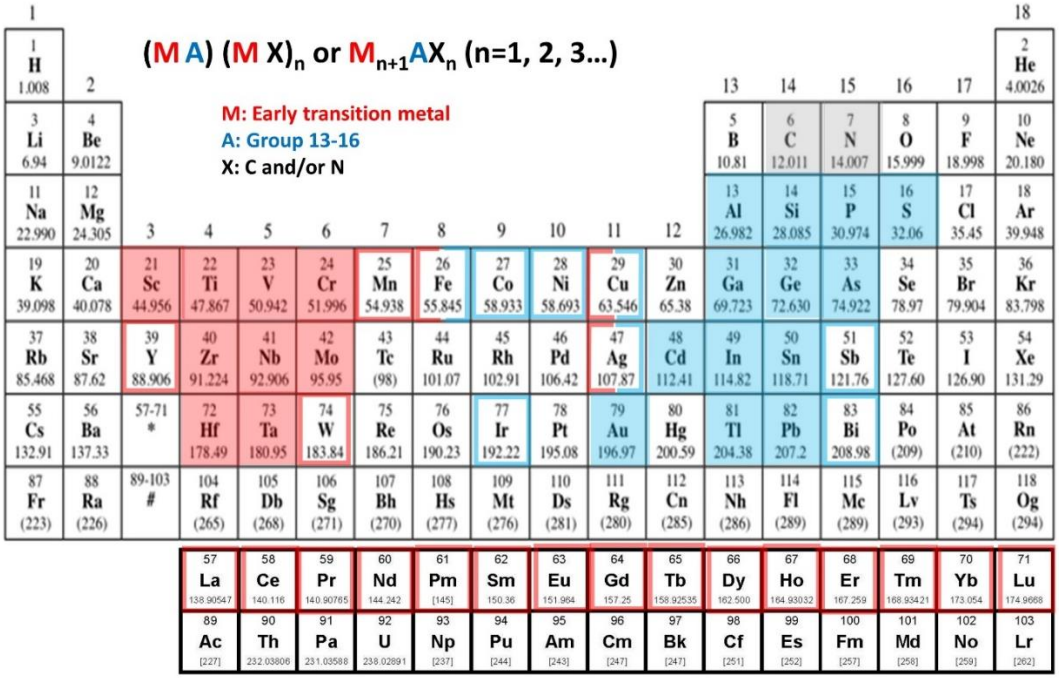

Figure 1-5 Reported M-elements (highlighted with solid red boxes) and A-elements (highlighted with solid blue boxes) in the periodic table. The elements marked with open red boxes and open blue boxes are reported can be alloyed on the M-site and A-site, respectively.

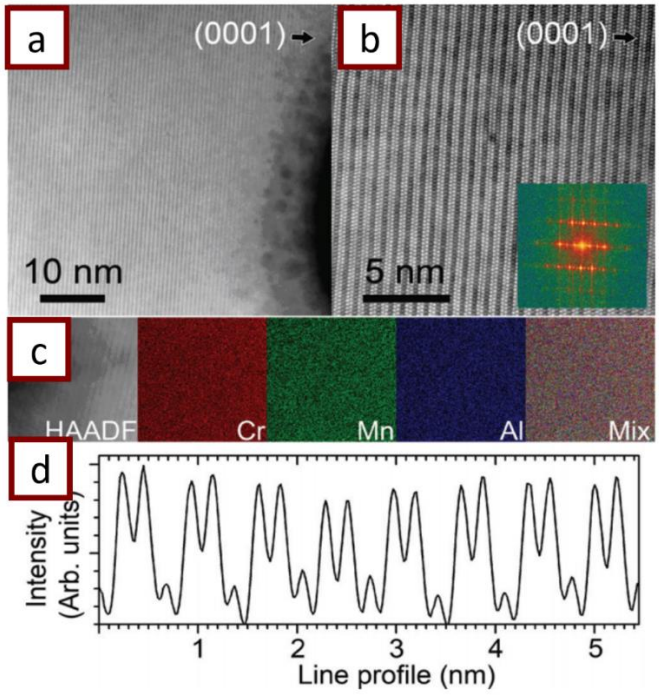

Figure 1-6 HAADF-S/TEM of $(Cr,Mn)_2AlC$ along (0001) under (a) low magnification and (b) high magnification; (c) is the corresponding EDX mapping with the (d) line profile, adapted from [18]**.**

In terms of Nb-based MAX phase solid solutions, a very few studies have been reported thus far. $(Nb_xTi_{1-x})_2AlC$ was of particular interest since Alexander *et al.* showed that mixing 4 at.% Nb with commercial Ti_2AlC and heated the mixture at 900^oC for 120 hours [21] resulted in samples that form more homogenous and uniform protective alumina oxide layer than the Nb-free sample. The most studied composition is $(Nb_{0.5}Ti_{0.5})_2AlC$ [22]. Other synthesized MAX phase solid solutions in Nb-Al-C include: $(Nb_xTi_{1-x})_2AlC$ with x = 0.04, 0.07 [23], $(Nb_xZr_{1-x})_2AlC$ with x = 0.2 and 0.8 [24], $(Nb_xV_{1-x})_2AlC$ with x=0.5 [24], $(Nb_xSc_{1-x})_2AlC$ with x = 0.66 (**Figure 1.7**) [25], $(Nb_xTa_{1-x})_4AlC_3$ with x = 0.05-0.25 [26,27], $(Nb_xTi_{1-x})_4AlC_3$ with x = 0.1-0.3 [28], $(Nb_{0.5}V_{0.5})_4AlC_3$ [24], and $(Nb_xZr_{1-x})_4AlC_3$ with x = 0.2 [29]. In some cases, alloying the second element on the M-site of parent Nb-based MAX phase results in an enhancement of mechanical properties. For example, the flexural strength, fracture toughness, Young's modulus and Vickers hardness of $(Nb_x,Ta_{1-x})_4AlC_3$ measured at RT were increased 45%, 8%, 18%, and 80%, respectively, when compared to Nb_4AlC_3 (**Figure 1.8**) [26]. While in other case, i.e., $(Ti_{0.5}V_{0.5})_2AlC$, the bulk modulus was reported to lower than the one of its end members [23]. However, to the best of our knowledge, no $(Ti_xNb_{1-x})_2AlC$, or any other M-site solid solution in Nb-Al-system has been synthesized and systematically characterized in the whole range from 0 to 1. This is particularly important for eventual high temperature applications of MAX phase solid solutions.

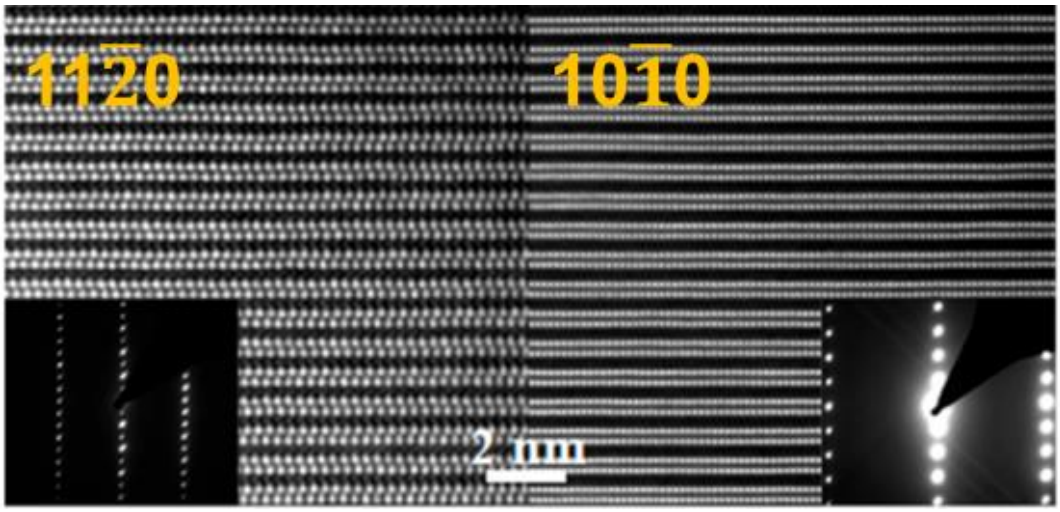

Figure 1-7 HR-S/TEM of $(Nb_{2/3},Sc_{1/3})_2AlC$, adapted from [25].

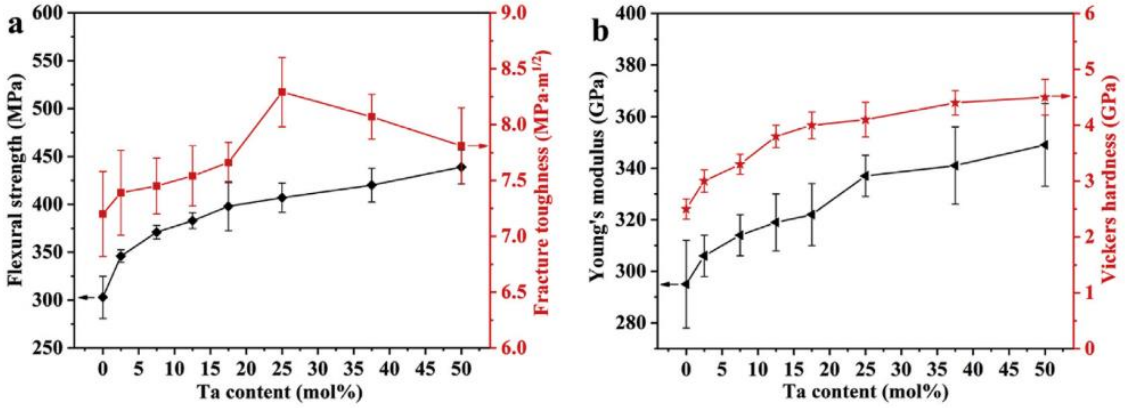

Figure 1-8 The changing trend of RT (a) Flexural strength and fracture toughness and (b) Young's modulus and Vickers hardness over 0-50 mol% Ta content. Images were adapted from [26].

Synthesis of phase-pure V_2AlC from elemental powders has been reported elsewhere [30–33]. With respect to V-based MAX phase solid solutions, a number of studies have been reported of $(V,Ti)_2AlC$ and $(V,Cr)_2AlC$ with full range of compositions [34–37]. Replacement of V atoms by Ti atoms in $(V,Ti)_2AlC$ resulted in a lower bulk modulus when compared to those its end members [23]; whereas the Vickers hardness of $(V,Cr)_2AlC$ increased linearly with increasing V content (see **Figure 1.9**) [35]. Other

synthesized MAX phase solid solutions V-Al-C system also include: $(V_xMn_{1-x})_2AlC$ with x = 0.96 [38], $(V_xSc_{1-x})_2AlC$ with x = 0.33 [39], $(V_xZr_{1-x})_2AlC$ with x = 0.66 [40], $(V_xCr_{1-x})_3AlC_2$ with x = 0.5 [13], $(V_xCr_{1-x})_4AlC_3$ with x = 0.5 [13], and $(V_xMo_{1-x})_5AlC_4$ with x = 0-1 [41]. Reported $(V_xMn_{1-x})_2AlC$ with x = 0.96 [38] is of the special interest for their study because of the reported magnetic properties.

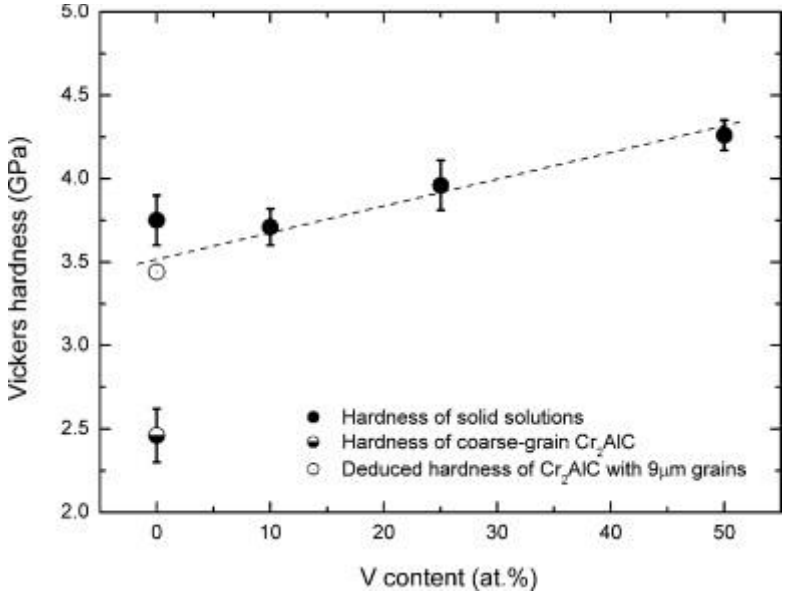

Figure 1-9 Vickers hardness of $(Cr_{1-x}V_x)_2AlC$ solid solutions at a load of 30 kgf as a function of V content. The dash line represents the linear fit of the deduced hardness of Cr_2AlC and those of V-containing solid solutions, adapted from [36].

It has to be noted here that some MAX phase solid solutions can also include elements that do not form stable MAX phase end members. For instance, Cr_3AlC_2 and V_3AlC_2 do not exist, while $(V_{0.5}Ti_{0.5})_3AlC_2$ and $(V_{0.5}Cr_{0.5})_3AlC_2$ were fabricated experimentally [13,24]. To date, only one composition of $(V_{0.5}Ti_{0.5})_3AlC_2$ was experimentally synthesized in bulk [24] while the end member V_3AlC_2 was only predicted to exist computationally. On the other hand, $(Ti_xNb_{1-x})_3AlC_2$ with x = 0-1 was only computationally studied as well while its end member Nb_3AlC_2 is even computationally

not stable [42]. Driven by adding new members to experimentally prepared MAX phases, phase stability of $(V_xTi_{1-x})_3AlC_2$ and $(Nb_xTi_{1-x})_3AlC_2$ MAX phases were also investigated experimentally.

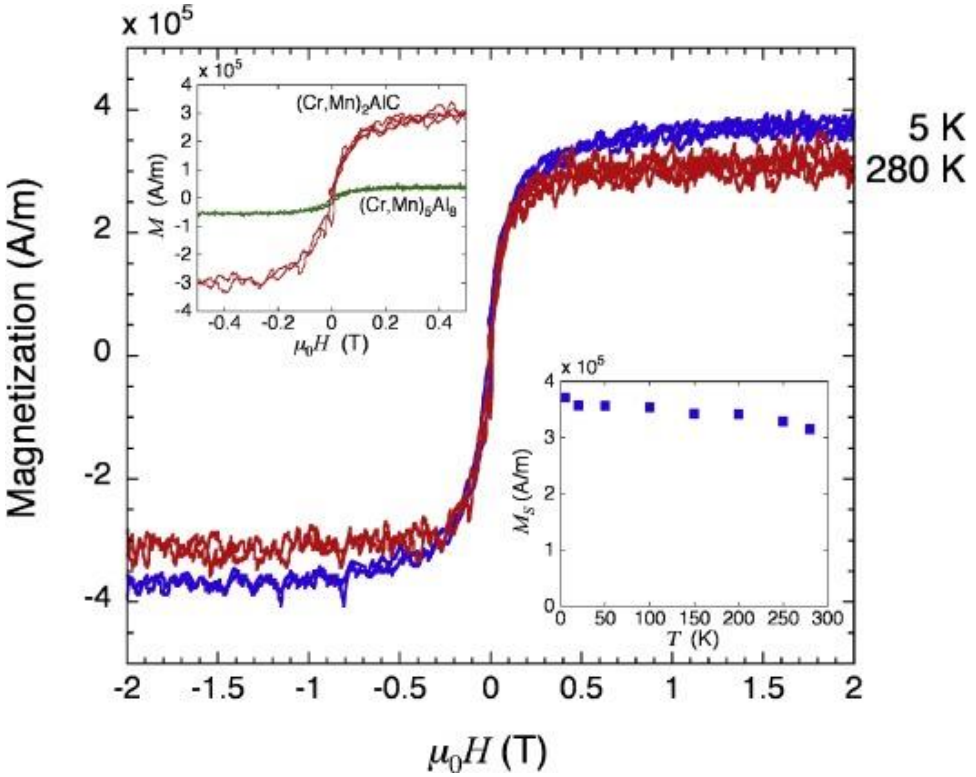

Figure 1-10 Magnetic response of $(Cr,Mn)_2AlC$ thin film with the magnetic field applied parallel to the film plane. At 280 K, a magnetic signal is observed. Top inset shows the low-field in-plane magnetization of $(Cr,Mn)_2AlC$; Bottom inset represents the relationship between temperature and saturation magnetization of $(Cr,Mn)_2AlC$ at 4 T. Images were adapted from [18].

With respect to achieving new properties of MAX phases, potential of making them magnetic is of special interest since they can be subsequently etched into their 2D derivates MXenes, impacting considerably many applications, including data storage and spintronic devices [43]. Fe-based MAX phases, i.e., Fe_2AlC and Fe_2SiC, were the earliest members that were investigated on magnetic properties by simulation work [44], and showing that both can be at best metastable, but these phases have never been

experimentally synthesized thus far. Mockute *et al.* subsequently alloyed Cr_2AlC with Mn in the thin-film form with a stoichiometry of $(Cr_{0.84}Mn_{0.16})_2AlC$ by magnetron sputtering (**Figure 1.10**) [45]. However, the magnetic properties of this solid solution were not analyzed until they obtained the highest alloying level of Mn in $(Cr_{1-x}Mn_x)_2AlC$ of x = 0.2 [18]. $(Cr,Mn)_2AlC$ as a first synthesized magnetic MAX phase displayed a significant magnetic signal at and below the room temperature, although lack of magnetization hysteresis indicated that the magnetic moments were either canceling each other out or randomly oriented without an applied field [46,47]. Similar to $(Cr,Mn)_2AlC$, Lin *et al.* synthesized the bulk $(Cr,Mn)_2GaC$ and showed that up to 50% M-sites were substituted by the additive, **Figure 1.11-a** [48], and the parent MAX phase Cr_2GaC was transformed from a non-magnetic material to a ferrimagnetic state, **Figure 1.11-b**. Apart from solid solutions, Mn_2Ga, which extends the family of MAX phases, was synthesized by Ingason *et al.* in thin film [49]. To gain more further insights into its magnetic properties, Dahlqvist *et al.* [50] and Ingason *et al.* [51] performed various measurements on this materials. They found that Mn_2GaC presented FM signals when the temperature was below 230 K. In addition, the magnetism is anisotropic with a long range magnetic order [51]. Triggered by the formation of Mn_2GaC, the solid solutions $(Mo_{0.5}Mn_{0.5})_2GaC$ [52] and $(V,Mn)_3GaC_2$ [53] were fabricated as thin film later.

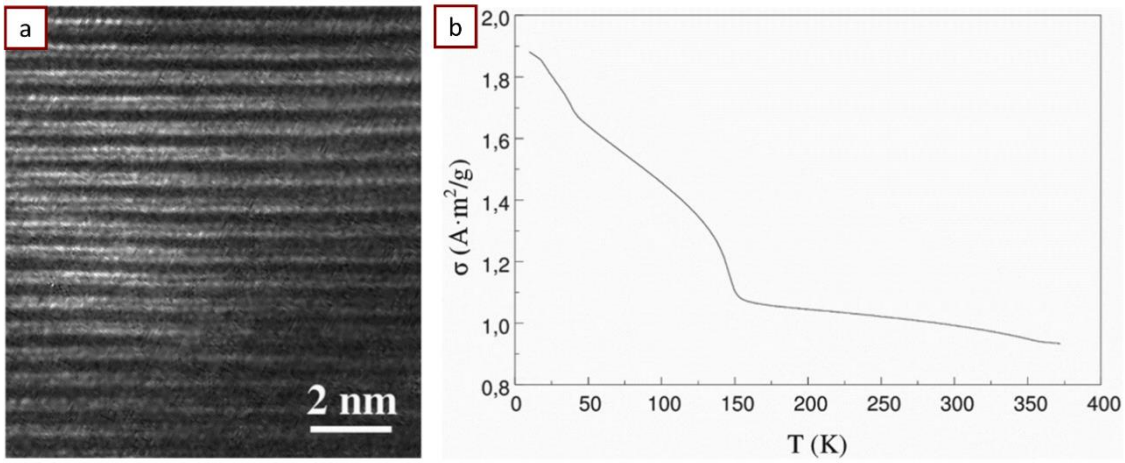

Figure 1-11 (a) Nanolaminated structure of $(Cr,Mn)_2GaC$; (b) Dependence between specific magnetic moment and temperature, showing evidence for magnetic transitions at 38 and 153 K. Images were adapted from [46]**.**

However, only a few studies have reported about alloying MAX phases with Fe, Ni and Co either on M-site or A-site. Most recently, Huang *et al.* showed that besides Fe, other magnetic elements, such as Co, Ni, and Mn or their combinations could also be intercalated as single-atom-thick A layers into V_2SnC [54]. The alloyed $V_2(A_xSn_{1-x})C$ (where A is a combination of Fe, Co, Ni, and Mn) showed the enhanced magnetism, **Figure 1.12**. No attempts on alloying potentially refractory MAX phase such as V_2AlC or Nb_2AlC with Fe, Ni, or Co has been reported thus far.

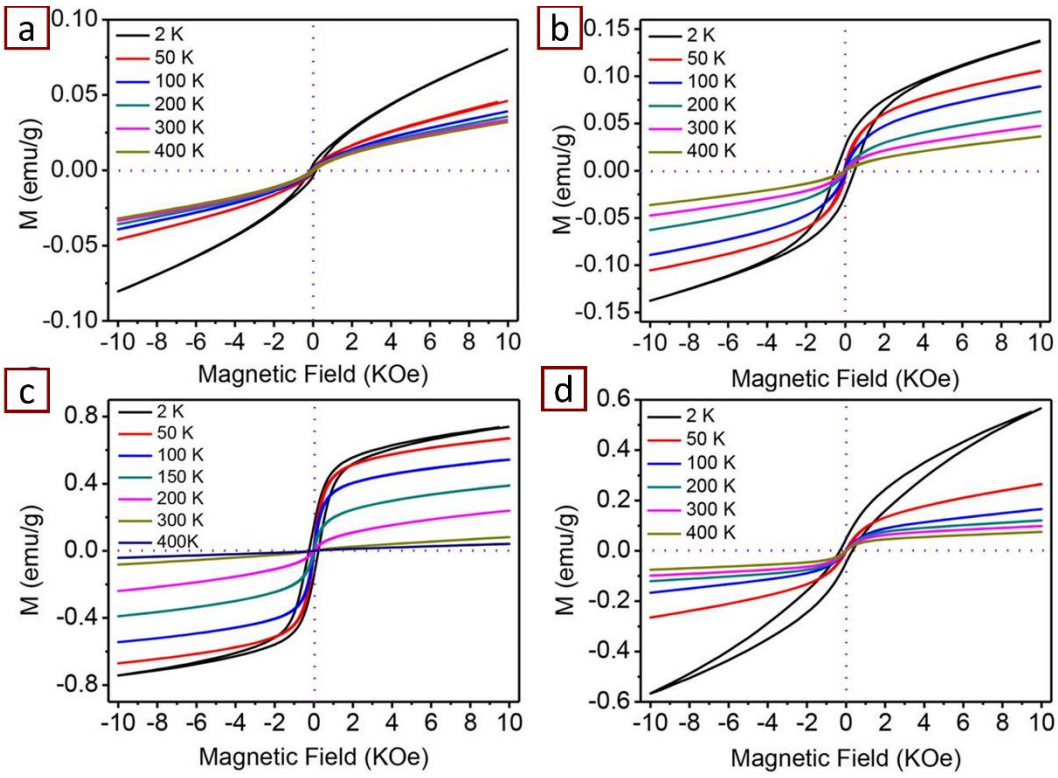

Figure 1-12 Magnetic hysteresis loops of (a) $V_2(Fe_xSn_{1-x})C$; (b) $V2(Fe_xCo_ySn_{1-x-y})C$; (c) $V_2(Fe_xCo_yNi_zSn_{1-x-y-z})C$; and (d) $V_2(Mn_xFe_yCo_zNi_nSn_{1-x-y-z-n})C$ at different temperatures in the range from −10 to 10 kOe. Images were adapted from [54]**.**

1.3. Research Objectives

The major objectives and rationale for this thesis research focusing on processing and characterization of new $(M_xNb_{1-x})_2AlC$, $(M_xV_{1-x})_2AlC$, and $(M_xV_{1-x})_3AlC_2$ MAX phase solid solutions with M = Ti, Fe, Co, Ni can be summarized as following:

1. ***Optimization of reaction sintering to fabricate phase pure, bulk Nb_2AlC from elemental powders using PECS*** as a more feasible way of obtaining phase pure Nb_2AlC. Note here that synthesis of phase pure V_2AlC from elemental powders has already been reported [30] and therefore it is not explored in this study.

2. ***Synthesis of $(Nb_xTi_{1-x})Al_2C$ with x=0-1 from elemental powders using PECS*** builds on the optimized method for synthesis of phase pure Nb_2AlC. Since alloying Ti_2AlC - the best-known MAX phase for high temperature structural applications - with more refractory Nb has been proposed as a possible way to improve its properties relevant to high temperature structural application, mechanical properties, and oxidation resistance of synthesized $(Nb_xTi_{1-x})Al_2C$ with x=0-1 has also been characterized. Note that effects of alloying Ti_2AlC with V on its mechanical properties has been characterized in the past and thus is not further investigated in this study.
3. ***Synthesis of $(V_xTi_{1-x})_3AlC_2$ MAX phase solid solutions*** for expanding composition of MAX phase that can be easily etched to 2D derivatives MXenes. Even after 10 year or extensive research on etching MAX phases to MXenes, only Ti_3AlC_2 MAX phase can be etched to corresponding MXenes with sizable yields, while etching of 211 MAX phases, including V-based ones is still very difficult and produces very small yields. The major challenge here is to achieve high degree of substitution of Ti with V in Ti_3AlC_2, since V_3AlC_2 MAX phases is thermodynamically unstable.
4. ***Extending functionality of Nb_2AlC and V_2AlC MAX phases*** by alloying them with magnetic transition elements such as Fe, Ni and Co and investigate their phase stability and magnetic properties. This study has been inspired by previsions cluster expansion calculations [55] suggesting sizeable stability of $(V,Fe)_2AlC$, $(V,Ni)_2AlC$ and $(V,Ni)_2AlC$ phase with a negative energy hull at 0 K. Previous

reports are purely on alloying Cr-based MAX phases with magnetic transition metals, and lack of any reported studies on alloying V_2AlC or Nb_2AlC with Fe, Ni, and Co.

5. ***Synthesizing and characterization of medium-entropy (ME) MAX phase $(Nb_{0.33}Ti_{0.33}V_{0.33})_2AlC$ $(Nb_{0.50}Ti_{0.25}V_{0.25})_2AlC$, $(Nb_{0.25}Ti_{0.50}V_{0.25})_2AlC$, and $(Nb_{0.25}Ti_{0.25}V_{0.50})_2AlC$, plus high-entropy (HE) $(Nb_{0.25}Ti_{0.25}V_{0.25}Cr_{0.25})_2AlC$ and $(Nb_{0.25}Ti_{0.25}V_{0.25}Ta_{0.25})_2AlC$.*** By far, all the works regarding ME/HE-MAX phases were done using selected elementary powders as starting materials, which led to forming many undesired competing phases and the resultant in poor phase purity of final products [56,57]. To solve this problem, the staring material used in this report were homemade highly-phase-pure Nb_2AlC, V_2AlC, Ti_2AlC, Cr_2AlC and Ta_2AlC aimed to avoid the formation of secondary phases.

2. EFFECTS OF EXCESS Al ON THE FINAL COMPOSITION OF Nb_2AlC SYNTHESIZED VIA PULSED ELECTRIC CURRENT SINTERING TECHNIQUE

2.1. Literature Review

$M_{n+1}AX_n$ (MAX) phases are a family of nano-laminated hexagonal carbides and/or nitrides with hexagonal *$P6_3/mmc$* crystal structure, where M is an early transition metal, A refers mostly to group 13-16 elements, and X stands for either C or N [2,8,58]. In general, MAX phases are refractory and have high stiffness [59], while some of them show outstanding corrosion and oxidation resistance at high temperatures [14,15] and even crack healing at elevated temperatures in oxidizing environments [60]. Unlike typical binary carbides and nitrides, MAX phases are easy to machine [2] and show an excellent thermal shock resistance [4], and an good damage tolerance [5]. In addition, they have good electrical and thermal conductivities, and mechanical properties [3,17,61,62]. Because of this interesting combination of properties, MAX phases are considered as good candidate materials for high-temperature structural applications and potential cladding materials in nuclear devices [2,63].

Out of more than ~160 MAX phases known to date [8], only a few of them, such as Ti_2AlC [64–66], Ti_3AlC_2 [67], Ti_3SiC_2 [68], and Cr_2AlC [69] have been investigated extensively. Even more, only a few published studies focused on Nb_2AlC as one of potentially the most refractory MAX phases thus far. Nowotny et al. were the first to report Nb_2AlC phase in the Nb-Al-C system [70]. They synthesized Nb_2AlC using arc melting of Nb, NbC, and Al_4C_3 at 1000^{o}C for 170 hours, but found a large amount of Nb-carbides

(NbC) and a shred of Nb-aluminides ($NbAl_3$) as secondary phases in all samples. Salama et al. synthesized successfully for the first time predominantly single-phase Nb_2AlC from NbC, Al, and C powder mixture with Nb:Al:C atomic ratio of 2.00:1.08:0.97 via hot isostatic pressing (HIPing) at 1600^oC under 100 MPa for 8 hours. Their EDS results showed that the Nb:Al:C atomic ratio in Nb_2AlC is close to 2.000:0.914:0.895, suggesting slight deficiency of Al and C [71]. Zhang et al. used different amounts of NbC, Nb, and Al corresponding to Nb:Al:C = 2:1:1 to reaction sinter bulk samples via hot-pressing at 1650 ^oC [72]. Even though they studied reaction mechanisms in the 600-1650 ^oC temperature range, they did not report many details on the phase purity of the final samples and the chemical composition on targeted Nb_2AlC. Afterward, self-propagating high-temperature synthesis (SHS) was employed to fabricate Nb_2AlC ternary carbides from Nb_2O_5, Al, and Al_4C_3 powder mixtures with different stoichiometries [73]. This study showed that increasing the amount of Al or Al_4C_3 increased the yield of Nb_2AlC phase effectively, while keeping aluminum amount close to the stoichiometric one in Nb_2AlC resulted in relatively large amount of Nb_4AlC_3, $NbAl_3$, and NbC as impurity phases [73]. Most recently, polycrystalline Nb_2AlC was reaction sintered via the Pulse Electric Current Slithering, PECS, (commonly, but inaccurately referred in the past as Spark Plasma Sintering, SPS) technique from the starting Nb, NbC and Al powder mixture corresponding to the Nb:Al:C atomic ratio of 2.0:1.2:1.0 [74]. However, neither the effect of adding excess Al in staring powders on phase purity and composition of the targeted Nb_2AlC phase, nor the reaction mechanisms were investigated in more detail in that study.

Brief literature review on synthesis of Nb_2AlC provided above shows that regardless of the reaction synthesis methods, no Nb_2AlC has been synthesized from the mixture of elemental powders, namely Nb, Al, and C, although this is more economical and more commonly used route for reaction sintering MAX phases nowadays [2,75,76]. In this paper, we report on reaction sintering of Nb_2AlC from the elemental powders using the PECS method. Microstructural characterizations and elemental analysis were conducted systematically to give insights into the reaction mechanisms during sintering. Effect of different amounts of excess Al in the starting powder mixtures on the phase purity of sintered samples and chemical composition of Nb_2AlC was investigated in more detail. It is well established by now that excess amount of Al has to be added to the starting elemental powder mixtures before reaction sintering to compensate for the loss of low melting-point Al due to its melting and its excessive volatilization before it reacts with other elements to form high melting-point intermediate compounds or final MAX phases [24,33,74,77,78]. However, if the addition of excess Al is not carefully balanced, it can result in a large amount of secondary phases and/or sub-stoichiometric Al amount in the MAX phase, as that was the case for Nb_2AlC in the previous study by Salama et al. [71]. Reaction sintering of Nb_2AlC was carried out in this study using PECS as this method has been proven as effective and fast for reaction sintering of other MAX phases [61,79–81]. Compared to other traditional fabricating techniques, the main advantages of using PECS are (i) rapid heating and cooling rate, as high as 1000 and 400 ^{o}C/min, respectively, and (ii) an operational control of final grain size of targeted materials [82]. Thanks to the locally heating due to direct current passing through the compacted powder [82–84], the

diffusion procedure is accelerated extensively. Moreover, densification and sintering can be accomplished simultaneously [85]. Given the above merits, the PECS technique is specially used for preparing refractory MAX phases, such as Nb_2AlC [74] and its derivative Nb_4AlC_3 [78].

2.2. Experimental Methods

Elemental powders of niobium (Alfa Aesar, -325 mesh, 99.8%), aluminum (Alfa Aesar, -325 mesh, 99.5%), and flake graphite (Alfa Aesar, 7-10 micron, 99%) were weighted in a molar ratio of 2.0:X:0.95, where X = 1.05, 1.10, 1.22 and 1.30, respectively. As discussed earlier, the different amounts of excess Al (i.e. 5, 10, 22 and 30%) were added to compensate for its loss during sintering, while the sub-stochiometric amount of C was used due to the sintering in graphite dies, which is the source of additional carbon during PECS. All mixtures were then ball-milled with ZrO_2 beads in a plastic jar at 300 rpm for 6 hours. The powder mixtures were cold-pressed in a 20 mm cylindrical steel die under a pressure of 100 MPa. The green bodies were sintered by PECS (SPS25-10, Thermal Technologies LLC, CA) at 1600 or 1650 ^oC for 30 min in ultra-high purity argon (UHP-Ar), using a 30 MPa pressure and a heating rate of 25 ^oC /min with a pre-load of 10 MPa during heating, Table 1. To investigate whether the annealing process after PECSing contributes to increasing the amount of targeted Nb_2AlC in the sintered samples, selected samples were heat-treatment in a tube furnace (GSL-1600X, MTI, CA) under the same soaking temperature for 4 hours in the flowing UHP-Ar. All samples in this study are labeled as “soaking temperature-excess Al at.%”, while suffix TF indicates PECSed bulk sample was additionally heat-treated is reported herein as in the tube furnace, Table 1.

Note here that the excess Al reported in Table 1 is the at.% of aluminum added in the powder mixture in excess to the stoichiometric Al content. For example, the sample with Nb:Al:C atomic ratios of 1:1.05:0.95 had 5 at.% of excess Al in the starting powder mixture.

Table 2-1 The molar ratios of Nb, Al, and C in the starting powder mixtures and sintering conditions for different samples reaction sintered in this study.

Sample	Excess Al (mol%)	PECS and Tube Furnace Soaking Temperature (ºC)	PECS Dwell Time (min)	Tube Furnace Soaking Time (hours)	Atomic Nb:Al:C ratio in starting powders
1600-5Al	5	1600	30	0	2:1.05:0.95
1600-10Al	10	1600	30	0	2:1.1:0.95
1600-10Al-TF				4	
1600-15Al	15	1600	30	0	2:1.15:0.95
1650-22 Al	22	1650	30	0	2:1.22:0.95
1600-22Al	22	1600	30	0	2:1.22:0.95
1600-22Al-TF				4	
1600-30Al	30	1600	30	0	2:1.30:0.95

The cross-section areas of all bulk samples were ground and polished down to 1 μm diamond paste. The X-ray Diffraction (XRD) was carried out using a D8-Focus X-ray diffraction (Bruker, Madison, USA) with a Cu Kα radiation (λ = 1.5406 Å) at 40 kV and 25 mA. The step size and time per step were 0.019° and 0.4 s, respectively. All XRD data were collected at 2θ angles ranging from 5° to 70°. Rietveld refinement of X-ray diffractograms was performed using TOPAS V4.2 (Bruker, Madison, USA) software to determine the weight fraction of each phase detected in a sample. The microstructures of all samples were analyzed on the polished cross-sections using a combination of Scanning Electron Microscopy, SEM, (FIB-SEM, Lyra-3 Model GMH, United States) and Field Emission SEM (FE-SEM, JEOL-7500, Japan). Both of these SEM and FE-SEM instruments were equipped with Energy Dispersion Spectrometer (EDS, Oxford, United

Kingdom). In addition, the quantitative elemental analysis, specifically, to determine the actual ratio between Nb and Al, was carried out using Wavelength Dispersive Spectroscopy (WDS, CAMECA, SXFive, United Kingdom) by averaging composition in at least five different points in each phase.

Transmission electron microscopy (TEM) sample was prepared using a focused ion beam (FIB) microscope (Strata DB235, FEI Company, USA), by milling out 20 × 2 × 15 μm lamella from the selected sample, which was then lifted out and Pt welded onto a copper TEM grid. Following the thinning procedure, the lamella was thinned further from the lift-out by milling away of alternating sides. Progressively gentler beams were used to finely polish the lamella and were thinned until small perforations were observed. FIB damage was then cleaned with a final polish using a 5 kV beam. General microstructural TEM imaging was performed in a field emission TEM (JEM-2010F, JEOL) operated at 200 kV. High-resolution scanning transmission electron microscopy, HR-STEM, images were obtained by Titan (ThermoFisher Scientific) at 300 kV. A 50 μm C2 aperture (camera length 73 nm) was used.

The elastic moduli were measured with Resonant Ultrasound Spectroscopy, RUS (Quasar RUSpec, Magnaflux, IL) at room temperature using the procedure described elsewhere [61,86]. We chose this technique because of its remarkable precision and repeatability in determining elastic constants [4,87]. RUS measures the resonant spectrum of the mechanical vibrations of a sample with known dimensions, mass, and geometry [86,88,89]. In our work, we placed a small disc with the diameter and the thickness of 20.95 mm and 3.31 mm, respectively, on three piezoelectric transducers. One of them

generated an elastic wave of constant amplitude and varying frequency that was further transmitted to the specimen, and the other two transducers detected the mechanical vibrations of the specimen. From the detected frequencies of the resonant peaks, a set of estimated elastic constants was determined using a multi-dimensional algorithm (Quasar RUSspec, Magnaflux, IL) for the sample with known dimensions and mass.

The Vickers hardness was measured at the cross-section of the sample with the best phase purity using microhardness tester LM 300AT (LECO, MI) under a load of 500 gram-force (gf). At least 20 points were indented, evaluated, and averaged. The Vickers hardness was calculated by the formula of $H = 1.8544*P/d_v^2$, where P (gf) is the applied load, and d_v (μm) is the average of the two diagonals of an indent [90]. The sample's density of sintered samples was measured by Archimedes' method described in more detail elsewhere [16,19].

2.3. Results and Discussion

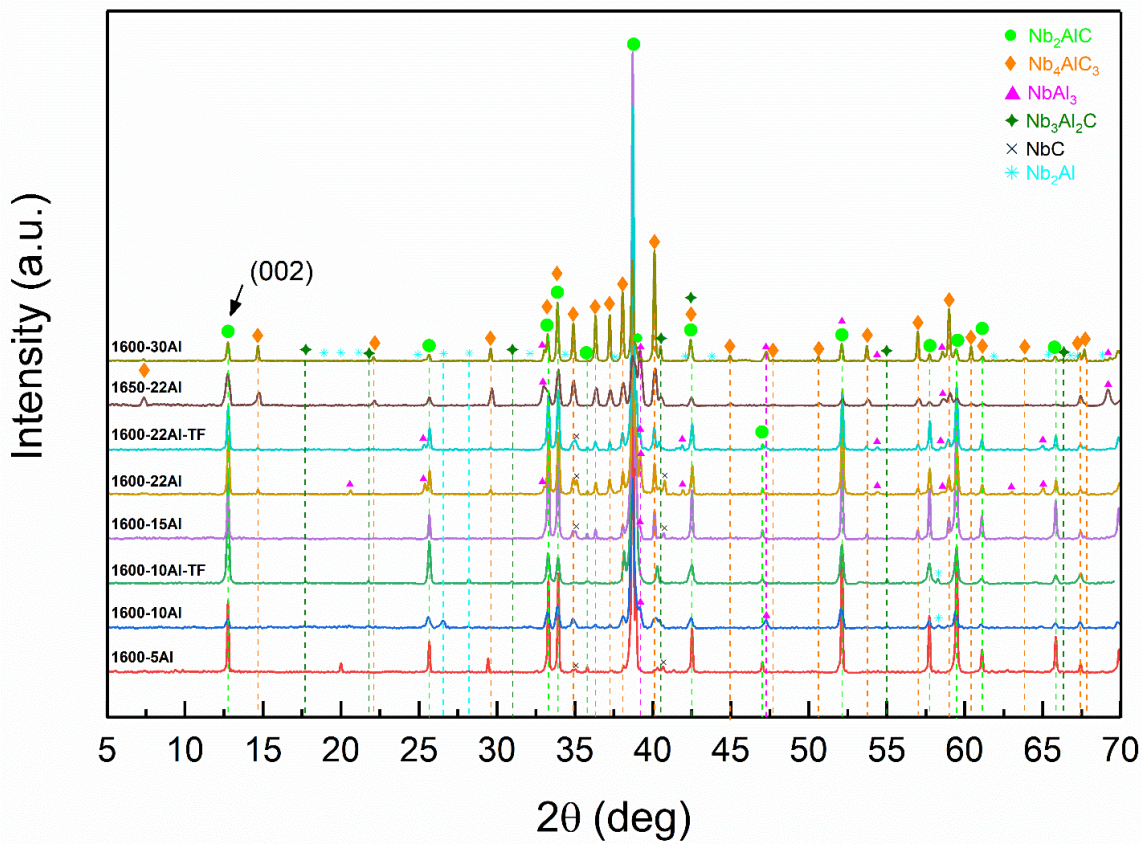

Figure 2-1 XRD patterns of "soaking temperature-x Al", where x = 5, 10, 15, 22, and 30 stands for the mol% of aluminum added in the powder mixture in excess to the stoichiometric Al content. TF refers to the PECSed bulk sample that was additionally heat-treated in a tube furnace.

Figure 2.1 shows X-ray diffractograms of all samples reaction sintered in this study, including those that were annealed after reaction sintering (TF), while **Figure 2.2** and **Table 2-2** summarize the results of Rietveld analysis, including wt% of each phase that can be detected using XRD, and R_{wp}. Note here, that all XRD results in **Figure 2.1** are collected from the middle of the disk-shaped specimens for the reasons that are discussed in more detail later.

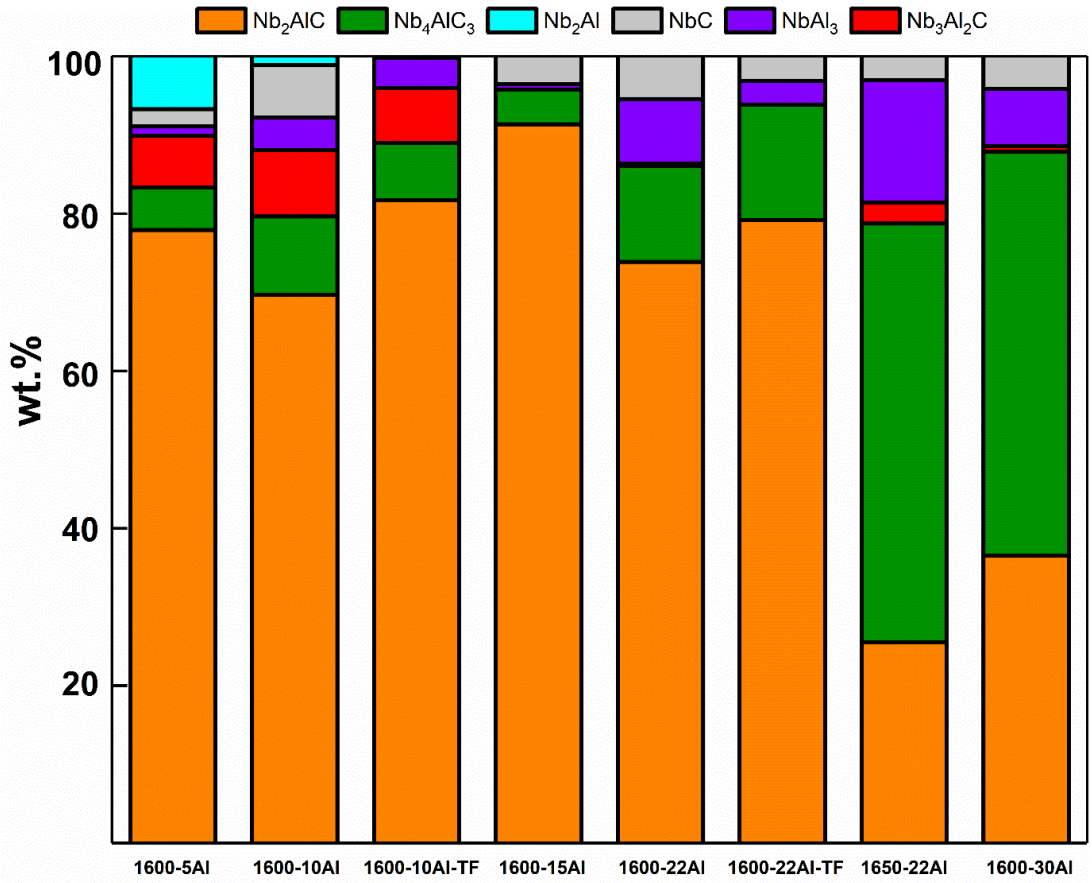

Figure 2-2 The stacked column showing the content of each phase detected within reaction-sintered samples.

Table 2-2 The content of each phase as determined by Rietveld refinement. Targeted Nb_2AlC is presented in bold character.

Sample	Phase content in wt.% from Rietveld analysis	R_{wp}	Calculated Nb:Al=2:X from the areal EDS of the sample
1600-5Al	**77.90% Nb_2AlC**, 5.44% Nb_4AlC_3, 6.54% Nb_3Al_2C, 1.18% $NbAl_3$, 2.21% NbC, 6.73% Nb_2Al	7.90	2:1.055
1600-10Al	**69.69% Nb_2AlC**, 9.94% Nb_4AlC_3, 8.44% Nb_3Al_2C, 4.12% $NbAl_3$, 6.65% NbC, 1.16% Nb_2Al	2.45	2:1.182
1600-10Al-TF	**81.71% Nb_2AlC**, 7.22% Nb_4AlC_3, 7.04% Nb_3Al_2C, 3.82% $NbAl_3$, 0.21% NbC	9.78	2:1.113
1600-15Al	**91.34% Nb_2AlC**, 4.43% Nb_4AlC_3, 0.67% $NbAl_3$, 3.56% NbC	5.90	2:1.017
1600-22Al	**73.88% Nb_2AlC**, 12.20% Nb_4AlC_3, 0.23% Nb_3Al_2C, 8.26% $NbAl_3$, 5.93% NbC	8.85	2:1.272

Table 2-2 Continued

Sample	Phase content in wt.% from Rietveld analysis	Rwp	Calculated Nb:Al=2:X from the areal EDS of the sample
1600-22Al-TF	**79.16% Nb_2AlC**, 14.66% Nb_4AlC_3, 0.03% Nb_3Al_2C, 3.00% $NbAl_3$, 3.16% NbC	6.96	2:1.055
1650-22Al	**25.51% Nb_2AlC**, 53.23% Nb_4AlC_3, 2.63% Nb_3Al_2C, 15.60% $NbAl_3$, 3.03% NbC	7.92	2:1.280
1600-30Al	**36.49% Nb_2AlC**, 51.41% Nb_4AlC_3, 0.67% Nb_3Al_2C, 7.31% $NbAl_3$, 4.12% NbC	6.25	2:1.016

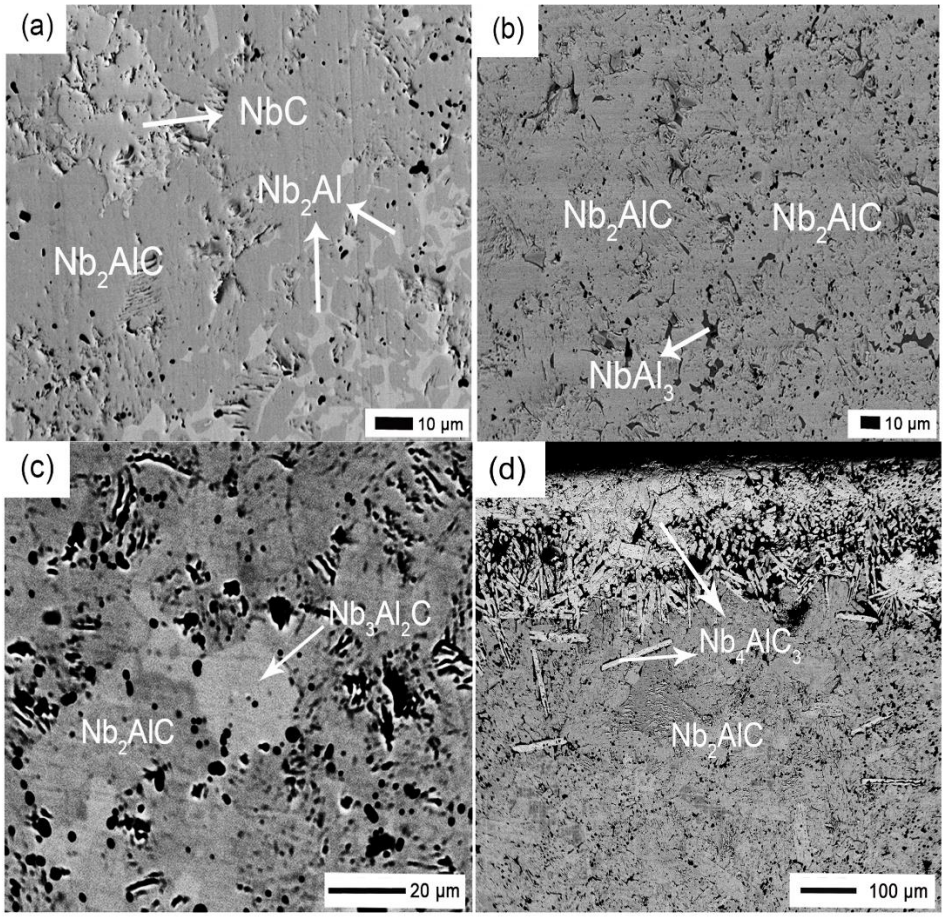

Figure 2-3 The selected but representative BSE images of (a) *1600-5Al*, (b) *1600-10Al*, (c) *1600-10Al-TF-middle* and (d) *1600-10Al-TF-edge*.

Table 2-3 Chemical compositions as determined using WDS by averaging in at least five different points in each phase of *1600-10Al-TF*.

Compounds	Nb at.%	Al at.%	C at.%	Nb/Al
Nb_2AlC	52.29±0.52	26.08±0.22	21.63±0.75	2.005
Nb_3Al_2C	52.44±1.30	34.29±1.36	13.27±2.58	1.529

To compensate for the loss of Al during sintering, we started by adding 5 mol% and 10 mol% excess Al (*1600-5Al, 1600-10Al*) into the starting powder mixture. Those amounts of excess Al were commonly used in the starting mixture of elemental powders to compensate for Al loss during reaction sintering of some other Al-based MAX phases[61,91,92]. As can be seen from XRD results in **Figure 2.1** and summary of Rietveld analysis in **Figure 2.2** and **Table 2-2**, besides the targeted Nb_2AlC, both *1600-5Al* and *1600-10Al* contained other phases, such as Nb_4AlC_3, Nb_3Al_2C, NbC as well as niobium-aluminides, which is also in good agreement with the corresponding backscattered micrograph (BSE) images, **Figure 2.3a** and **2.3b**, respectively, and EDS results (not shown here). Clusters of NbC were identified as well as sporadic niobium-aluminides distributed in the ternary carbide matrix in both samples. Since the average atomic number per atom of Nb_2AlC is 25.25 and very close to that of 25.8 for Nb_3Al_2C the difference between those two phases is not readily observed in BSE images, but the presence of the later was confirmed by the latter WDS analysis (**Figure 2.3c**). It is worth noting that the Nb_4AlC_3 detected by XRD is primarily located close to the surface of the disk-shaped samples (**Figure 2.3d**). The reason for the formation of these secondary phases can be result of (i) incomplete sintering reaction process, i.e., thermodynamic equilibrium has not been reached, or (ii) deviation from the Nb:Al:C molar ratio of 2:1:1

in the sample after reaction sintering, primarily because of volatilization of the low melting point Al.

To check if the high amount of secondary phases in samples *1600-5Al* and *1600-10Al* are due to incomplete reactions, the later one was additionally heated in the tube furnace at 1600 ^{o}C for 4 hours (**Table 2-1**). Note here that despite the fact that the PECSed reaction synthesis benefit from the short sintering duration due to the rapid heating and cooling rates, the incomplete reaction between reactants could be quite common because of local inhomogeneity of composition in the starting powders as well as temperature gradients in the sample [82,83]. As shown in **Figures 2.1** and **2.2,** and **Table 2-2**, additional thermal treatment resulted in the increased amount of Nb_2AlC from 69.69% to 81.71% and decrease in the amount of all secondary phases (Nb_2Al, $NbAl_3Nb_3Al_2C$, and NbC) as well as formation of smaller amount of $NbAl_3$. Note here that two major secondary phases, namely N_4AlC_3 and Nb_3Al_2C have Nb:Al ratio of 4:1 and 1.5:1, respectively, and thus quite different from 2:1 in the targeted Nb_2AlC, while the third major secondary phase NbC does not contain any aluminum. Formation of those two phases was never reported in previous attempt to reaction sinter Nb_2AlC using PECS from the mixture of Nb, NbC and Al powders. The presence of both those phases even after additional heat treatment in the tube furnace for 4 hours has been additionally confirmed using WDS, **Figure 2.3d**. However, regardless of the presence of larger amount of Al deficient secondary phases in samples having 5% and 10% of access Al in the initial powder mixtures, the areal EDS analysis shows (**Table 2-2**) that samples after reaction sintering still contain substantial amount of excess Al. Even more, those results also show

decrease in the overall Al content in the samples after additional thermal treatment in a tube furnace, regardless of the additional reaction of secondary phases to form more Nb_2AlC, suggesting that continuous volatilization of Al during sintering most likely from lower melting point phases, such as intermetallic phases. Results presented thus far suggest that redundant Al within the PECSed samples can be attributed to the appearance of Nb_3Al_2C and niobium aluminides that forms locally where Al content in the powder is higher, while the presence of high amount of Nb_4AlC_3 and NbC is possibly stemming from the lack of Al locally in the powder mixtures and short sintering times. Because of the very short reaction times during PECS, it is default to achieve a uniform concentration of Al throughout the sample and thus reaction sintered sample contains a larger amount of secondary phases, both having Nb:Al>2 and <2.

In the attempt to obtain higher phase purity of Nb_2Al_xC phase, a sample *1600-15Al* was reaction sintered using with 15mol.% access aluminum using same sintering conditions as in the case of 1600-5Al and 1600-10Al. More aluminum was added to avoid formation of Al-deficient phase such as NbC and Nb_3Al_2C. In addition, it has been reported that adding more Al would promote transformation of Nb_4AlC_3 to its 211-derivative [48]. As indicated in **Figure 2.2** and **Table 2-2**, over 90 wt.% Nb_2AlC (91.34 wt.%) formed *1600-15Al* after direct PECS, along with small amount of secondary phases. The corresponding BSE SEM image (see **Figure 2.4**) present the predominant targeted Nb_2AlC phase throughout the bulk sample, while $NbAl_3$ secondary phases is distributed sporadically in Nb_2AlC matrix as shown in the inset. The calculated Nb:Al atomic ratio from areal was 2:1.017 (**Table 2-2**) suggesting that there was almost no more excess Al

remains in the as-sintered sample. In other words, the fact of the stoichiometry of the as-prepared sample is approximately equal to the nominal stoichiometry of Nb_2AlC demonstrates the sintering reaction was completed. More importantly, all those results indicate that adding 15 mol% excess Al in the starting powder mixture is the almost optimum for obtaining high-purity Nb_2AlC from elemental powders using PECS.

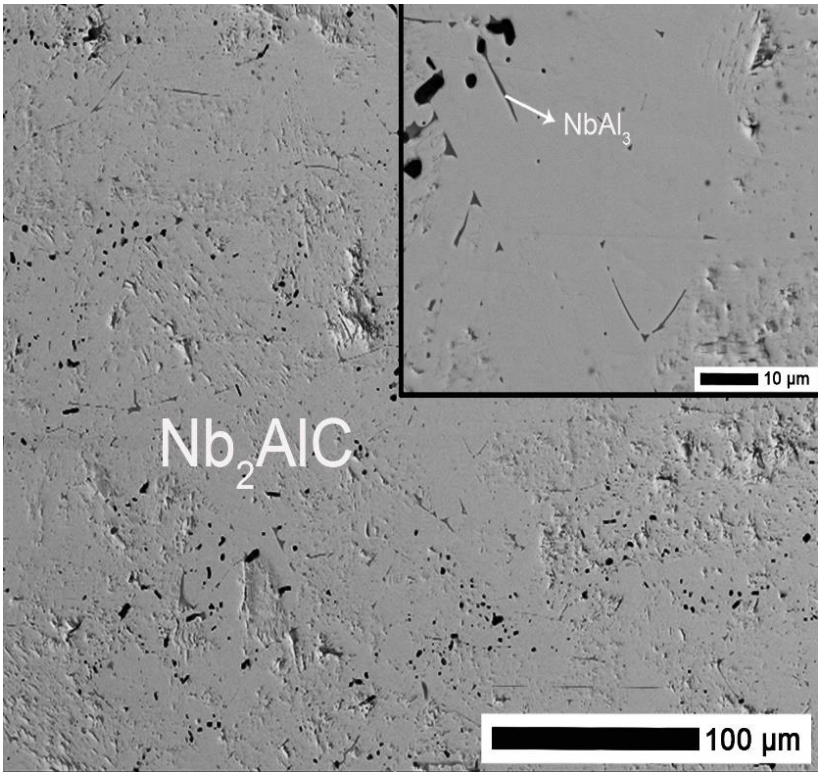

Figure 2-4 BSE micrograph collected from *1600-15Al*. The top inset is the area taken under a larger magnification, indicating trace amounts of impurities distributed in the Nb_2AlC matrix.

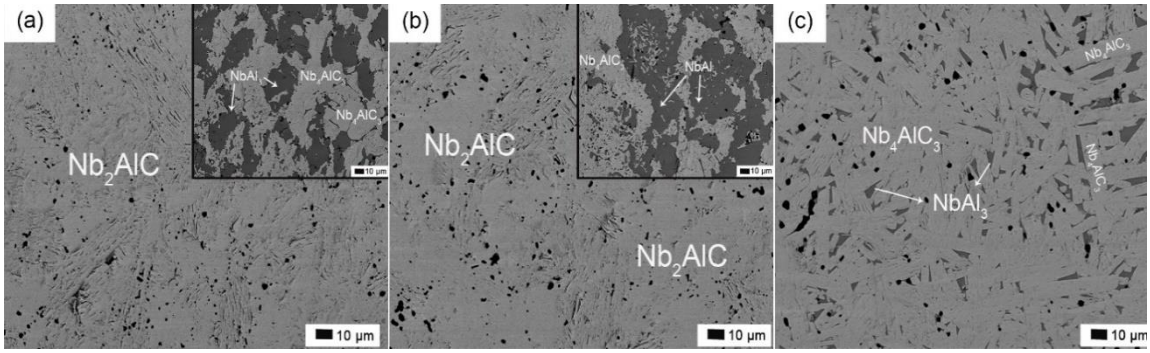

Figure 2-5 BSE micrographs collected from (a) *1600-22Al,* (b) *1600-22Al-TF,* and (c) *1650-22Al.* The insets of (a) and (b) are corresponding impurity-rich areas.

In the work of Yeh et al. [93], the formation of the targeted MAX phase was improved because of an excessive amount of Al, which was reported by Hu et al. as well [94]. Therefore, we increased the next step excess Al in the starting powder mixture from 15 mol% to 22 mol% (*1600-22Al*) and even 30 mol% (*1600-30Al*), in the attempt to active higher phase purity of Nb_2AlC. However, as it can be seen from **Figures 2.1 and 2.2, and in Table 2-2**, the amount of Nb_2AlC phase in *1600-22Al* and *1600-30Al* was lower than in sample *1600-15Al*. In addition, noticeable amounts of Nb_4AlC_3, $NbAl_3$, and NbC secondary phases were identified within both and *1600-22Al* and *1600-30Al* and their amount actually increased with increasing amount of excess Al. BSE SEM images and EDS results of sample *1600-22Al* in **Figure 2.5a** further confirms those findings. In addition, calculated Nb:Al atomic ratio from areal EDS was in **Table 2-2**, confirms significant amount of remaining excess Al in both samples. To check if further reaction between secondary phases can results in the higher phase purity, *1600-22Al* was selected for further annealing at 1600^{o}C for 4 hours (*1600-22Al-TF*). As shown in **Figures 2.1 and 2.2** and **Table 2-2**, this resulted only in minor increase in the amount of Nb_2AlC and Nb_4AlC_3 in the sample, followed by the significant decrease on the amount of excess Al,

i.e., Nb:Al ratio from areal EDS dropped from 2:1.272 to 2:1.055 after annealing. Due to the limited aid of annealing, *1600-22Al-TF* did not significantly improved yield of Nb_2AlC, as it can be also seen by comparing BSE SEM images in **Figures 2.5a** and **2.5b**.

As mentioned earlier, another way to promote a fully complete reaction is by increasing sintering temperature. Therefore, the powder compact with the same 22 mol% excess Al was sintered at 1650^{o}C (*1650-22Al*) using PECS. As can be seen in **Figures 2.1 and 2.2,** and **Table 2-2**, compared with *1600-22Al*, *1650-22Al* had more amount of secondary phases, while the content of Nb_2AlC phase decreased from 73.88 to 25.51 wt.%, whereas Nb_4AlC_3 increased from 12.20 to 53.23 wt.% by increasing sintering temperature. In addition, increase in the amount of Nb_3Al_2C is noticeable by increasing sintering temperature, suggesting that formed Nb_2AlC most likely starts to decompose at 1650^{o}C according to the following reaction

$$5Nb_2AlC = Nb_4AlC_3 + 2Nb_3Al_2C \quad (3)$$

This transformation from 211 to 413 MAX phases was frequently reported in other Al-based MAX phases [93,95]. The increment of the amount of $NbAl_3$ stemmed from the outward diffusion of molten Al during sintering, resulting in further Al-deficiency areas in the middle of the sample and the formation of Nb_4AlC_3 . As shown in BSE SEM images in **Figure 2.5c**, when the sintering temperature was increased to 1650^{o}C, the sample with 22% excess Al had substantial amount of Nb_4AlC_3 besides niobium-aluminide secondary phase.

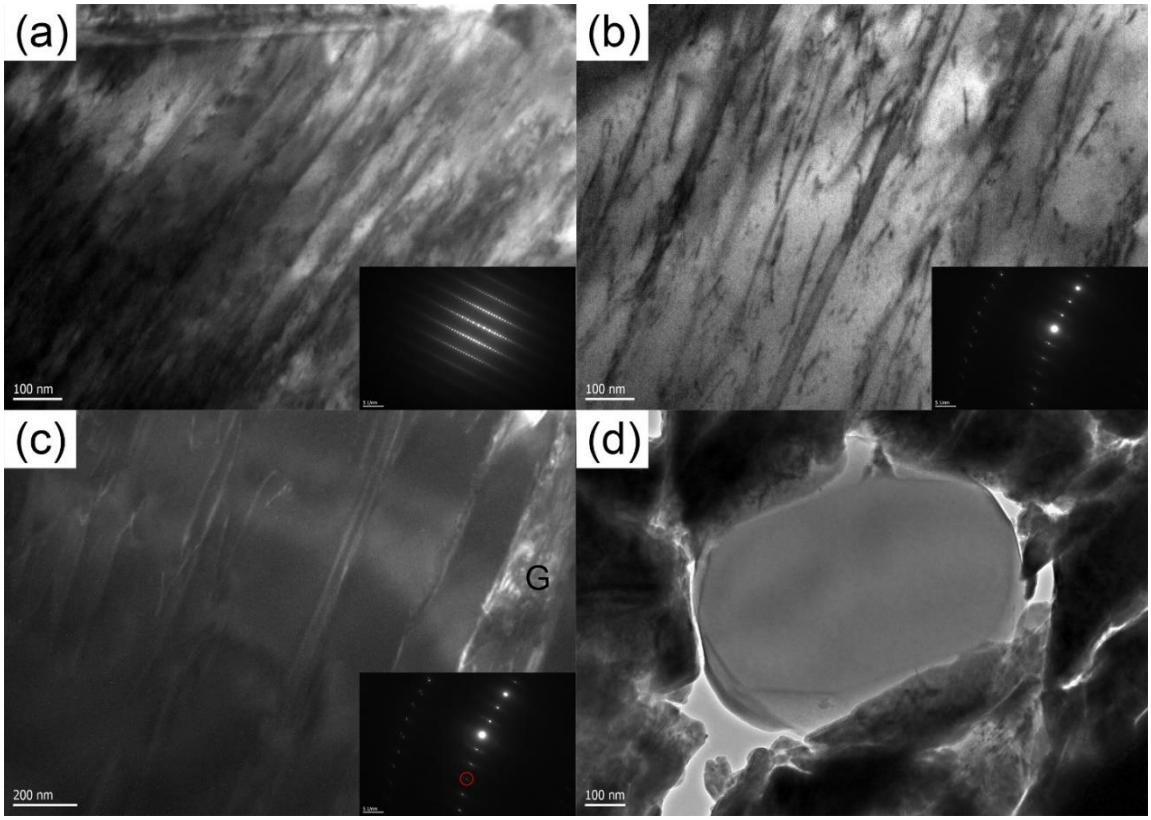

Figure 2-6 Representative TEM micrographs of the *1600-10Al-TF* sample. (a) brightfield on zone down the [11$\bar{2}$0] axis, (b) sample tilted off zone to a brightfield 2-beam condition, (c) weak-beam dark field (WBDF) image revealing dislocation arrays. "G" stands for the grain boundary and the red circle indicates which diffraction spot was used for the weak beam imaging. Dislocations appear to be straight lines when viewed on the zone in (a), but in fact are curved within the basal planes, and some appear to emanate from a grain boundary, as seen when tilted in (c). (d) An Al_2O_3 particle.

For the sake of investigating the atomic structures of Nb_2AlC and potential impurities, after the WDS measurement, *1600-10Al-TF* was selected for being operated conventional TEM and HR-STEM analysis. Conventional TEM micrographs of *1600-10Al-TF* lamella revealed presence of dislocations in the Nb_2AlC phase after PECS, **Figure 2.6**. Most of the grains appear clear of damage, lacking significant dislocation density. Occasionally, as seen in **Figure 2.6**, some grains contain perfect basal dislocations throughout, as well as growth dislocation arrays. The sample lamella was fully crystalline and contained a small Al_2O_3 impurity particle (**Figure 2.6(d)**). **Figure 7** shows the HR-

STEM micrographs of *1600-10Al-TF* sample in annular dark-field (ADF) and high-angle annular dark-field (HAADF) mode acquired along the [11 $\bar{2}$ 0] zone axis. The corresponding Nb (red), Al (blue), and C (green) atoms were overlaid to distinguish the atomic structure readily. Typical 211 MAX phase structure, with alternating two Nb-layers interleaved by an Al-layer can be apparently observed. The measured *a* and *c* lattice parameters are 3.113±0.001 Å and 13.894±0.001 Å, respectively, which are very close to our Rietveld refined values (*a* = 3.1097±0.0001 Å; c = 13.8876±0.0005 Å) and the reported ones [71].

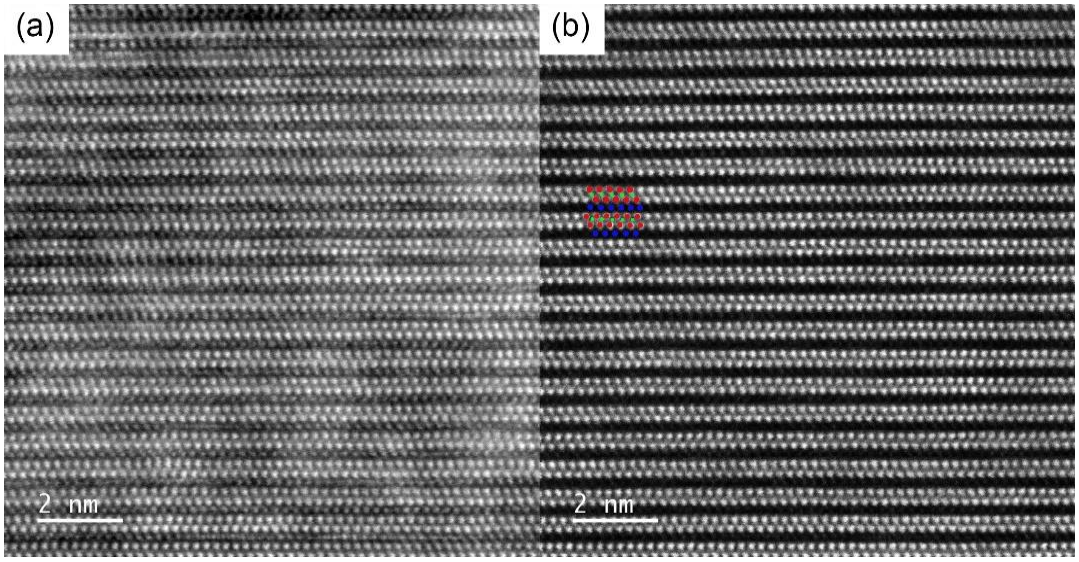

Figure 2-7 HR-S/TEM image of Nb_2AlC in (a) ADF and (b) HAADF mode. Respective Nb (red), Al (blue), and C (green) atoms were highlighted in (b) for the ease of demonstration.

Table 2-4 Summary of measured properties of *1600-15Al* and the comparison with other reported values.

Properties	**This work**	**Reference** [74,96]
Poisson's Ratio	0.24	0.24
Bulk (GPa)	184	183
Shear (GPa)	116	116
Youngs (GPa)	287	288
Density (g/cm^3)	6.37	6.47
Vickers Hardness (GPa)	4.2	4.0

Table 2-4 summarizes the measured mechanical properties of *1600-15Al* in the present work and compares them to the previously published results. The value of the Poisson's ratio and the determined bulk, shear, and Young's moduli are in good agreement with the reported ones. The density of 1600-15Al was measured to be 6.37 g/cm^3, which is 98% of the value (6.47 g/cm^3) previously reported for Nb_2AlC [74], probably owing to the remaining pores after the reaction sintering process.

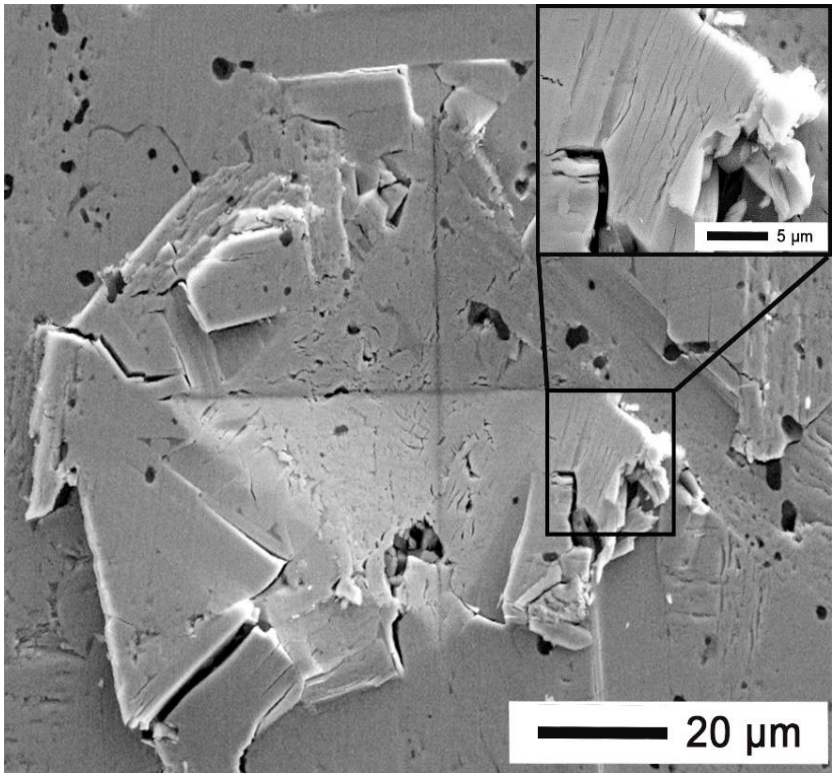

Figure 2-8 The SEM image of the indented area of *1600-15Al*. The inset displays the representative delamination feature of MAX phases.

Figure 2.8 shows the SEM image of the indented area after Vickers hardness testing of *1600-15Al* testing. The measured value of hardness of 4.20±0.22 GPa is slightly higher than that reported for Nb_2AlC sintered using PECS technique [74]. Similar as in

other MAX phases, the delamination and kinking of individual lamellas can be observed after indentation [97,98].

2.4. Summary

In summary, the elemental powder mixture of Nb:Al:C=2:1.15:0.95 sintered at 1600^{o}C for 30 min with a heating rate of 25^{o}C/min was found to be result in formation of highly-pure Nb_2AlC (>91 wt.%) using the PECS technique. Decreasing the excess amount of Al in the starting materials results in the formation of another MAX phase Nb_4AlC_3 while increasing the amount of excessive Al beyond the value used in the optimized recipe triggers the formation of profuse niobium-aluminides. Due to the applied pressure during the sintering, these niobium-aluminides were pushed toward edges of the sample and left a few Al-deficient areas, which in turn results in the formation of Nb_4AlC_3 once again. Moreover, increasing the sintering temperature to 1650^{o}C induced Nb_2AlC to decompose into Nb_4AlC_3 and another not commonly reported niobium-carbide, namely Nb_3Al_2C. The actual atomic percentages of Nb, Al, and C in Nb_2AlC is 52.29±0.52, 26.08±0.22, and 21.63±0.75, respectively, determined by WDS. HR-STEM confirmed the atomic structure of Nb_2AlC with two M-layers interleaved by an A-layer. The obtained Vickers hardness of as-prepared Nb_2AlC is 4.2 GPa and the bulk, shear, and Young's modulus are 184, 116, and 287 GPa, respectively. The method of synthesizing highly pure Nb_2AlC using the PECS technique can not only shed light on synthesizing other MAX phases using the same technique but also promote the yield of related 2D materials (MXene) from the parent-materials-purity standpoint.

3. SYNTHESIS, MICROSTRUCTURE CHARACTERIZATIONS, AND MECHANICAL PROPERTIES OF $(Ti_xNb_{1-x})_2AlC$ SOLID SOLUTION WITH x = 0-1

3.1. Literature Review

MAX phases are a family of ternary carbides and/or nitrides with a general chemical formula of $M_{n+1}AX_n$, where n = 1-3 [8,58,99]. M stands for an early transition metal, A refers to an element from group 13-16, and X is either carbon or nitrogen. MAX phases crystallize in a *$P6_3/mmc$* layered structure where layers of edge-sharing M_6X octahedra are interleaved with a layer of A element [6]. Thanks to their layered structure, MAX phases possess combination of metal- and ceramic-like properties such as easy machinability, excellent damage tolerance, good thermal and electrical conductivity, but at the same time high stiffness, high temperature stability and some of them display exceptional corrosion and oxidation resistance at high temperatures [2,14,15,17,59,66,100,101].

As one of the most studied member of MAX phases, Ti_2AlC is known for its remarkable oxidation resistance aided by self-forming alumina protective oxide scale due to the outward diffusion of Al toward interface [1,102–104]. On the other hand, Nb_2AlC is considered as one of the possibly most refractory MAX phases with good mechanical properties, which renders it a good candidate for high temperature structural applications [72,73,105]. Combined with the fact that MAX phases possess considerable possibilities of tuning their properties by alloying on the M, A, and X sites, alloying Ti_2AlC with Nb on the M-site could improve its mechanical properties while preserving extraordinary

oxidation resistance. However, only a few works have been reported the synthesis and properties $(Ti_xNb_{1-x})_2AlC$. Nowotony *et al.* first synthesized $(Ti_xNb_{1-x})_2AlC$ with x = 0.25, 0.5, 0.75 using arc melting method starting from NbC and Al_4C_3 and showed that both lattice parameters *a* and *c* increase with the increasing content of Nb within the samples [70]. Salama *et al.* successfully fabricated predominant single-phase $(Ti_{0.46}Nb_{0.54})_2AlC$ by reactive hot isostatic pressing (HIPing) using Nb, graphite, and Al_4C_3. They also showed that 1000-1200 ^oC, the formation of TiO_2 by the inward diffusion of oxygen led to a better oxidation resistance of thsi solid solution compared to that of Nb_2AlC. In addition, solid solution's electrical resistivity increased linearly with increasing temperature, and the thermal expansion coefficient was determined as 8.9 x $10^{-6}K^{-1}$ [71,77,106], which is close to the value reported by Barsoum *et al.* from hot-pressed $(Ti_{0.45}Nb_{0.55})_2AlC$ starting from the mixture of Nb, Al_4C_3, and graphite [107]. Alexander *et al.* mixed 4 atomic percent (at. %) Nb with commercial MAXTHAL 211 ® and heated it at 900 ^oC for 120 h. They found that the addition of Nb resulted in a more homogenous oxide layer on the specimen than the Nb-free sample [21].

Building on the above brief literature review on the synthesis and properties of $(Ti_xNb_{1-x})_2AlC$, the most studied composition in Nb-Ti-Al-C system is $(Ti_{0.5}Nb_{0.5})_2AlC$. To the best of our knowledge, there is no study on the synthesis and mechanical properties of $(Ti_xNb_{1-x})_2AlC$ with a full-range of solute concentration on the M-site. Given the fact that Nb and Ti are fully miscible on the M-site of M_2AlC, we prepared a series of highly phase-pure MAX phase solutions by PECS and investigated the changing trend of mechanical properties over the full range of compositions.

3.2. Experimental Methods

Commercial elemental powders of Nb (Alfa Aesar, 325 mesh, 99.8%), Ti (Alfa Aesar, 325 mesh, 99.5%), and graphite (Alfa Aesar, 7-10 micron, 99%) were selected as starting materials for synthesis. Powders were mixed with the molar ratio of $2(Ti_xNb_{1-x})$:1.1Al:0.95C, where y = 0.1, 0.25, 0.5, 0.75, 0.8, 0.9, 0.95, and 1. An excessive aluminum usage is aimed to compensate for the loss of material during the sintering and the deficiency in C is often applied to Al-containing MAX phases. Samples are named by their respective titanium percentage pertaining to the M-site, i.e., 25 Ti means x is equal to 0.25. Nb_2AlC (x = 0) was prepared separately using the details described elsewhere. Powder mixtures were ball-milled with ZrO_2 beads for 24 hours at 300 rpm and placed into a 20 mm graphite die. Green bodies were sintered by pulse electric current sintering (PECS, Thermal Technologies, LLC, CA). Each composition has its unique sintering condition that were optimized up on a series of investigations of effect that reaction routes has on the phase purity of the samples, as it is explained in subsequent paragraphs.

X-ray diffractograms (D8-Focus, Bruker, Madison, USA) were collected from the cross-section areas of as-prepared samples which were polished down to 1 μm diamond paste with a step size of 0.019^o and time per step of 0.4 s at 40 kV and 25 mA. Rietveld refinement was operated by TOPAS V4.2 (Bruker, Madison, USA) to acquire the lattice parameters of all compositions and weight percent (wt. %) of each phase detected in the final specimen. Microstructure and elemental composition analysis were performed using TESCAN LYRA-3 Model GMH Ga^+ Focused Ion Beam – Scanning Electron Microscope

(FIB-SEM) equipped with Energy Dispersive Spectrometer (EDS, Oxford, United Kingdom).

Young's and shear moduli were measured by Resonant Ultrasound Spectroscopy (RUS, Quasar RUSpec, Magnaflux, IL) at room temperature using the procedure described elsewhere [61,86]. A small disc with the diameter and thickness of 20.00 mm and 3.30 mm, respectively, was placed on three piezoelectric transducers. The elastic wave with constant amplitude and changing frequency generated by one of the transducers was transferred to the sample and the resulted mechanical vibrations were measured by the other two. Resulting resonant spectra, we further deconvoluted using RUSpec software (Vibrant, NM) to obtain Young's and shear moduli for samples of known mass and dimensions.

Vickers hardness test was performed using microhardness tester LM 300AT (LECO, MI) under a load of 500 gram-force (gf) using a diamond Vickers indenter. The hardness calculated as $H = 1.8544*P/d_v^2$, where P (gf) is the applied load, and d_v (μm) is the average of the two diagonals of an indent [90]. The sample's density was measured by Archimedes' method, using method described in more details elsewhere [16,19].

To conduct the compressive test, reaction-sintered samples were machined by electro-discharge machining (Wire-EDM) with a dimension of 5.5 x 5.5 x 11 mm and then quasi-statically compressed to failure at room temperature using a servo – hydraulic testing machines (MTS-810, MTS, USA) with SiC pushrods under a constant crosshead displacement rate to a strain rate of $10^{-4}s^{-1}$. The fracture surfaces after testing were characterized by SEM.

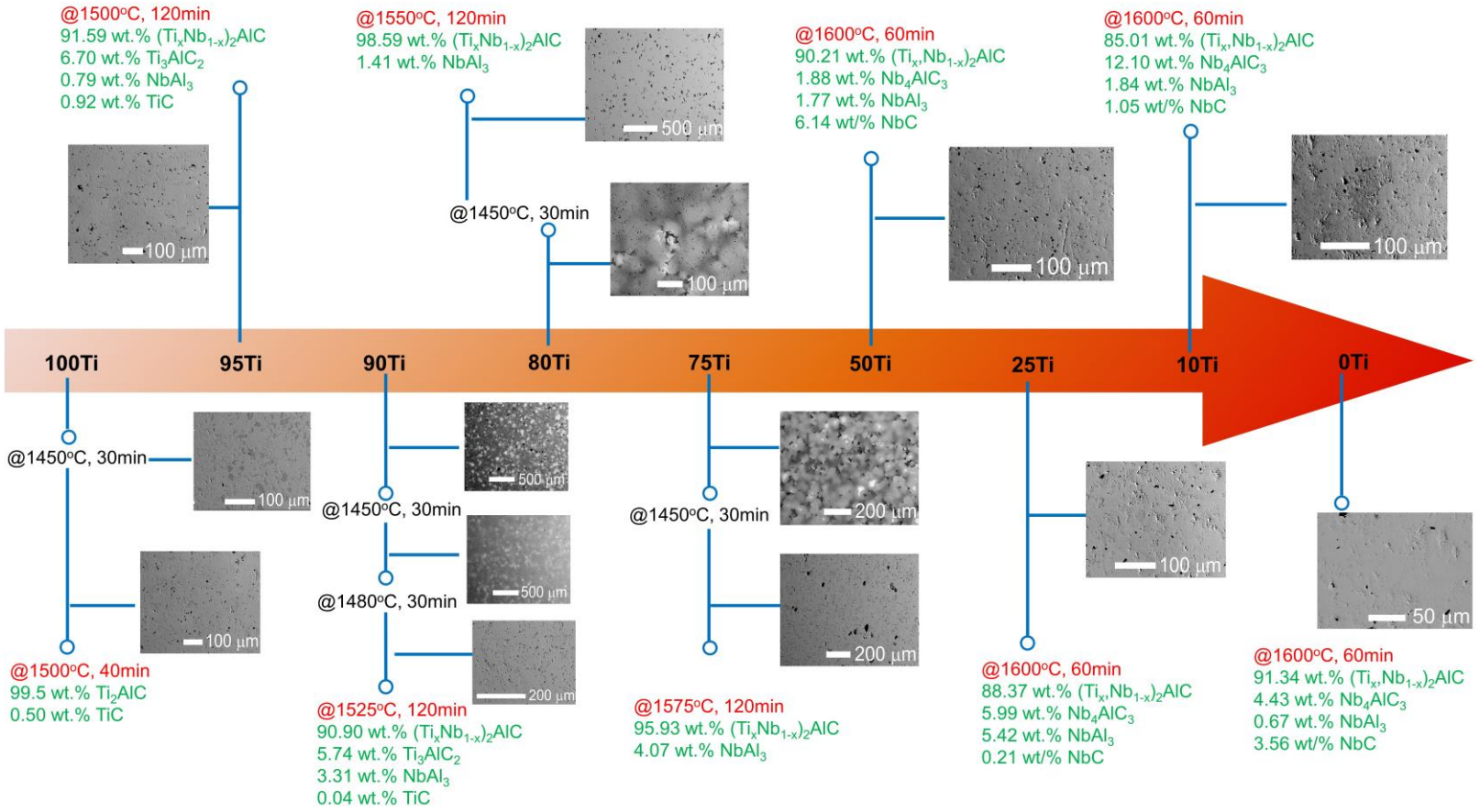

Figure 3-1 Reaction routes of synthesizing highly phase-pure $(Ti_xNb_{1-x})_2AlC$ with x = 0-1.

3.3. Results and Discussion

The reaction routes of synthesizing highly phase-pure $(Ti_xNb_{1-x})_2AlC$ with x = 0-1 is summarized in **Figure 3.1**. The optimized sintering conditions for each composition is highlighted in red and while wt.% of each phase determined using Rietveld refinement of XRD results for each sample is highlighted in green. Target solid solution's content has been improved by increasing the sintering temperature and elongating the dwell time accordingly. Pure Nb_2AlC (0Ti) was sintered under 1600 ^oC for 60 min using PECS based on the results from Chapter 2. From 0Ti to 50Ti, the samples with high phase purity, i.e. with approximately more than 90% of $(Ti_xNb_{1-x})_2AlC$ were obtained from the same sintering condition. Pure Ti_2AlC (100Ti) was made under 1500 ^oC for 40 min following sintering procedures reported elsewhere (x). The required temperature was higher than the one prepared by the same sintering technique [108], which is due to the different starting materials used. However, for solid solutions samples with more than 50% Ti, the sintering temperature hat to be increased stepwise with a degree of 25 ^oC, i.e., 1500 ^oC for 95Ti, 1525 ^oC for 90Ti, 1550 ^oC for 80Ti, and 1575 ^oC for 75Ti in order to synthesize high purity samples.

The X-ray diffractograms collected from cross-section areas of all reaction-sintered samples are shown in **Figure 3.2**. Besides the target $(Ti_xNb_{1-x})_2AlC$, side phases such as $NbAl_3$, niobium aluminum carbides and titanium aluminum carbides in different amounts were detected and labeled. (013) and (006) peaks at 2θ angle of approximately 38.5^o and 40.0^o belonging to $(Ti_xNb_{1-x})_2AlC$ are represented in **Figure 3.3**. Both peaks move toward a higher 2θ angle with increasing amount of Ti within a sample which results

from the size difference between Nb and Ti atoms. The atomic radius of Ti is smaller than the one of Nb [109], therefore, the atomic spacing is expected to decrease when Ti atoms are replaced Nb atoms on the M-site of the target solid solution, leading to the characteristic peaks moved to the higher 2θ angle in **Figure 3.3**.

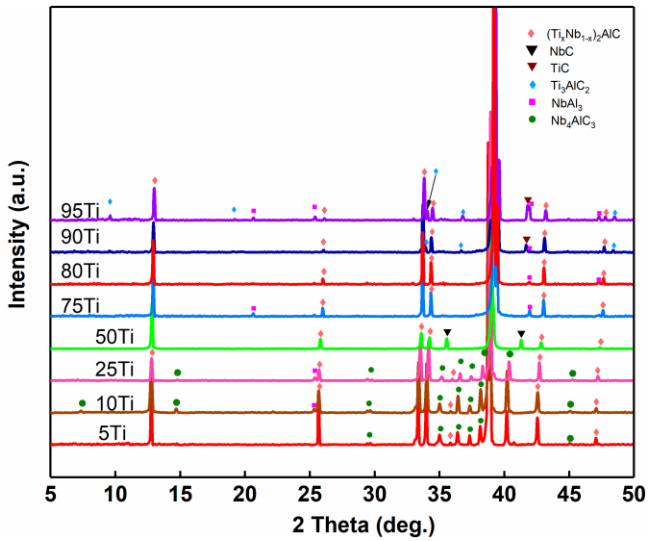

Figure 3-2 X-ray diffractograms of $(Ti_xNb_{1-x})_2AlC$, where x is equal to 0.05, 0.10, 0.25, 0.50, 0.75, 0.80, 0.90 and 0.95. Peaks in between 38.5° to 40.0° were truncated to fit the graph.

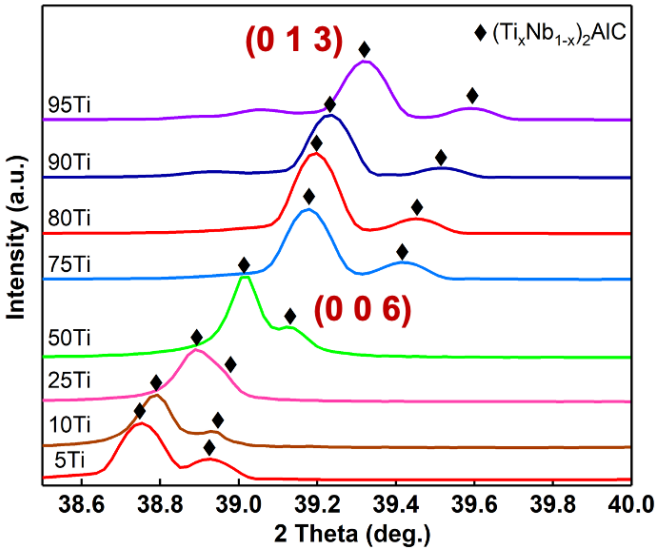

Figure 3-3 Magnified XRD results from Figure 2 in the area of (013) and (006) peaks belonging to $(Ti_xNb_{1-x})_2AlC$. Both peaks shift toward a higher 2θ angle with the increasing content of Ti in $(Ti_xNb_{1-x})_2AlC$.

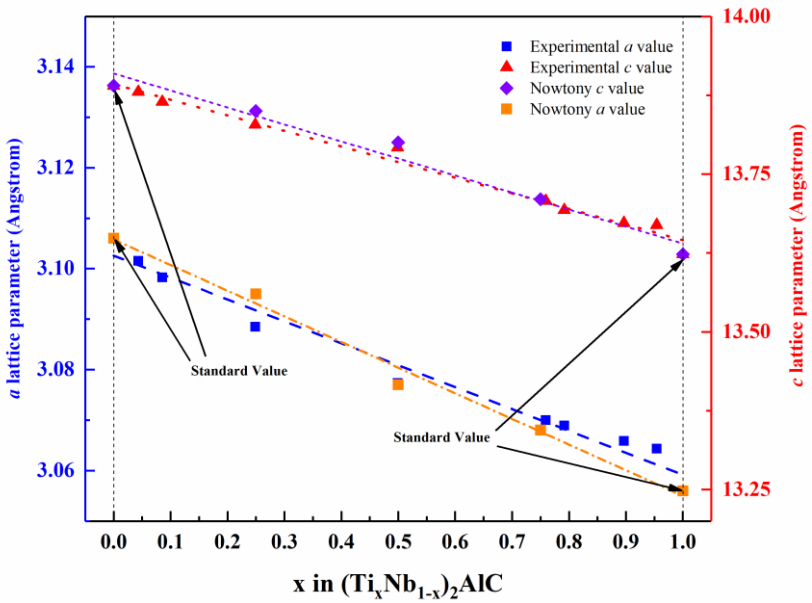

Figure 3-4 The changing trend of lattice parameters *a* and *c* as a function of Ti content. Values obtained from Nowotny's work [70] **and ICSD** [110] **are added for comparison.**

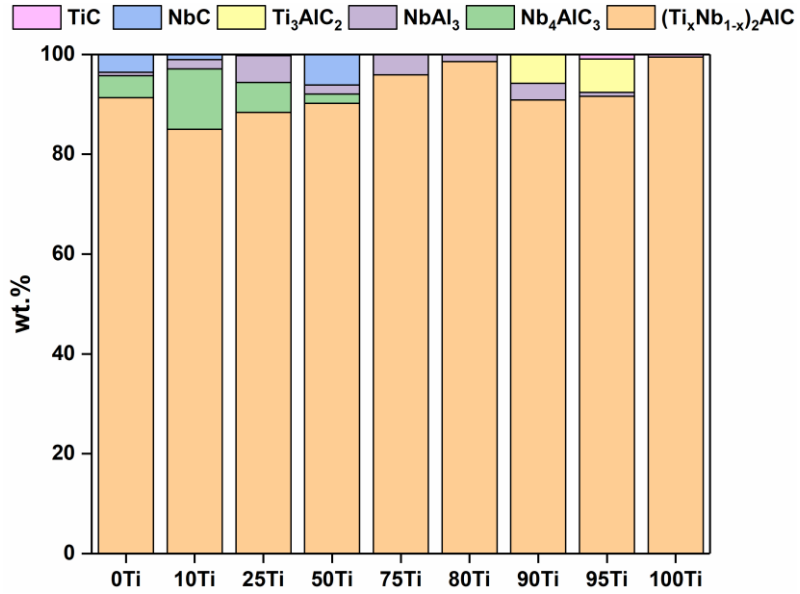

Figure 3-5 The wt. % of each phase acquired by Rietveld refinement. Target $(Ti_xNb_{1-x})_2AlC$ is the predominant phase for all compositions.

The changing trend of lattice parameters *a* and *c* over the full composition obtained by Rietveld refinement is displayed in **Figure 3.4**. Data points collected from Nowotny's

work and ICSD (the ones of Ti_2AlC and Nb_2AlC) were added for comparison [70,110]. One can easily see that both *a* and *c* decreased almost linearly with an increasing amount of Ti in $(Ti_xNb_{1-x})_2AlC$ following Vegard's law [111], which is in agreement with the tendency previously demonstrated by Nowotny *et al.* . The wt. % of each phase discerned by XRD was acquired by Rietveld refinement and visualized in **Figure 3.5**.

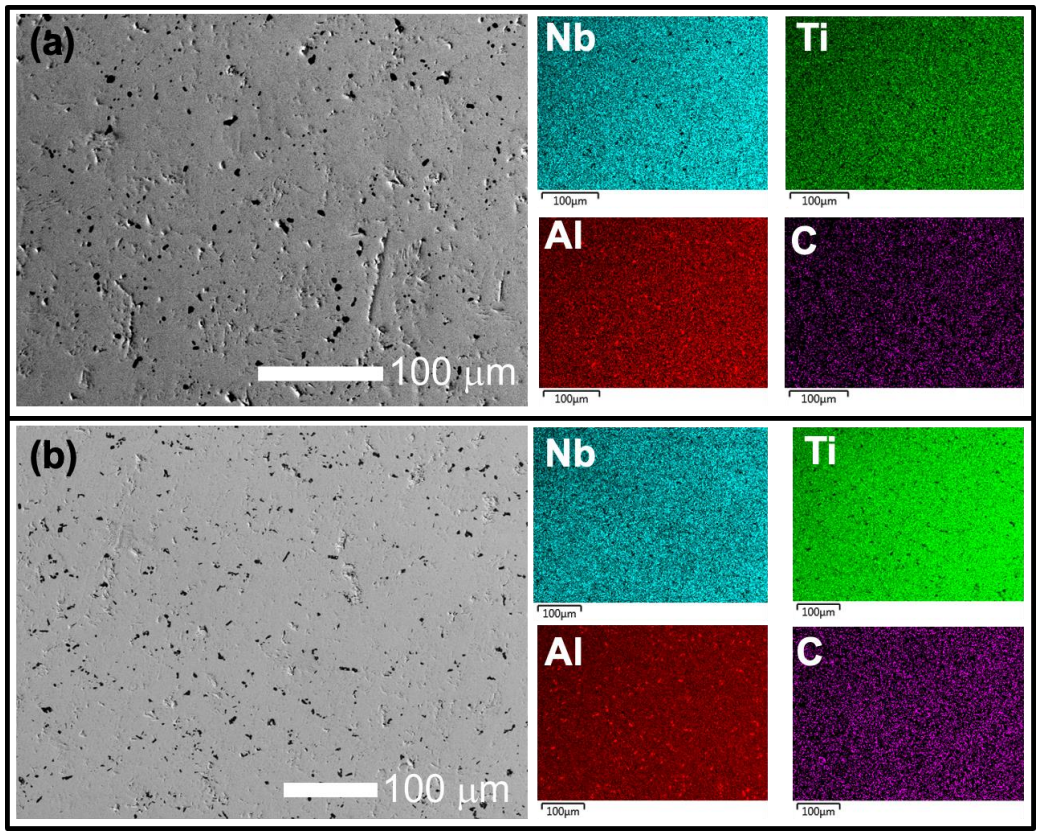

Figure 3-6 Selective but representative back-scattered electron SEM images with EDS maps of samples (a) 50Ti and (b) 80Ti.

Table 3-1 EDS point analysis of all reaction sintered samples. Results were obtained by averaging at least 4 points.

Samples	Nb at.%	Ti at.%	Al at.%	C at.%	(Nb+Ti)/Al	Ti/(Nb+Ti)
0Ti	31.34±0.45	N/A	14.05±0.40	54.61±0.61	2.23±0.07	0%

Table 3-1 Continued

Samples	Nb at.%	Ti at.%	Al at.%	C at.%	(Nb+Ti)/Al	Ti/(Nb+Ti)
10Ti	36.19±1.22	3.26±0.09	17.14±0.64	43.42±1.85	2.30±0.04	8.27%±0.26%
25Ti	33.58±0.23	10.36±0.22	19.27±0.26	36.79±0.69	2.28±0.01	23.58%±0.26%
50Ti	19.44±0.29	19.86±0.15	16.90±0.16	43.81±0.35	2.33±0.02	50.54%±0.52%
75Ti	11.15±0.57	32.18±0.70	18.27±0.19	38.41±0.52	2.37±0.01	74.27%±1.35%
80Ti	9.01±1.45	35.07±2.41	19.00±0.47	36.93±1.42	2.32±0.02	79.47%±3.72%
90Ti	4.50±0.59	43.89±3.21	21.42±1.59	30.20±4.14	2.26±0.07	90.62%±1.68%
95Ti	2.20±0.28	44.59±0.43	20.32±0.47	32.89±1.17	2.30±0.02	95.31%±0.52%
100Ti	N/A	51.88±0.31	23.00±0.31	25.13±0.23	2.26±0.04	100%

Selective but representative SEM images collected in back-scattered mode with corresponding EDS maps of 50Ti and 80Ti are represented in **Figure 3.6a** and 3.**6b**, respectively. Images collected from other compositions were similar to these two and henceforth are not presented herein. As can be seen, target solid solution $(Ti_xNb_{1-x})_2AlC$ was the predominant phase where both Nb and Ti distributed homogeneously within the matrix. The atomic ratios of (Nb+Ti)/Al and Ti/(Nb+Ti) in $(Ti_xNb_{1-x})_2AlC$ (**Table 3-1**) were close to the nominal values indicating the synthesized MAX phase solid solution belonged to the 211-class.

The compressive strength of $(Ti_xNb_{1-x})_2AlC$ over the full compositional range is shown in **Figure 3.7**. The compressive strength of Nb_2AlC of 1.6 GPa reported herein is the highest ever reported among all MAX phases, confirming good mechanical properties of Nb_2AlC. However, the compressive strength decreased almost linearly from 1.6 GPa for pure Nb_2AlC to 0.9 GPa for pure Ti_2AlC with increasing amount of Ti in $(Ti_xNb_{1-}$

$_x)_2$AlC. Unfortunately, no solid solution strengthening effect is observed, which is consistent with what Salama et al. claimed in their work [77]. All samples failed in compressive testing by forming the crack 45oC relative to applied load which is typical for most of the MAX phases. Selected but typical SEM image of the fracture surface in sample 75Ti shows kink bands that are typically observed in all MAX phases [78,112]. The Vickers hardness of $(Ti_xNb_{1-x})_2AlC$ over the full composition also displayed a decreasing trend with the rising content of Ti in the solid solution and the representative delamination feature was found (see **Figure 3.8**). The changing trend of Young's and shear moduli of $(Ti_xNb_{1-x})_2AlC$ over the full composition is represented in **Figure 3.9**. Approximately linearly decreasing tendency was observed for both moduli.

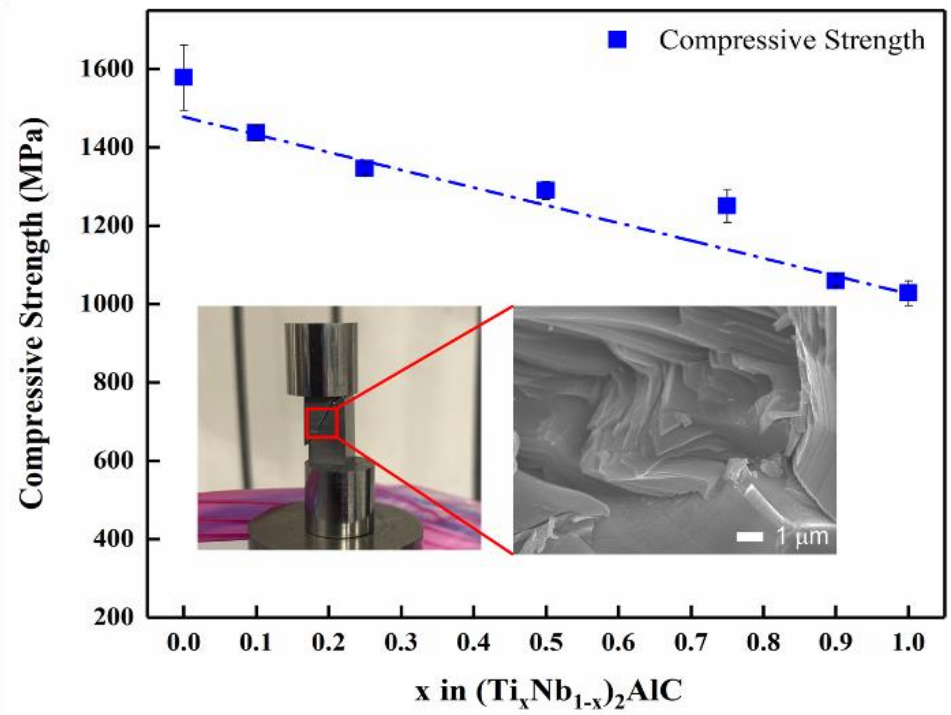

Figure 3-7 The compressive strength of $(Ti_xNb_{1-x})_2AlC$ over the full range of composition. The insets show photograph of the sample 75Ti after failure and SEM image of the fracture surface.

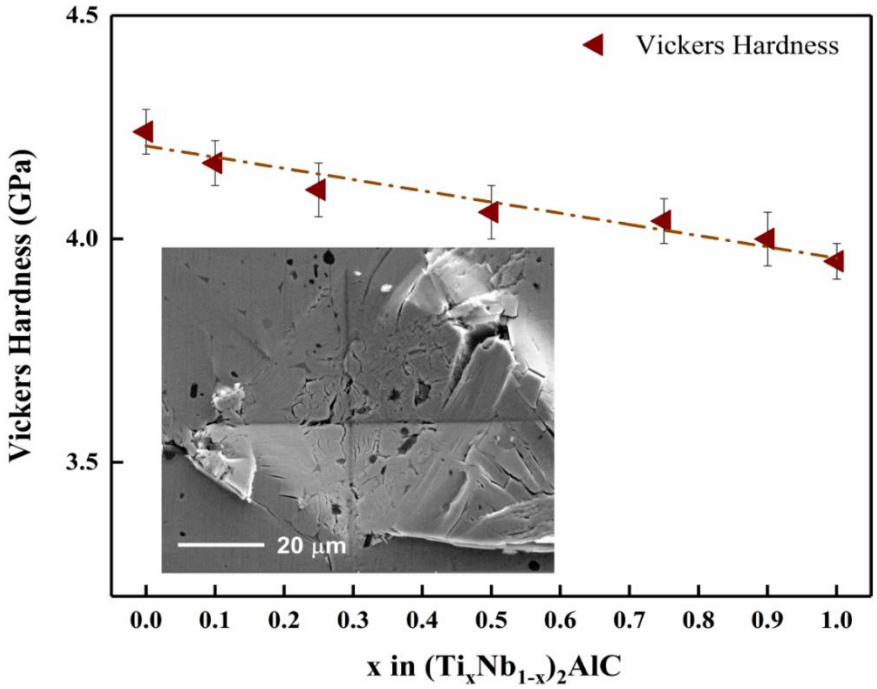

Figure 3-8 The Vickers hardness of $(Ti_xNb_{1-x})_2AlC$ over the full range of composition. Selected but typical SEM image of one of the indents in the sample 75Ti is given in the insert.

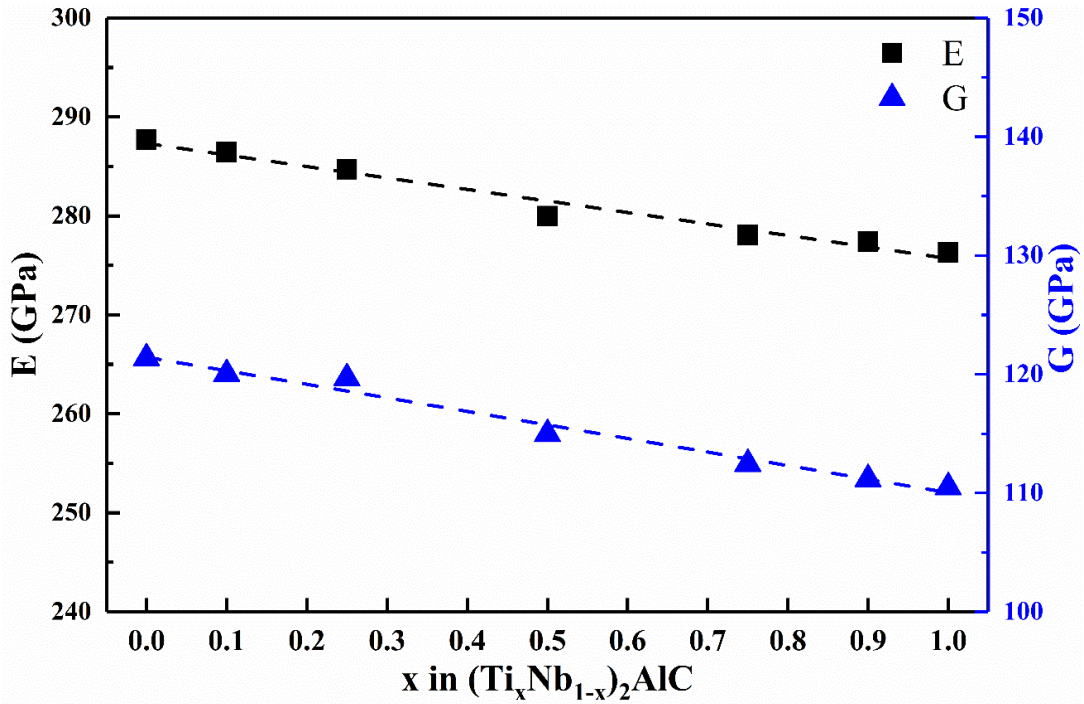

Figure 3-9 Young's and shear moduli of $(Ti_xNb_{1-x})_2AlC$ over the full range of composition. Both moduli decreased almost linearly with increasing amount of Ti in $(Ti_xNb_{1-x})_2AlC$.

3.4. Summary

In summary, predominant single-phase $(Ti_xNb_{1-x})_2AlC$ over full composition were synthesized by PECS. Each composition possesses its unique sintering parameter. A higher percentage of Nb within the green body, a higher sintering temperature is needed until the Nb% reaches 50% where all phase-pure samples were prepared under 1600^oC. The decreasing trend of lattice parameters *a* and *c* with an increasing amount of Ti is in agreement with Vegard's law, which is also represented by Vickers hardness, Young's, and shear moduli. Besides target $(Ti_xNb_{1-x})_2AlC$ solid solution, other tiny amounts of impurities, i.e., niobium aluminum carbides in different stoichiometries, niobium carbides, and titanium carbides were also detected. Elemental analysis confirmed the 211-stoichiometry with Ti and Nb homogeneously arranged on the M-site. Unfortunately, no solid solution strengthening effect was observed while the compressive strength of Nb_2AlC was reported as 1.6 GPa for the first time, which is one of the highest ever reported values for any other MAX phases.

4. SYNTHESIS AND MICROSTRUCTURE OF $(V_xTi_{1-x})_3AlC_2$ WITH x = 0-0.9

4.1. Literature Review

MAX phases are a family of nano-laminated ternary carbides and/or nitrides with a composition of $M_{n+1}AX_n$ (n = 1-3), where M refers to an early transition metal, A corresponds to an element from group 13-16, and X is C or N [2,8,58]. These compounds crystallize layer atomic structure where strongly bonded MX layers are interleaved by a weekly boded A-layer, forming hexagonal *p6$_3$/mmc* structure. Thanks to this, layered structure and combination of atomic bonds within it, MAX phases share many characteristics with both typical ceramics and metals, such as the easy machinability[16], good thermal and electrical conductivity [2], outstanding damage tolerance[4], and excellent corrosion and oxidation resistance at high temperature [3,14].

In addition, MAX phases provide a great opportunity of alloying with other elements on M, A and X sites, providing extra degrees of freedom needed to fine-tune their desired properties. Thus far, more than 100 solid solution MAX phases have been experimentally synthesized [8], and this number is constantly increasing. Noted that some solid solutions can be formed by one or two of its end members which are not otherwise do not form thermodynamically stable MAX phases. For example, Cr_3AlC_2 and V_3AlC_2 were not successfully synthesized, while $(V_{0.5}Ti_{0.5})_3AlC_2$ and $(V_{0.5}Cr_{0.5})_3AlC_2$ were successfully synthesized [13,24].

By solid solution substitution on M, A and X site, the newly synthesized MAX compounds can show significant enhancement of their mechanical, thermal, and chemical properties. For example, Tian *et al.* synthesized $(Cr,V)_2AlC$ by Pulse Electric Current

Synthesis (PECS) and found that the Vickers Hardness was increased with the increasing V content [35]. $(Ti_{0.5},Nb_{0.5})_2AlC$ fabricated by Barsoum *et al.* was reported that has a larger thermal expansion coefficient (TEC) than its two end members [22]. In terms of A-site solid solutions, Gao *et al.* observed a solid strengthening effect of $Ti_3(Si_x, Al_{1-x})C_2$, i.e. the maximum compressive strength (x = 0.4) is 8.8% or 7.3% higher than that of Ti_3SiC_2 and Ti_3AlC_2, respectively [81]. For the solid solution on the X-site, at least 20% of vacancies were confirmed on the C or N site of Ti_2AlC $(C_xN_{1-x})_y$, while a slightly strengthening effect was observed with the variation of x [113].

Of special interest in this paper is $(V_x,Ti_{1-x})_3AlC_2$ solid solution. As for now, only one composition $(V_{0.5},Ti_{0.5})_3AlC_2$ was experimentally synthesized in bulk [24] while V_3AlC_2 end member was only prepared in thin film [114]. Herein, we report the synthesis and microstructure characterization of $(V_x,Ti_{1-x})_3AlC_2$ with x = 0-0.9. By the fact of that up to 90%V atoms substituted Ti in Ti_2AlC bulk samples is somewhat surprising, ad suggest that small amount of Ti can fully stabilize V_3AlC_2 structure in the bulk form.

4.2. Experimental Methods

Commercial powders of vanadium (Alfa Aesar, -325 mesh, 99.5%), titanium (Alfa Aesar, -325 mesh, 99.5%), Al (Alfa Aesar, -325 mesh, 99.5%), and graphite (Alfa Aesar, 7-10 micron, 99%) were selected as starting materials. Different powders mixtures prepared with the molar ratios listed in **Table 1** were ball milled using ZrO_2 beads at 300 rpm for 24 hours and placed in alumina boats for further pressures reactions sintering. Reactions sintering was carried out in a tube furnace (GSL-1600X, MTI, CA, USA) at 1500 ^oC for in a flowing ultra-high purity argon (UHP-Ar). All samples were heated up to

the sintering temperature at the rate of 10 ^{o}C/min . After sintering, the resulting samples were drill milled into the powders, and further sieved to obtain powders with particle size of 38-45 µm for further characterization.

Table 4-1 The target compositions and molar ratios of powder mixtures synthesized in this study.

Sample Name	Target Composition	Nominal Composition of powders
V10	$(V_{0.1},Ti_{0.9})_3AlC_2$	0.3V:2.7Ti:1.3Al:1.95C
V30	$(V_{0.3},Ti_{0.7})_3AlC_2$	0.9V:2.1Ti:1.3Al:1.95C
V50	$(V_{0.5},Ti_{0.5})_3AlC_2$	1.5V:1.5Ti:1.3Al:1.95C
V70	$(V_{0.7},Ti_{0.3})_3AlC_2$	2.1V:0.9Ti:1.3Al:1.95C
V90	$(V_{0.9},Ti_{0.1})_3AlC_2$	2.7V:0.3Ti:1.3Al:1.95C
V95	$(V_{0.95},Ti_{0.05})_3AlC_2$	2.85V:0.15Ti:1.3Al:1.95C

The X-ray Diffraction (XRD) of reaction-sintered $(V_x,Ti_{1-x})_3AlC_2$ was carried out using a D8-Focus X-ray Diffractometer (Bruker, Madison, USA) with a Cu Kα radiation (λ = 1.5406 Å) at 40 kV and 25 mA from $2\Theta = 5^{o}$ - 70^{o}. All samples were scanned at a step size of 0.02° and a scan rate of 1.5 s per step. A zero-background sample holder was used in all the measurements.

To investigate the microstructure of $(V_x,Ti_{1-x})_3AlC_2$ solid solution, the drilled powders were mounted in epoxy resin (Buehler, EpoxiCure^{TM}2), polished with diamond paste down to 1µm and sputter coated with platinum. SEM images were obtained using a combination of Scanning Electron Microscopy (SEM) (FIB-SEM, Lyra-3 Model GMH, USA) and Field Emission SEM (FE-SEM, JEOL-7500, Japan). Both instruments were

equipped with Energy Dispersion Spectrometer (EDS, Oxford, UK) to conduct the EDS analysis.

4.3. Results and Discussion

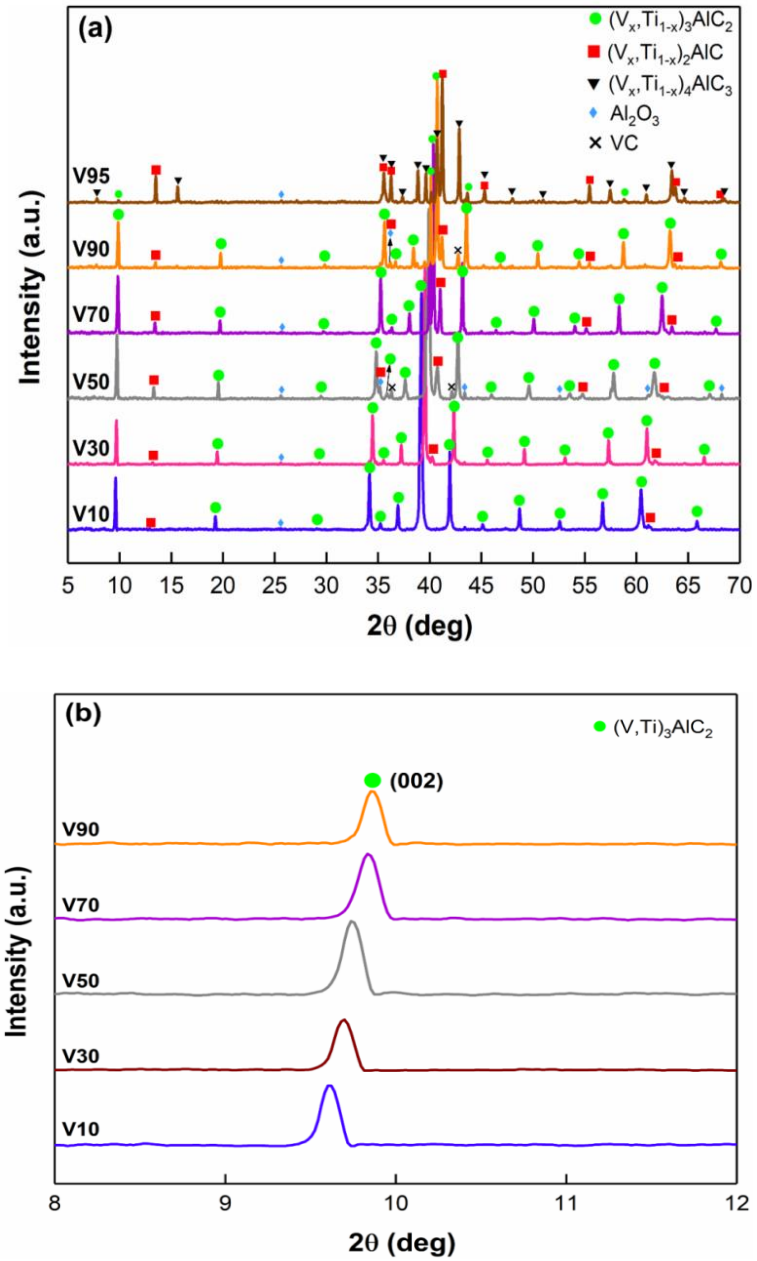

Figure 4-1 (a) XRD patterns of V10-V95. The diffractogram of V95 is different than all the others, indicating a structural transformation occurred. (b) The magnified illustration of (002) peak belonging to $(V_x,Ti_{1-x})_3AlC_2$. The shifting toward a higher 2θ demonstrates the successful replacement of Ti atoms by V atoms.

Figure 4.1a displays the XRD patterns of all as-synthesized $(V_x,Ti_{1-x})_3AlC_2$ solid solutions. In all cases typical XRD peaks for 312 MAX phases can be observed, besides some those belonging to the secondary phases such as 211 MAX phase, Al_2O_3, VC and $(V_x,Ti_{1-x})_4AlC_3$. The magnified area of (002) peak belonging to $(V_x,Ti_{1-x})_3AlC_2$ is represented in **Figure 4.1b**. Note here the predominant side phase $(V_x,Ti_{1-x})_2AlC$ was previously synthesized as the phase pure solid solution in bulk by Gupta *et al.* and Yeh *et al.* who also demonstrated that V_2AlC and Ti_2AlC had the full range of miscibility with each other [115,116].

It is clear from the magnitude of XRD peaks in **Figure 4.1a** that 312 phases, most likely with $(V_x,Ti_{1-x})_3AlC_2$ stoichiometry is the primary phase in samples V10-V90. However, in sample V95 the peak intensity of $(V_x,Ti_{1-x})_3AlC_2$ decreased to a great extent along while those belonging to $(V_x,Ti_{1-x})_2AlC$ and $(V_x,Ti_{1-x})_4AlC_3$ increased. This suggests that $(V_x,Ti_{1-x})_3AlC_2$ starts to decompose when over 90% V atoms replaced Ti in Ti_3AlC_2, favoring the formation of its 211-type and 413-type counterparts according to the following reaction:

$$2\ (V_x,Ti_{1-x})_3AlC_2 = (V_x,Ti_{1-x})_4AlC_3 + (V_x,Ti_{1-x})_2AlC$$

As observed in **Figure 4.1b**, (002) peaks shifted toward a higher 2θ angle with an increase of V content suggesting decrease in lattice parameter with increasing amount of V in the sintered 312 MAX phase. Due to the fact that the covalent radii of V and Ti are 153 pm and 160 pm [117], respectively, this decrease in lattice parameters is expected with substitution of Ti with V in Ti_3AlC_2, which was in turn associated with the observed

shifting and demonstrating the successfully incorporation of V atoms on the M-site of Ti_3AlC_2.

Figure 4.2 displays the changing trend of lattice parameters *a* and *c* over the full composition. Data points of experimentally synthesized Ti_3AlC_2 [118] and $(V_{0.5},Ti_{0.5})_3AlC_2$ [24], and computationally predicted V_3AlC_2 [118] were added for comparison. As can be seen that both *a* and *c* decreased almost linearly with the increasing content of Ti in $(V_x,Ti_{1-x})_3AlC_2$. The wt.% of each phase detected by XRD was obtained by Rietveld refinement and shown in **Figure 4.3**, where target $(V_x,Ti_{1-x})_3AlC_2$ is the predominant phase. Values of lattice parameters and phase contents for each composition is listed in **Table 4-2**.

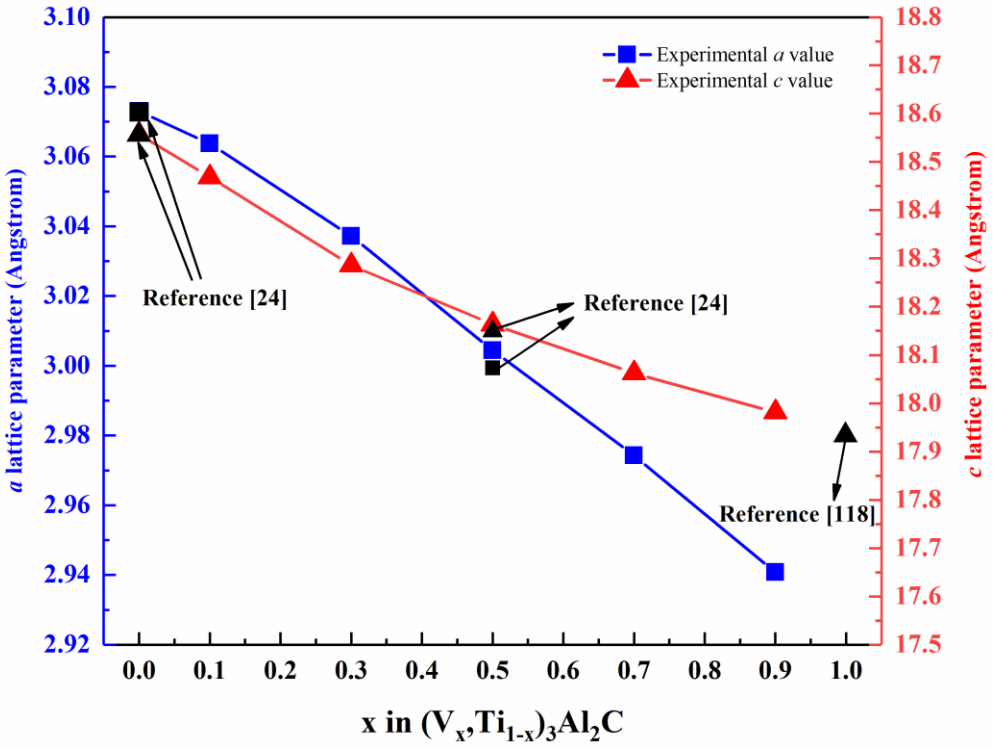

Figure 4-2 The changing trend of LP-*a* and LP-*c* as a function of x in $(V_x,Ti_{1-x})_3AlC_2$. Data points collected from [24] **of Ti_3AlC_2, $(V_{0.5},Ti_{0.5})_3AlC_2$, and** [118] **of V_3AlC_2 are added for comparison as well.**

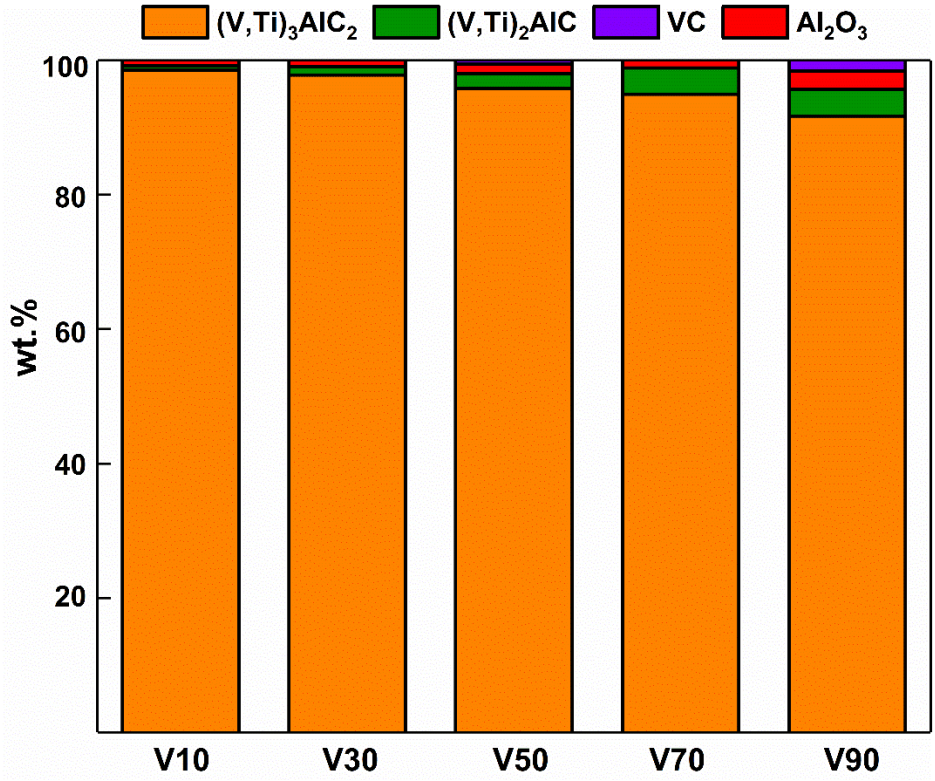

Figure 4-3 The wt.% of each phase within V10, V30, V50, V70, and V90, respectively.

Table 4-2 The lattice parameters *a* and *c*, and content of each phase as determined by Rietveld refinement for each composition. Target $(V_xTi_{1-x})_3AlC_2$ is presented in bold.

Sample Name	LP-*a* (Å)	LP-*c* (Å)	Phase content in wt.%	R_{wp}
V10	3.0637±0.0001	18.4683±0.0014	**98.52 $(V_{0.1}Ti_{0.9})_3AlC_2$**, 0.68 $(V,Ti)_2AlC$, 0.81 Al_2O_3	9.345
V30	3.0372±0.0001	18.2858±0.0010	**97.81 $(V_{0.3}Ti_{0.7})_3AlC_2$**, 1.23 $(V,Ti)_2AlC$, 0.97 Al_2O_3	9.229
V50	3.0044±0.0002	18.1633±0.0024	**95.85 $(V_{0.5}Ti_{0.5})_3AlC_2$**, 2.14 $(V,Ti)_2AlC$, 1.41 Al_2O_3, 0.60 VC	7.923
V70	2.9743±0.0001	18.0622±0.0015	**94.96 $(V_{0.7}Ti_{0.3})_3AlC_2$**, 3.91 $(V,Ti)_2AlC$, 1.13 Al_2O_3	8.391

Table 4-2 Continued

Sample Name	LP-*a* (Å)	LP-*c* (Å)	Phase content in wt.%	R_{wp}
V90	2.9407±0.0002	17.9816±0.0017	**91.71 $(V_{0.9}Ti_{0.1})_3AlC_2$**, 3.95 $(V,Ti)_2AlC$, 2.77 Al_2O_3, 1.57 VC	8.116

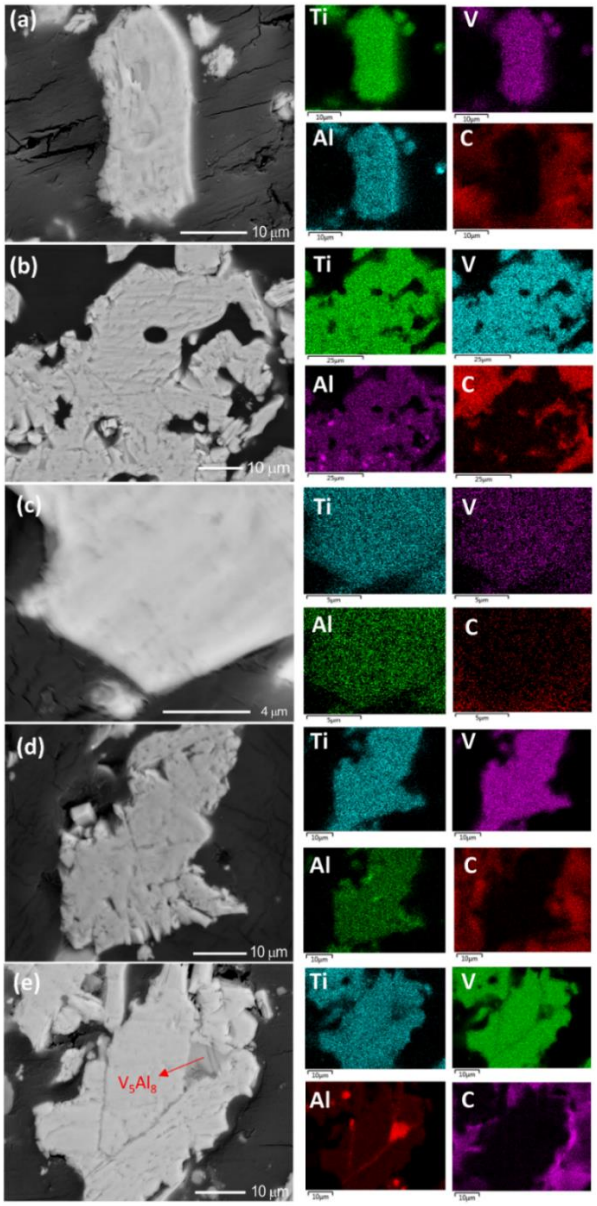

Figure 4-4 Selective but representative SEM images and related EDS mapping results of (a) V10, (b) V30, (c) V50, (d) V70 and (e) V90. A V_5Al_8 grain was detected within the V90, as marked in red in (e). shown here).

Selective but representative SEM images and corresponding EDS maps for samples V10, V30, V50, V70 and V90 are shown in **Figure 4.4a** to **4.4e**, respectively. As can be seen in this figure, vanadium was homogeneously distributed in the target $(V_x,Ti_{1-x})_3AlC_2$ MAX phase. As regard to V90, a V_5Al_8 grain was detected using EDS of which the content is below the one that can be determined accurately by XRD. EDS point analysis (**Figure 4.5**) indicates a quantitative estimation of the atomic ratios, with of (V+Ti)/Al being close to 3, is equal to the stoichiometry of a 312-type MAX phase. SEM-EDS analysis coupled with XRD observations confirm the successfully synthesis of series of $(V_x,Ti_{1-x})_3AlC_2$ solid solutions with x ranging up to 0.9.

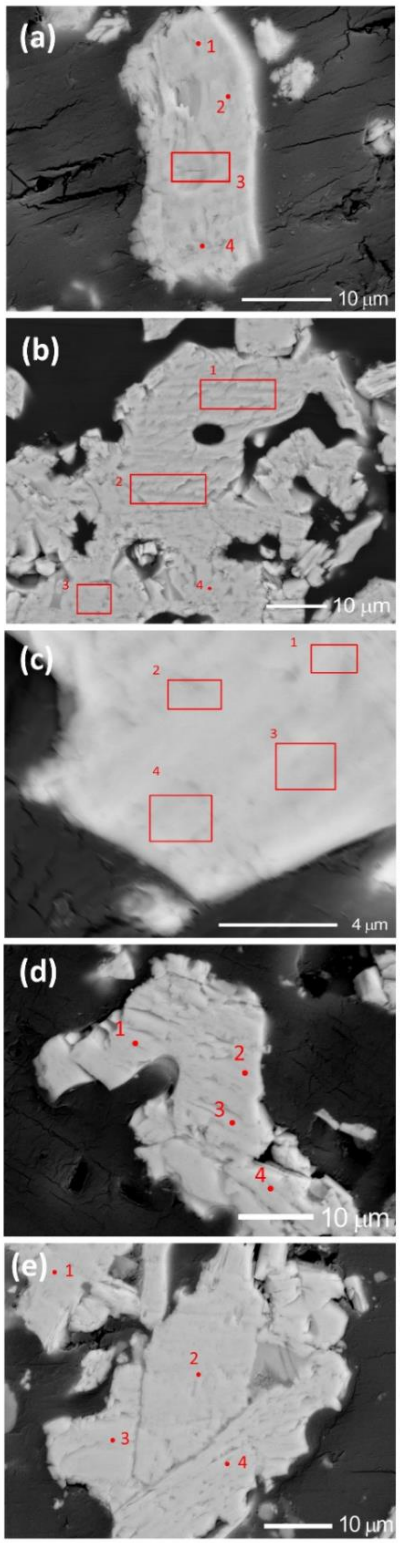

	1	2	3	4	Avg. ± Std. dev.
C	46.00	41.60	40.10	39.40	41.78±2.57
Al	12.90	13.70	14.20	14.30	13.78±0.55
Ti	37.40	41.20	41.70	42.30	40.65±1.92
V	3.70	3.40	4.00	4.00	3.78±0.25
V/(V+Ti)	9.00%	7.62%	8.75%	8.64%	8.50%±0.53%
(V+Ti)/Al	3.19	3.26	3.22	3.24	3.22±0.03

	1	2	3	4	Avg. ± Std. dev.
C	36.03	36.81	40.91	34.54	37.07±2.36
Al	14.60	14.10	14.60	14.50	14.45±0.21
Ti	33.30	32.40	33.20	32.30	32.80±0.45
V	12.10	11.90	12.20	12.40	12.15±0.18
V/(V+Ti)	26.65%	26.86%	26.87%	27.74%	27.03%±0.42%
(V+Ti)/Al	3.11	3.14	3.11	3.08	3.11±0.02

	1	2	3	4	Avg. ± Std. dev.
C	41.70	39.70	42.50	42.50	41.60±1.14
Al	14.30	12.10	14.10	14.10	13.65±0.90
Ti	21.90	19.00	21.70	21.40	21.00±1.17
V	22.10	18.50	21.70	22.10	21.10±1.51
V/(V+Ti)	50.23%	49.33%	50.00%	50.80%	50.09%±0.53%
(V+Ti)/Al	3.08	3.10	3.08	3.09	3.08±0.01

	1	2	3	4	Avg. ± Std. dev.
C	45.50	41.20	42.40	43.90	43.25±1.61
Al	12.90	13.90	13.50	13.20	13.38±0.37
Ti	13.80	15.10	14.70	14.40	14.50±0.47
V	27.90	29.80	29.40	28.40	28.88±0.76
V/(V+Ti)	66.91%	66.37%	66.67%	66.36%	66.57%±0.23%
(V+Ti)/Al	3.23	3.23	3.27	3.24	3.24±0.01

	1	2	3	4	Avg. ± Std. dev.
C	35.90	36.20	35.20	37.10	36.10±0.68
Al	15.60	15.60	15.90	15.30	15.60±0.21
Ti	4.90	4.90	4.90	4.80	4.88±0.04
V	43.60	43.30	44.00	42.80	43.43±0.44
V/(V+Ti)	89.90%	89.83%	89.98%	89.92%	89.91%±0.05%
(V+Ti)/Al	3.11	3.09	3.08	3.11	3.10±0.01

Figure 4-5 EDS point analysis of (a) V10 (b) V30, (c) V50, (d) V70 and (e) V90. Each composition was set 4 points and the averages and standard deviations were listed as well.

4.4. Summary

V_3AlC_2 MAX phase has been theoretically predicted but have not been experimentally synthesized to date due to the system being thermodynamically unstable at room temperature. In this work, Ti is proposed as an alloying element to stabilize the V_3AlC_2 system and synthesize $(V_x,Ti_{1-x})_3AlC_2$ with x ranging from 0 to 0.9. $(V_x,Ti_{1-x})_3AlC_2$ with x=0-0.9 was synthesized by Spark Plasma Sintering (SPS) technique. The phase compounds and microstructure were analyzed by XRD, SEM, and EDS. $(V_x,Ti_{1-x})_3AlC_2$ was no more thermodynamically stable for x is greater than 0.9 due to decomposition into $(V_x,Ti_{1-x})_2AlC$ and $(V_x,Ti_{1-x})_4AlC_3$, which results from the outward diffusion of Al.

5. EFFECT OF MAGNETIC DOPING ON PARAMAGNETIC PROPERTIES OF V_2AlC MAX PHASE

5.1. Literature Review

MAX phases belong to the group of layered ternary carbides and/or nitrides, with a general chemical formula of $M_{n+1}AX_n$ (n = 1-3), where M is an early transition metal, A stands for mostly group 13-16 elements, and X is carbon and/or nitrogen [8,58]. MAX phases crystallize in hexagonal $P6_3/mmc$ structure, with layered structure in which strongly bonded M_6X octahedra are interleaved with weakly bonded A element layers [59]. Because of unique crystal structure and atomic bonding within it, MAX phases possess not only the merits of metals (readily machinability, good thermal and electrical conductivity, excellent damage tolerance) [2,4,16], but also ceramic-like properties (elastically stiff, resistant to thermal shock, outstanding corrosion and oxidation resistance at high temperatures) [3,4,14,15].

Magnetic MAX phases have attracted substantial attention since magnetism combined with the layered structure makes them promising candidate material for many applications, including spintronic and data storage [43]. The first theoretically predicted and experimentally synthesized magnetic MAX phase $(Cr,Mn)_2GeC$ was reported in 2013 which was prepared as a heteroepitaxial single crystal thin film [119]. Concentration of Mn on the M-site in those $(Cr,Mn)_2GeC$ heteroepitaxial single crystal thin films was around 25%, while their magnetic characterization revealed complex magnetic behavior as a result of competition between AFM and FM ground states. In the same year, bulk $(Cr,Mn)_2GaC$ was reaction-sintered by Lin *et al.*, with up to 50% Cr-sites being substituted

by Mn [48]. They reported that the parent Cr_2GaC was transformed from non-magnetic (NM) state to FM-state after the Mn addition. Mockute *et al.* alloyed Cr_2AlC with Mn in the thin-film form with a stoichiometry of $(Cr_{0.84}Mn_{0.16})_2AlC$ by magnetron sputtering [45] and demonstrated a strong magnetic response at and below the room temperature [18], although they didn't observe any magnetic hysteresis, indicating that magnetic moments were either canceling each other out or randomly oriented without an applied field. Later, the same group prepared bulk $(Cr,Mn)_2AlC$ using hot-pressing at 1400^oC for 1 h under Ar flow. Neither apparent FM behavior nor magnetic transitions were detected [46,47].

Somewhat later the thin-film Mn_2GaC was fabricated and its magnetic behavior was characterized by Ingason and collaborators [49–51]. Mn_2GaC was found to show FM behavior at temperature was below 230 K. In addition, the magnetism was found to be anisotropic with a long-range magnetic order [50,51]. Triggered by the synthesis of Mn_2GaC, its solid-solution derivates $(Mo_{0.5}Mn_{0.5})_2GaC$ and $(V,Mn)_3GaC_2$ were also synthesized in the thin-film form later. $(Mo_{0.5}Mn_{0.5})_2GaC$ showed a magnetic response in the temperature range of 3-300 K, which attributed to the competition between AFM and non-linear FM [52]. $(V,Mn)_3GaC_2$ was discovered as the first magnetic 312-class MAX phase, and its FM response was revealed in the 50-300 K temperature range [53].

Several attempts on alloying different MAX phases with Fe on either M-site or A-site have in order to enhance their magnetic properties have been reported. Ouabadi *et al.* prepared Ti_3SnC_2 using Fe as an additive in the starting powder mixture via hot-isostatic pressing (HIPing) [120]. However, no Fe was detected in the Ti_3SnC_2 matrix. Lapauw *et. al*. carried out a follow-up investigation, i.e., adding Fe, Co, and Ni into Pulse Electric

Current Sintered (PECSed) Ti_3SnC_2, Zr_3SnC_2, and Hf_3SnC_2 [121]. Even though they didn't find any Fe-containing MAX phase, the additives were assumed to facilitate the densification and formation of high n-values MAX phases. Fe-incorporated Cr_2GeC was synthesized by Shuai Lin *et al*. [122]. The as-prepared $(Cr_{1-x}Fe_x)_2GeC$ was claimed to be FM due to the substitution of Cr with Fe. However, the insufficient microstructure characterization and the lack of reporting actual amount of Fe within the MAX phase suggests that observed magnetic behavior might be affected by detected Fe containing secondary phases. Hamm *et al*. fabricated bulk Fe-doped Cr_2AlC with the Fe concentration on Cr-site up to approximately 2 at.% using the combination of microwave heating and PECS techniques [123]. They claimed that neither the Fe-doped nor the parent Cr_2AlC MAX phases were FM. Regarding alloying MAX phases with Fe on A-site, Lai *et al*. successfully substituted up to 50 at.% Mo with Fe in Mo_2GaC through a solid-state substitution reaction [124], but they didn't report further details on the magnetic property of this new MAX phase solid solution phase. Most recently, Li *et al*. discovered that besides Fe, other magnetic elements, such as Co, Ni, and Mn or their combinations could also be intercalated in Sn layers of V_2SnC [54]. The alloyed $V_2(A_xSn_{1-x})C$ (where A is a combination of Fe, Co, Ni, and Mn) showed enhanced magnetic behavior.

Inspired by our previous work [55], showing a negative energy hull for $(V_{1-x}Fe_x)_2AlC$ at the ground state, indicating the sizeable thermodynamic stability of this family of solid solutions, the series of $(V_{1-x}Fe_x)_2AlC$ were synthesized and characterized in this study. To the best of the knowledge of authors, this is the first study reporting on phase stability and magnetic behavior of $(V_{1-x}Fe_x)_2AlC$ MAX phase solids solutions.

5.2. Experimental Methods

Experimental Procedure: Commercial powders of V (Alfa Aesar, -325 mesh, 99.5%), Fe (Alfa Aesar, -325 mesh, 98%), Al (Alfa Aesar, -325 mesh, 99.5%), and C (Alfa Aesar, 7-10 micron, 99%) were used to prepare all samples in this study. The powder mixtures prepared with different molar rations of elemental powders as listed in **Table 5-1** were ball-milled with ZrO_2 beads for 6 hours at 300 rmp in a glass jar and transferred into a 20 mm graphite die. Note here that smaller amount of carbon was added into the starting mixtures than that required by targeted MAX phase stoichiometry because graphite die serves as additional source of carbon during sintering. The whole unit was placed into the Pulse Electric Current Sintering system (DCS25, Thermal Technology LLC, CA), heated up to 1250 ^oC with a rate of 100 ^oC/min under flowing ultra-high purity argon (UHP-Ar). In addition, sintered samples were post-annealed in a tube furnace (MTI Corporation, CA) at 1250 ^oC for 2 hours in the flowing UHP-Ar. As a reference, pure V_2AlC was prepared as well. It is important to note that to obtain the V_2AlC and $(V_{1-x}Fe_x)_2AlC$ solid solutions, more than 65 different nominal stoichiometries and synthesis routines were probed, only those resulted in highest phase purity are listed in **Table 5-1** and furthered examined in this study.

Table 5-1 The nominal compositions and sintering parameters of as-prepared samples in this study.

Sample	Nominal Compositions	Nominal Molar Ratios in Staring Powders	PECS				Post-annealing		
			Soaking Temp. ^oC	Heating Rate ^oC/min	Dwell Time min	Pressure MPa	Soaking Temp. ^oC	Heating Rate ^oC/min	Dwell Time hours
S0	V_2AlC	V:Al:C=2:1.1:0.95	1400	20	15	15	-		
S1	$(V_{0.9},Fe_{0.1})_2AlC$	V:Fe:Al:5C=1.8:0.2:1:0.95	1250	100	15	15	1250	10	2
A-S1			Entire sample S1 was powderized						
M-S1			The middle of S1 was drill milled						
E-S1			The middle of S1 was drill milled and etched in 30% HCl for 20 minutes.						
S2	$(V_{0.8},Fe_{0.2})_2AlC$	V:Fe:Al:C=1.6:0.4:1.0:0.95	1250	100	15	15	1250	10	8

To conduct the magnetometry measurement, pure V_2AlC and S1 were entirely drill-milled into powders, loaded into a polypropylene capsule, and applied tested under magnetic field ranging from -7 to +7 T at 300 K using a Superconducting Quantum Interference Device (SQUID, Quantum Design, United States). The reason described in detail is in subsequent text. Only the middle part of sample S1 was drill-milled into powders and were further tested using SQUID before (sample AS1) and after (sample ES1) etching powders in 30% HCl for 20 min, as it is illustrated in **Figure 5.1**.

The phase composition of all reaction sintered samples was examined by X-ray Diffraction (XRD, Bruker, Madison, USA) using Cu Kα radiation (λ = 1.5406 Å) at 40 kV and 40 mA. XRD were collected in 5° - 70° 2θ range with the step size of 0.019° and the time per step of 0.4 s. Rietveld refinement (TOPAS, V4.2, Bruker, Madison, USA) was performed to obtain the weight fraction of each phase detected in sintered samples. Microstructure characterization was conducted using scanning electron microscope (SEM, FIB-SEM, Lyra-3, Tescan, Switzerland) equipped with Energy Dispersion Spectrometer (EDS, Oxford, United Kingdom). High resolution transmission electron microscopy (HRTEM) was performed using on FEI Titan^3 (Thermo Fisher, UK) equipped with Super-X EDS system (Oxford, United Kingdom) using acceleration voltage of 300 kV at Linköping University, Linköping, Sweden.

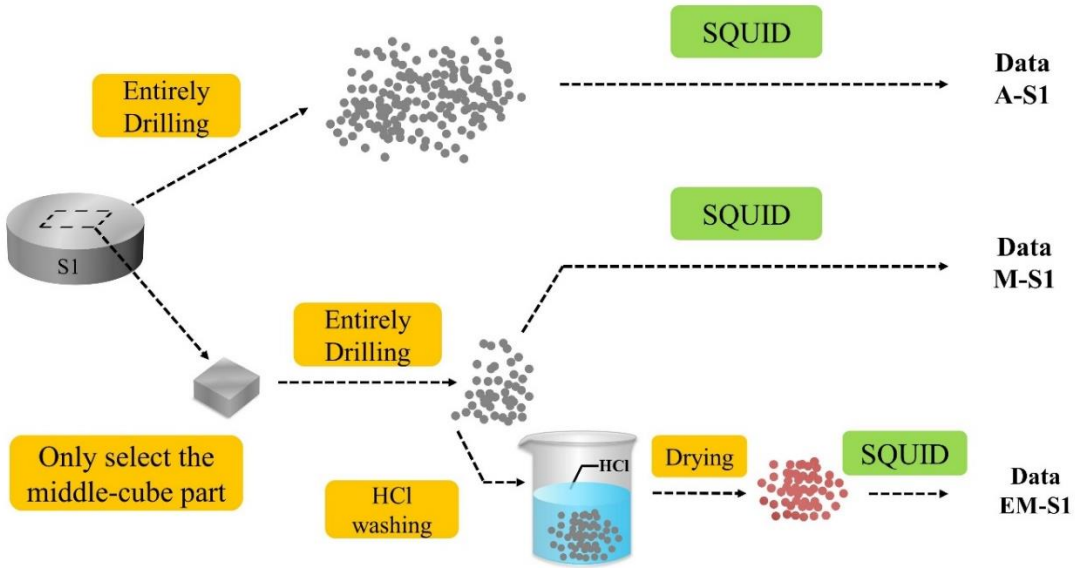

Figure 5-1 The schematic of preparing S1 samples for SQUID measurement.

Density functional theory (DFT): DFT-based Vienna *Ab-initio* Simulation Package (VASP) [125,126] was used for structural minimization, total energy, and formation enthalpy calculation of M-site disorder V-Fe-Al-C MAX phases. The disorder supercell is generated using a special quasi-random supercell (SQS) approach [126] as implemented within the Alloy Theoretic Automated Toolkit [127]. The forces and total energies are converged to 0.001 eV/Å and 10^{-5} eV/cell, respectively. The gamma-centered Monkhorst-Pack [127] *k*-mesh of $5 \times 5 \times 3$ and $9 \times 9 \times 7$ for the geometry-optimization and charge self-consistency, respectively. The Perdew, Burke, and Ernzerhof (PBE) generalized gradient approximation is used with a plane-wave cut-off energy of 533 eV [128]. The phase stability (formation enthalpies) of MAX phases is estimated with respect to elemental (V, Fe, Al, C) ground state energies.

5.3. Results and Discussion

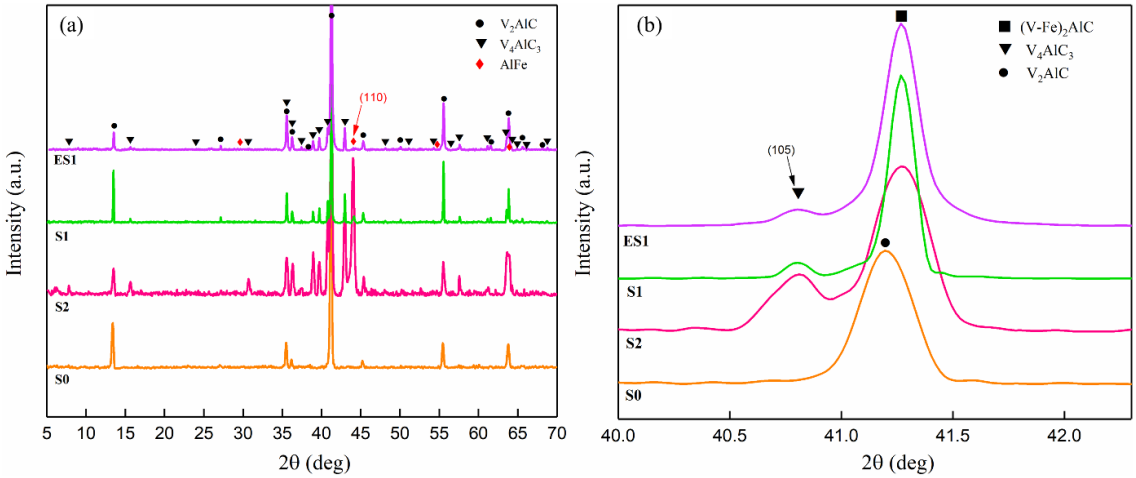

Figure 5-2 XRD results for samples (a) S0 (orange), S1 (green), ES1 (purple), and S2 (pink). (b) is the enlarged area around (103) peak of V_2AlC.

Table 5-2 Phase coposition of the sintered samples as determined using Rietveld refinement from XRD and R_{wp}.

Sample	phase content in wt.%	R_{wp}
A-S1	**68.71 $(V_{1-x}Fe_x)_2AlC$**, 18.23 V_4AlC_3, 13.06 AlFe	3.53
E-S1	**81.20 $(V_{1-x}Fe_x)_2AlC$**, 18.80 V_4AlC_3, 0.00 AlFe	5.41
S2	**31.22 $(V_{1-x}Fe_x)_2AlC$**, 43.90 V_4AlC_3, 24.88 AlFe	2.54

Figure 5.2a shows the X-Ray diffractograms for samples S0, S1, ES1, and S2, respectively, while the enlarged area around (103) peak for V_2AlC phases is highlighted in **Figure 5.2b**. XRD results for sample S0 confirms presence of pure V_2AlC, other secondary phases that are commonly reported in V_2AlC samples prepared using PECS were not observed [32,129]. With the addition of Fe to the starting powder mixture, apart from V_2AlC phase, V_4AlC_3 as well as AlFe intermetallic phase can be detected in XRD results, as it is illustrated for both S1 and S2 samples in **Figure 5.2a**. It is obvious from comparing the relative intensities of XRD peaks for samples S1 and S2 in **Figure 5.2a**

that amount of AlFe and V_4AlC_3 increase noticeably with increasing amount of Fe in the starting powder mixtures. In addition, AlFe is barely detectable in XRD results for S1, and completely undetectable in XRD results for the sample ES1 obtained by the acid washing powders extracted from the center of samples S1. This trend is further confirmed by results of Rietveld refinement presented in **Table 5-2,** showing significant decrease in the amount of **(**$V_{1-x}Fe_x)_2AlC$, and increase in the amount of secondary phases with increasing amount of Fe used in starting powders. In addition, **Table 5-2** shows no presence of any AlFe intermetallic phases in sample ES1, confirming its successful removal after washing S1 powders in the HCl. This is particularly important for reasons discussed in more detail later in this manuscript.

Table 5-3 Comparison of experimental and calculated lattice parameters of V_2AlC, $(V_{1-x}Fe_x)_2AlC$, and Fe_2AlC.

	V_2AlC		**$(V_{1-x}Fe_x)_2AlC$**		**Fe_2AlC**	
	Experimental (XRD)	**Calculated (DFT)**	**Experimental (XRD)**	**Calculated (DFT)**	**Calculated (DFT)** [130]	**Calculated (DFT)**
a (Å)	2.913	2.8906	2.911	2.914	2.842	2.889
c (Å)	13.14	13.1304	13.121	12.963	11.935	11.811

A careful comparison of the position of (103) XRD peak of V_2AlC and **(**$V_{1-x}Fe_x)_2AlC$ for samples S0 and S1 in **Figure 5.2b**, shows its shifts towards a higher 2θ angle, suggesting slight decrease in corresponding lattice parameter by solid solution of Fe in V_2AlC. This is expected as covalent radii of Fe and V are 132 pm and 153 pm, respectively [117], henceforth, decrease in lattice parameters signifies the successful replacement of V with Fe in V_2AlC. However, (103) XRD peak remains at almost same 2θ angle for samples S1 and S2, suggesting no significant difference in the amount of Fe in **(**$V_{1-x}Fe_x)_2AlC$. Therefore, the maximum solubility of Fe into V_2AlC had already been

reached in S1 and increasing the amount of Fe would only trigger the formation of secondary phases as it is confirmed by Rietveld analysis (**Table 5-2**). The lattice parameters *a* and *c* of **(**$V_{0.97}Fe_{0.03}$**)**$_2$AlC determined by XRD are 2.911 Å and 13.121 Å, respectively, and thus they lies between the corresponding reported values for hypothetical Fe_2AlC [44] and V_2AlC [131], **Table 5-3**. Note that Fe_2AlC has never been experimentally synthesized and only the simulative lattice parameters were reported using the DFT method. The lattice parameters for V_2AlC, **(**$V_{1-x}Fe_x$**)**$_2$AlC, and Fe_2AlC calculated in this study using DFT calculated are also listed in **Table 5-3** and they are in good agreement with the experimental result and previously reported values [44,131]. The fact that lattice parameter *c* decreases by alloying V_2AlC with Fe following Vegard's law, suggests that Fe is most likely positioned on M-site in V_2AlC, and not on the A-site, because covalent radius of Fe is smaller than that of V, but larger than that Al (121 pm) [117]. In addition, no shift of the (105) XRD peak for V_4AlC_3 (marked by a black triangle in **Figure 5.2b**) can be observed, suggesting that solid solution of Fe in V_4AlC_3 is negligible.

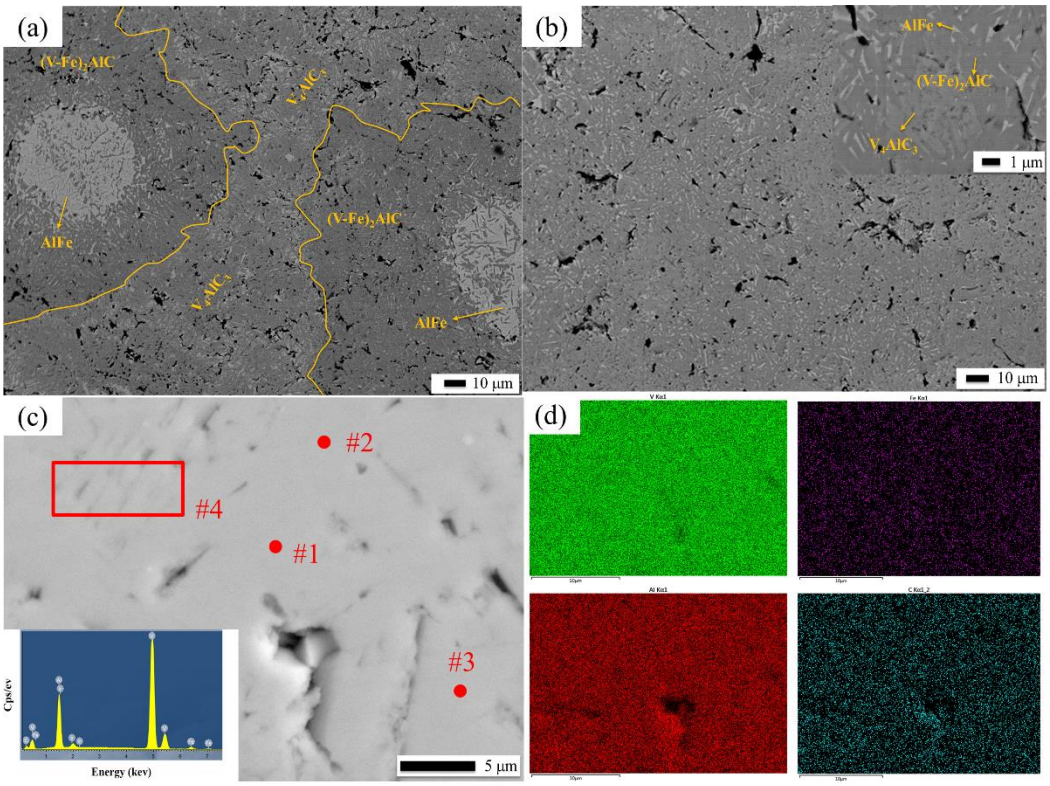

Figure 5-3 BSE-SEM images of (a) S2, (b) S1 and (c) ES1. Insert in (b) shows higher magnification BSE-SEM image of sample S1, while insert in (c) shows EDS spectra for area marked with red rectangle. The locations of EDS point analysis are marked with red points in (c) while EDS results are provided in Table 4. (d) is the EDS mapping of the area in (c).

Table 5-4 EDS point analysis of $(V_{1-x}Fe_x)_2AlC$ phase in Figure 3c.

Element	#1	#2	#3	#4	Avg±Std.dev.
V, at.%	46.39	45.78	47.16	47.17	46.63±0.58
Fe	1.5	1.66	1.48	1.24	1.47±0.15
Al, at. %	24.05	23.54	23.78	22.39	23.44±0.63
C, at.%	28.07	29.01	27.59	29.2	28.47±0.66
(V+Fe)/Al	1.99	2.02	2.05	2.16	2.05
Fe/(V+Fe)	0.03	0.03	0.03	0.03	0.03

Figure 5.3 shows representative backscattered secondary electron (BSE) SEM images of the reaction-sintered samples S2, S1 and ES1. **Figure 5.3a** clearly show that sample S2 contains a large amount of light gray phase that was identified by EDS as

intermetallic AlFe (EDS results not shown here), MAX phase that were identified by EDS as **(**$V_{1-x}Fe_x)_2AlC$ was detected in between AlFe and V_4AlC_3 regimes. On the other hand, BSE-SEM image of sample S1 under same magnification (**Figure 5.3b)** shows more uniform microstructure containing primarily **(**$V_{1-x}Fe_x)_2AlC$ phase as identified using EDS (not shown here) and significantly smaller amount of uniformly distributed AlFe and V_4AlC_3 phases. **Figure 5.3c** shows BSE-SEM image and areal EDS results for sample ES1 prepared by drill milling center of S1 sample and subsequent washing of the obtained powder in HCl, while **Figure 5.3d** shows corresponding EDS maps showing uniform distribution of all elements in that sample. EDS point analysis results for sample ES1 are summarized in **Table 5-4,** and they clearly suggest presence of $(V_{0.97}Fe_{0.03})_2AlC$ phase as (V+Fe)/Al atomic ratio in all points is close to 2, while Fe/(V+Fe) is close to 0.03. This clearly suggest that only around 3 at.% or V has substituted by Fe in sample S1, regardless of the fact that targeted composition of this sample was $(V_{0.9}Fe_{0.1})_2AlC$. In addition, at.% of Fe in **(**$V_{1-x}Fe_x)_2AlC$ phase was detected by EDS in sample S2 prepared to have targeted composition of $(V_{0.8}Fe_{0.2})_2AlC$, suggesting that 3 at.% is solid solubility limit of Fe on V-site in V_2AlC. This is in good agreement with previously discussed XRD results showing no significant difference between lattice parameters of **(**$V_{1-x}Fe_x)_2AlC$ phase in S1 and S2. In addition, this limited solubility of Fe also explains formation of AlFe and V_4AlC_3 secondary phase, whose amount increases with increasing overall Fe amount in starting powder, as excess Fe reacts with Al to form AlFe, triggering also the formation of this Al-deficient V_4AlC_3 MAX phase [93].

The HRTEM image of S1, together with the corresponding EDS results are shown in **Figure 5.4**. The typical atomic structure of 211 MAX phase consisting of two M-Layers (bright atoms) interleaved by an A-layer (dark atoms) is clearly observed in **Figure 5.4a**. EDS results in Figure 4b clearly show presence of V and Al, while the peak corresponding is not clearly visible. Given the limited solubility of Fe substituting the M-sublattice of V_2AlC (up to 3 at.%), the Fe content should accordingly be at an amount near or below the detection limit using this method. However, on the EDS map in **Figure 5.4c** lower magnification clearly show presence of Fe.

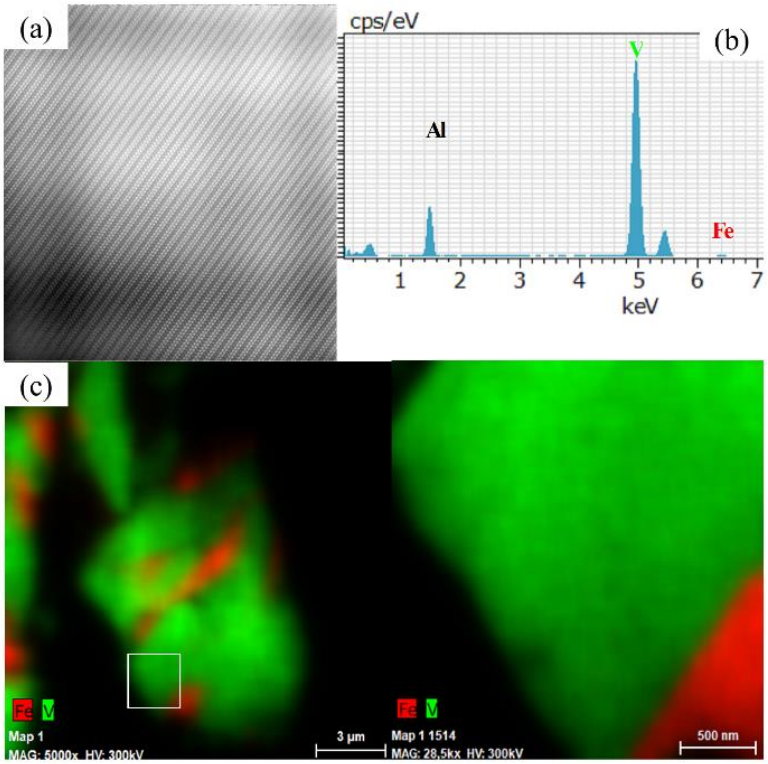

Figure 5-4 (a) HRTEM image of Fe-substituted V_2AlC (S1) with corresponding (b) EDX spectra. (c) EDS map taken at lower magnification.

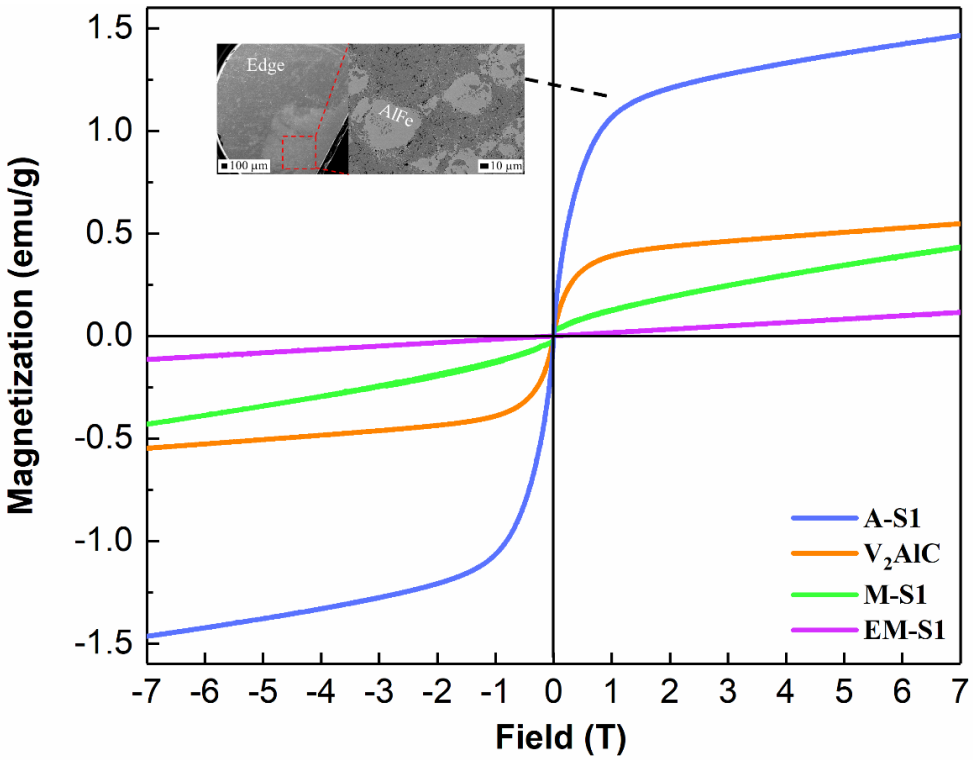

Figure 5-5 Magnetization (emu/g) versus field (T) curves of A-S1 (blue), V_2AlC (orange), M-S1 (green), and EM-S1 (purple) from -7 to +7 T at 300 K.

It is well established by now that the secondary phases within in a sample even in the small amount, could be essential for its magnetic response [44,46]. Therefore, we selected only samples S0 and S1 for further characterization of magnetic properties since sample S2 contained relatively small amount of $(V_{1-x}Fe_x)_2AlC$ phase, and a lot of secondary phases (**Table 5-2**). **Figure 5.5** displays the curves of magnetization (emu/g) versus field (T) of sample S0 (pure V_2AlC) and sample S1 ($(V_{1-x}Fe_x)_2AlC$) at 300K. Note here that S1 powers for magnetic measurements were prepared in three different ways, namely by powdering entire samples (A-S1), powdering only middle of the sample (M-S1), and powdering middle of the sample with subsequent acid washing to dissolve AlFe intermetallic (EM-S1).

Magnetization curves obtained for all four samples show no magnetic hysteresis as it can be seen in **Figure 5.5**. Notably, the pristine V_2AlC was characterized as a reference and the results presented in **Figure 5.5** are in good agreement with other reports [38]. As it can be seen in **Figure 5.5**, sample A-S1 displayed the strongest PM-strength, however, this intensified PM-strength was not arising from presence of $(V_{1-x}Fe_x)_2AlC$ phase, but rather from the presence of relatively large amount (13.05 wt.%, **Table 5-2**) of FM AlFe arrayed primarily around the edges of the sample. It is a common phenomenon that secondary phases arrange along the edges of PECSed samples during reaction sintering due to (i) molten metal (especially low melting point Al) being pushed towards edges by applied pressure before it reacts to form high melting point phases, and (ii) the temperature gradient within the die [82]. The top-left inset in **Figure 5.5**, shows BSE-SEM image of the sample S1 close to the edge with aggregated AlFe along the sample's edges. In stark contrast to the expected increased strength, the PM-strength of M-S1 containing larger amount of $(V_{1-x}Fe_x)_2AlC$ and smaller amount of FM AlFe secondary phase, decreased significantly not only when compared to sample A-S1, but also when compared to pure V_2AlC (sample S0). It has to be noted here that a small amount of AlFe was still discerned in the specimen, but the local magnetic moments brought by this FM intermetallic were still unable to suppress the reduced trend of PM-strength. Due to the close analogy between AFM with PM phase, i.e., zero overall magnetic moment [47], we believe that substituting Fe on M-site (vanadium) increases the electronic imbalances between Fe and V, which results in reduced PM-strength as also discovered in the case for $(Cr_{1-x}Mn_x)_2AlC$ [132]. This speculation is further evidenced as AlFe was completely

removed from the powder with the aid of HCL-etching to obtain sample E-S1 with no AlFe intermetallic phase (**Table 5-2**). The obtained results for EM-S1 in **Figure 5.5** show even further decrease in magnetization. Because of the complete removal of FM AlFe from that sample, the detected PM signal was primarily stemming from the Fe-doped V_2AlC, i.e., $(V_{0.97}Fe_{0.03})_2AlC$. Compared to the pristine V_2AlC, the PM-strength of E-S1 decreased to a great extent. Without the presence of AlFe, the competition between PM and AFM became more noticeable, decreasing the overal PM-strength further at 300 K.

To further investigate the thermodynamic stability of $(V_{1-x}Fe_x)_2AlC$, the formation energies (E_{form}) of it was calculated using: $E_{form} = E_{total}^{alloy} - \sum_i E_i$, where E_{total}^{alloy} is the total energy of ($(V_{1-x}Fe_x)_2AlC$, E_i is the elemental energy in their reference phases, and 'i' labels elements (V, Fe=b.c.c.; Al=f.c.c., and C=graphitic phase). If $E_{form} < 0$, then the $(V_{1-x}Fe_x)_2AlC$ MAX phase is predicted as stable during the sintering procedure, while $E_{form} > 0$ indicates it is a thermodynamically unstable phase. The negative E_{form} (=-0.473, see **Table 5-6**) of single-site disorder $(V_{1-x}Fe_x)_2AlC$ shows that the alloy is thermodynamically more stable, whereas comparing to pure phase [133], it shows a slight decrease in stability compared to, i.e., E_{form} [V_2AlC] < E_{form} [$(V_{1-x}Fe_x)_2AlC$]. The reduced energy stability of $(V_{1-x}Fe_x)_2AlC$ is in accordance with our experimental observation that the amount of targeted 211-configuration decreased with increasing Fe content, whereas the contents of competing phases such as AlFe and V_4AlC_3 increase.

Table 5-5 DFT calculated Fe-moment, average bond-length (V-C; Fe-C), and formation enthalpy of $(V_{1-x}Fe_x)_2AlC$.

Method/System	V_2AlC	$(V_{1-x}Fe_x)_2AlC$	Fe_2AlC
Fe Moment (μ_B)	--	1.27	2.1
BL_{avg} (V-C)	2.017 Å	2.0154 Å	--
BL_{avg} (Fe-C)	--	2.0166 Å	1.927 Å
E_{form} (eV/atom)	-0.487	-0.473	-0.103

To further understand the stability, we analyze the relaxed structures of ordered (V_2AlC/Fe_2AlC) and $(V_{1-x}Fe_x)_2AlC$. The calculated average V-C (V_2AlC) and F-C (Fe_2AlC) bond-length in pure phases are 2.017Å and 1.927Å, respectively [133]. The $(V_{1-x}Fe_x)_2AlC$ shows a significant increase in the average bond-length of Fe-C from 1.927Å to 2.0166 Å whereas the average V-C bond-length remains unchanged (V-C=2.0154 Å). The increased Fe-C bond-length indicates the reduced covalent nature of the Fe-C bond due to reduced charge sharing. The weakening of bond strength reduces the energy stability of the doped MAX phase. This originates from the fact that longer bonds need less energy to break, therefore, less stable. The Fe-doping to paramagnetic V_2AlC shows weakly reduced energy stability of with ΔE_{form} [$(V_{1-x}Fe_x)_2AlC$ - V_2AlC] is only +14 meV, which is equivalent to 162 K on temperature scale. This also indicates the competing nature of paramagnetic V_2AlC and AFM $(V\text{-}Fe)_2AlC$.

To shed more light, we plotted the total density of states (TDOS) for PM-V_2AlC and AFM$(V_{1-x}Fe_x)_2AlC$ in **Figure 5.6a**, which shows common features of MAX phases [134]. The structure of the density of states at Fermi level (F_{Fermi}, vertical dashed line) can also be interpreted in terms of structural stability of MAX phases. Valley in the density of states at E_{Fermi} is indicative of stability whereas the peak in the density of state at E_{Fermi}

shows structural instability. Based on this analysis, the position of E_{Fermi} of the valley in TDOS of V_2AlC (red) corresponds to the weaker peak in TDOS of $(V_{1-x}Fe_x)_2AlC$. The energy difference between peak and dip in TDOS works as an energy barrier for charges to move from occupied states below E_{Fermi} to unoccupied states above E_{Fermi}. Since Fe has more valence electrons than V, Fe doping pumps excessive charges that fill some unoccupied bonding V-*d* states above E_{Fermi}. This band-filling moves the E_{Fermi} from the valley of V_2AlC TDOS at E_{Fermi} towards peak point due to band-filling, which weakly destabilizes $(V_{1-x}Fe_x)_2AlC$. This is also reflected in the calculated formation enthalpies in **Table 5-6**. The charge imbalance induced by Fe addition to V_2AlC reduces the paramagnetic strength of V_2AlC. The contour plots of charge densities for V_2AlC and $(V_{1-x}Fe_x)_2AlC$ in the M-C atomic plane are shown in **Figure 5.6b-c**. A significant delocalization of electrons near Fe-site due to the increased Fe-C bond-length in $(V_{1-x}Fe_x)_2AlC$, i.e., weaker covalent Fe-C bonding compared to Fe_2AlC in **Table 5-6** was also found.

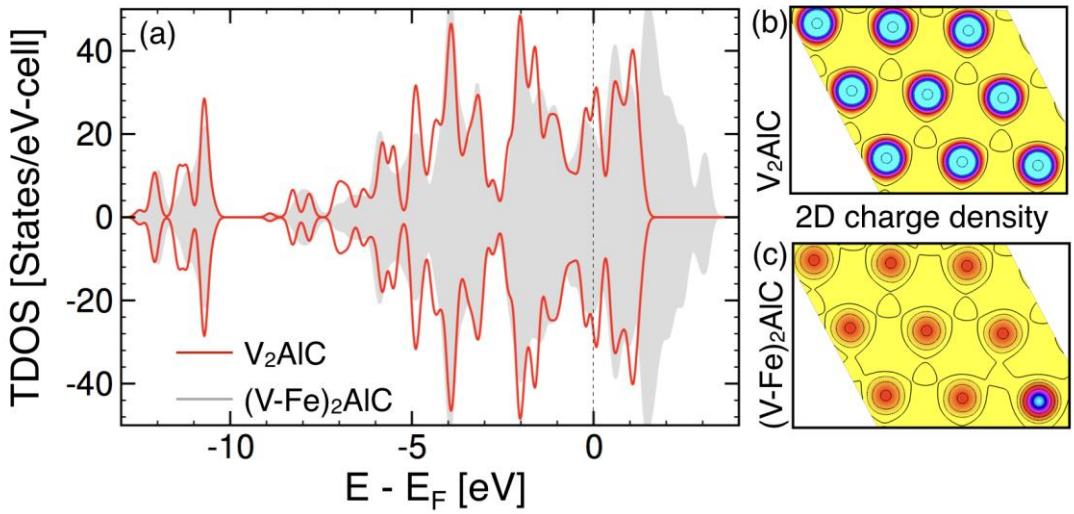

Figure 5-6 (a) Total density of states, and (b-c) contour map of electronic charge densities of V_2AlC and $(V_{1-x}Fe_x)_2AlC$ (3% at. Fe) MAX phases in the M-C atomic plane.

A 3% Fe-substitution to V in V_2AlC adds a quarter more electron per iron, while 3% V deficiency creates 0.15 holes, i.e., Fe pumps 0.09 excess electrons. The increased charge density lobes in **Figure 5.7a** shows slightly increased localized charges on Fe due to the reduced covalent nature of Fe-C bonds, which increases the Fe-C bond-lengths in $(V_{1-x}Fe_x)_2AlC$. This small electronic imbalance created by Fe substitution induces small AFM moments on V and C as shown in the magnetization density plot in **Figure 5.7b-c**. This reduces the paramagnetic strength compared to V_2AlC. We also found the change in the magnetic behavior of Fe in $(V_{1-x}Fe_x)_2AlC$, where Fe moment is significantly reduced to 1.27 μ_B from 2.1 μ_B in Fe_2AlC. In $(V_{1-x}Fe_x)_2AlC$, the polarization of Fe-*d* bands determines the magnetic moment of Fe, whereas the weak V/C moments arise from the delocalized magnetic exchange interaction of Fe-*d* with V-*d*/C-*p* states [133]. The shorter bond length in **Table 5** of Fe_2AlC leads to an increased direct magnetic exchange between Fe and C and local Fe moment. However, the reduced Fe moment arises from increased Fe-C bond length due to the reduced magnetic exchange coupling. The decreasing trend of the magnetic moment was also confirmed by our SQUID measurements that M-S1

represents the reduced magnetic moments compared with V_2AlC, and when all FM AlFe was removed, the measured moments dropped further down.

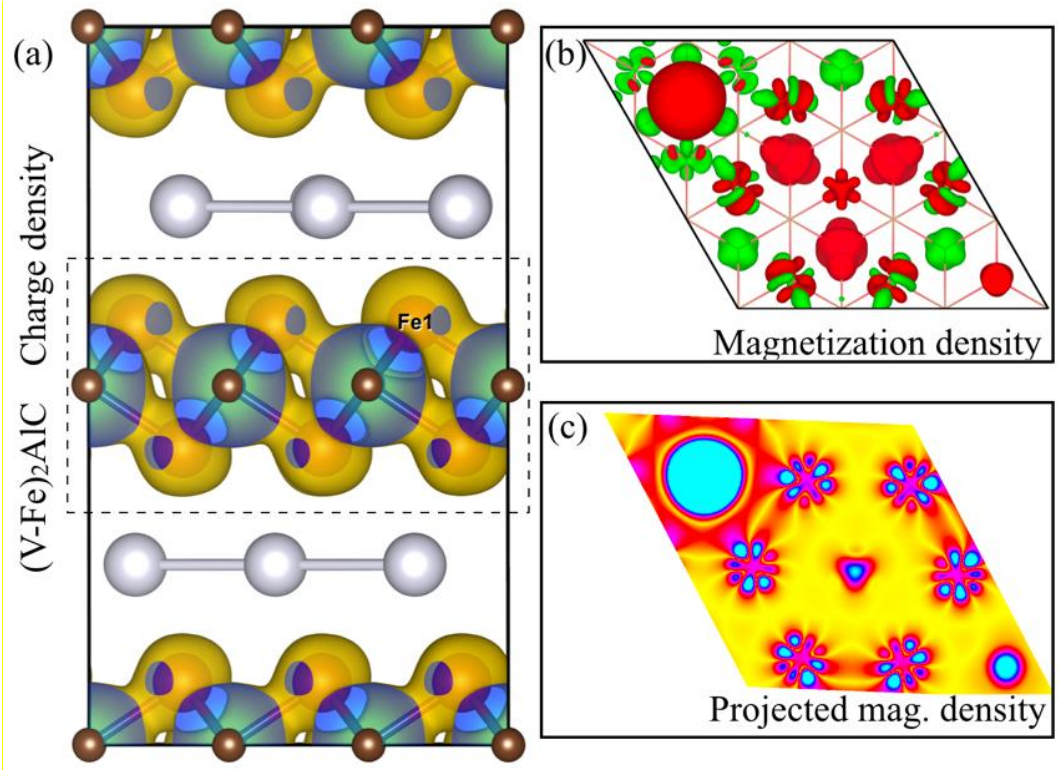

Figure 5-7 (a) $(V_{1-x}Fe_x)_2AlC$ charge density, (b) magnetization density of marked zone (a) along (x-y) plane, and (c) 2D projected magnetization density.

Notably, the magnetic exchange increases the covalent nature of bonding by increased hybridization, which also lowers the energy stability [133]. Chemically doped V_2AlC leads to a change of magnetic phase from PM to AFM whereas PM V_2AlC is slightly more stable. We believe that the unusual competition between PM (V_2AlC) and AFM ($(V_{1-x}Fe_x)_2AlC$) phases arises due to increased Fe-C bond length that weakens the covalent nature of bonding.

5.4. Summary

Highly pure $(V_{1-x}Fe_x)_2AlC$ and V_2AlC were both synthesized using the SPS technique. The maximum solubility of Fe on the M-site of V_2AlC is up to 3 at.%. Beyond the maximum solubility, the $(V_{1-x}Fe_x)_2AlC$ tended to be less thermodynamically stable as more secondary phases (AlFe and V_4AlC_3) were formed. The reduced stability was validated both experimentally and computationally. Replacing V with Fe on M-sublattice of V_2AlC induces the decrease of PM-strength instead of enhancing it, which can be ascribed to the small AFM moments introduced by Fe substitution, resulting in the competition with PM-state of V_2AlC. The possibility of substituting the original M-site atoms with magnetic elements in the V_2AlC phase offers another great potential of fabricating magnetic MXene for further application-oriented studies.

6. PHASE STABILITY OF QUATERNARY CARBIDES IN Nb-Fe/Ni/Co-Al-C SYSTEMS: FORMATION OF η-CARBIDE

6.1. Literature Review

Nb_2AlC is one member of MAX phase family of ternary carbides and nitrides that all share common chemical formula of $M_{n+1}AX_n$ (n = 1-3), where M is an early transition metal, A denotes mostly to group 13-16 elements, and X stands for either C or N. These compounds crystallize in layered hexagonal $P6_3/mmc$ structure with of M_6X octahedra interleaved with atomic A layers [2,8,58]. Compared to conventional binary MX carbides and nitrides, MAX phases combine both merits of metals and ceramics, such as easy machinability, good thermal and electrical conductivity, outstanding damage tolerance, and excellent corrosion and oxidation resistance at high temperature [3,14,17,100]. And thanks to the plentiful number of possibilities of forming substitutional solid solutions in MAX phases on M, A, and X sites, their properties can be easily tailored for particular application [46]. For example, replacing 80% of V atoms with Ti atoms on the M-site of V_2AlC led to a 45% enhancement of the compressive strength [135]; Barsoum *et al.* reported that $Ti_2Al(C_{0.5},N_{0.5})$ was stronger in compression, harder, but more brittle than its end-members [136]; Cai *et al.* found that by partially substituting Al with Si and/or Sn on the A-site of Ti_3AlC_2 resulted in the friction coefficient increased from 0.2 to 0.38 [137].

As of Nb_2AlC, a few studies have been carried out to investigate effects that substitution of Nb with other elements on phase stability and properties of these MAX phases. For instance, Salama *et al.* synthesized $(Nb_{0.5},Ti_{0.5})_2AlC$ from Nb, Ti, C, and Al_4C_3

powder mixture by hot-isostatic pressing (HIP) and showed no solid-solution strengthening due to substitution of Nb with Ti [71]. Bentzel *et al.* reported that the thermal expansion coefficient (TEC) of $(Nb_{0.5},Ti_{0.5})_2AlC$ fabricated by the same technique was slightly higher than that of its end-members [107]. On the other hand, Donchev *et al.* found that the substitution of Ti with small amount of Nb enhances oxidation resistance of Ti_2AlC MAX phase and reduces the oxide scale growth rate [21]. Lapauw *et al.* and Halim *et al.* recently synthesized $(Nb_{0.80},Zr_{0.92})_2AlC$ MAX phase solid solution from $NbH_{0.89}$, ZrH_2, Al and C, and $(Nb_{0.66},Sc_{0.33})_2AlC$ from the elemental powder mixtures, respectively, by pressureless sintering, but did not report on its chemical and physical properties. [25,29].

To the best of our knowledge, there is no report pertaining to investigate possibility of substituting Nb with Fe, Ni or Co on Nb_2AlC. The purpose of this paper is two-fold: first, to investigate phase stability Nb_2AlC with partial substitution of Nb with Fe, Ni and Co; second, to characterize the structure of this newly discovered quaternary carbide η-$(Nb_{0.8},X_{0.2})_4Al_2C$ in Nb-X-Al-C system, where X is Fe, Ni, or Co.

Table 6-1 The target, nominal compositions, molar ratio of powders in the stating mixtures and sintering conditions.

Sample Name	Target Composition	Nominal Composition of powders	Pulsed Electric Current Sintering			Pressureless Sintering
			Heating rate (^{o}C/min)	Dwell Temperature (^{o}C)	Dwell Time (min)	
S1	Nb_2AlC	Nb:Al:C=2:1.15:0.95	25	1600	30	N/A
S2	$(Nb_{0.8},Fe_{0.2})_2AlC$	Nb:Fe:Al:C=1.6:0.4:1.1:0.95	50	1550	15	
S3	$(Nb_{0.8},Fe_{0.2})_2AlC$	Nb_2AlC:Fe:Al:C=0.8:0.4:0.22:0.95	50	1550	15	
S4	$(Nb_{0.97},Fe_{0.03})_2AlC$	Nb_2AlC:Fe:Al:C=0.97:0.06:0.033:0.015	50	1550	15	
S5	$(Nb_{0.8},Fe_{0.2})_4Al_2C$	Nb:Fe:Al:C=3.2:0.8:2.2:0.95	50	1550	30	1550 ^{o}C 5 hours

6.2. Experimental Methods

In this study, powders of niobium (Alfa Aesar, -325 mesh, 99.8%), iron (Alfa Aesar, -325 mesh, 98%), aluminum (Alfa Aesar, -325 mesh, 99.5%), and graphite (Alfa Aesar, 7-10 micron, 99%) were used to reaction sinter samples with targeted compositions of Nb_2AlC, $(Nb_{0.8},Fe_{0.2})_2AlC$, $(Nb_{0.97},Fe_{0.03})_2AlC$, and $(Nb_{0.8},Fe_{0.2})_4Al_2C$, **Table 6-1**. In brief, the powder were mixed in different molar ratios provided in **Table 6-1**, and then ball-milled with ZrO_2 beads for 24 hours at 300 rmp in plastic jars. Mixed powder were transferred into a 20 mm graphite die for reaction sintering by Pulsed Electric Current Sintering (PECS) (PECS25-10, Thermal Technologies LLC, CA) . Samples were first heated to temperature in the 1550-1600 ^oC range at heating rates of 25 or 50 ^oC/min, and then reaction sintered at targeted temperature under for 15-30 min under the load of 10 MPa and continuous flow of ultra-high purity argon (UHP-Ar), **Table 6-1**. Regarding S5, the PECSed sample was additionally post-annealed in a tube furnace (GSL-1600X, MTI, CA) at 1550^oC for 5 hours under the flowing UHP-Ar. It has to be noted here the Nb_2AlC used for samples S3 and S4 was sintered using the sample procedure as for sample S1. Besides Fe, Ni (Alfa Aesar, -325 mesh, 99.8%) and Co (Alfa Aesar, -400 mesh, 99.5%) were added into the starting powder mixtures of Nb, Al and C powders as well (**Table 6-2**). Both green bodies were sintered by PECS under 1550 ^oC for 30 min with the heating rate of 50 ^oC/min and a constant 10 MPa pressure.

Table 6-2 The target, nominal compositions, molar ratio of powders in the stating mixtures and sintering conditions.

Sample Name	Target Composition	Nominal Composition of powders	Pulsed Electric Current Sintering		
			Heating Rate (ºC/min)	Dwell Temperature (ºC)	Dwell Time (min)
S6	$(Nb_{0.8},Ni_{0.2})_4Al_2C$	Nb:Ni:Al:C=1.6:1.1:0.2:0.95	50	1550	30
S7	$(Nb_{0.8},Co_{0.2})_4Al_2C$	Nb:Co:Al:C=1.6:1.1:0.2:0.95	50	1550	30

The cross-section areas of all as-prepared samples were polished down to 1 μm diamond paste. The X-ray Diffraction (XRD) was carried out using a D8-Focus X-ray diffraction (Bruker, Madison, USA) with a Cu Kα radiation (λ = 1.5406 Å) at 40 kV and 25 mA. The step size and time per step were 0.019° and 0.4 s, respectively. All XRD data were collected at 2θ angles ranging from 5° to 60°. Rietveld refinement of X-ray diffractograms was performed using TOPAS V4.2 (Bruker, Madison, USA) to obtain phase composition of the samples and the lattice parameters of all samples. The microstructure and composition analysis were conducted using a Focused Ion Beam - Scanning Electron Microscope (FIB-SEM, LYRA-3, Tescan, Switzerland) equipped with Energy Dispersion Spectrometer (EDS, Oxford, United Kingdom).

The cross-sectional lamella was prepared by the FIB-SEM (LYRA-3) for transmission electron microscopy (TEM, FEI TITAN Themis Z 300, Thermo-Fisher Scientific, UK) equipped with double aberration-corrector correction using acceleration voltage of 300 kV. The composition of phases was analyzed using a high-efficiency X-ray energy dispersive spectroscopy (EDS) facility equipped on TEM. Simulation of the HAADF-STEM images was conducted using the QSTEM simulation developed by Koch [138]. The values of the input HAADF collector angles, the convergence semi-angle of the electron probe and the probe size were the same as described on above paragraphs.

6.3. Results and Discussion

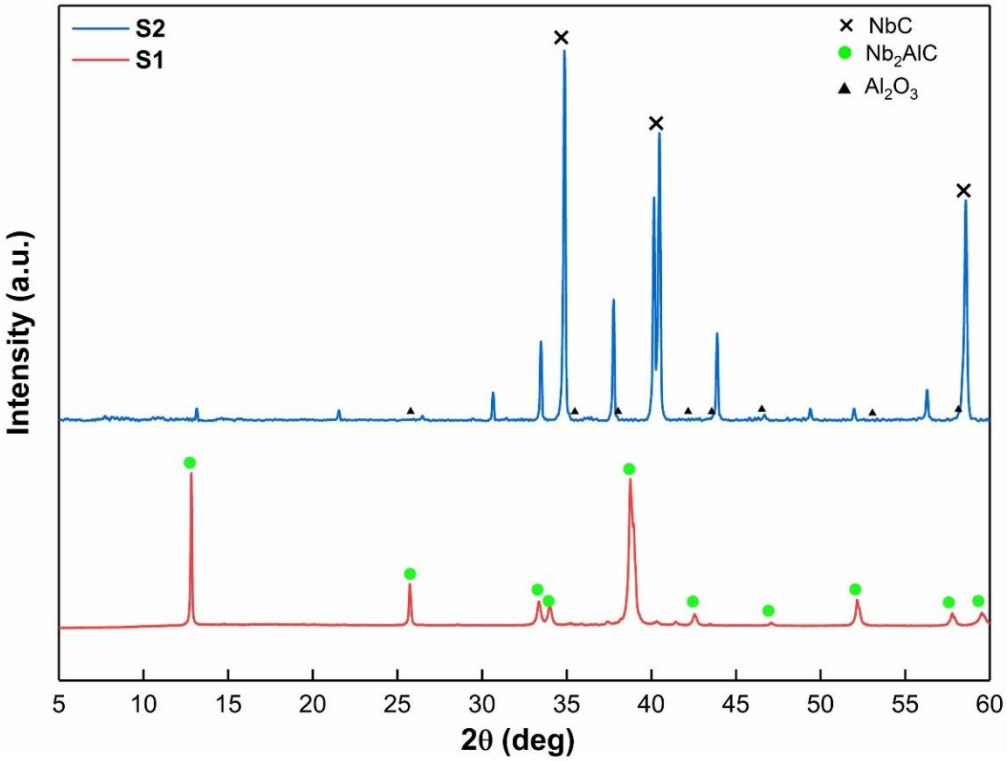

Figure 6-1 XRD patterns of S1 and S2. Some peaks of S2 cannot be indexed as Nb_2AlC any other possible phase in Nb-Fe-Al-C system and they were left unlabeled intentionally.

Figure 6.1 shows the XRD results for samples S1 and S2 which were synthesized from elemental powders. While XRD of S1 sample shows that sample consists of Nb_2AlC as expected, XRD of sample S2 shows presence of NbC and Al_2O_3 besides XRD peaks that could not be indexed as Nb_2AlC or other phases existing in the Nb-Fe-Al-C system. Therefore, we assumed a new phase was formed in S2 with targeted composition of $(Nb_{0.8},Fe_{0.2})_2AlC$. SEM images and EDS results for S2 shown in **Figure 6.2** and **Table 6-3** shows presence NbC and Al_2O_3, besides the third phase containing Nb, Fe, Al and C that could not be indexed in XRD. Presence of NbC and Al_2O_3 detected by EDS-mapping (**Figure 6.2d**) is in good agreement with the XRD result. As can be seen in **Figure 6.2b**,

NbC clusters together in the regions characterized with high porosity while Al_2O_3 particles are uniformly dispersed throughout unknown phase. Noted that Al_2O_3 comes from the impurities in starting Al powder, as it was discussed elsewhere [17,112], while NbC forms during reaction sintering. Results of EDS-points analyses of the unknown phase in **Figure 6.2a** are listed in **Table 6-3**, and they show that unknown phase contains of 33.81 at.% of Nb, 9.29 at.% of Fe, 21.63 at.% of Al, and 35.25 at.% of C. Noted here that amount of carbon is most likely significantly overestimated because EDS's low accuracy in quantifying amount of carbon, and thus its content will not be taken into account in the further analysis of EDS results. EDS results in **Table 6-3** clearly show (Nb+Fe)/Al ratio close to 2 and Fe/(Nb+Fe) ratio close to 0.22, which is approximately equal to those in S2's targeted composition $(Nb_{0.8},Fe_{0.2})_2AlC$. This indicate that all Fe was dissolved within this unknown niobium carbide phase.

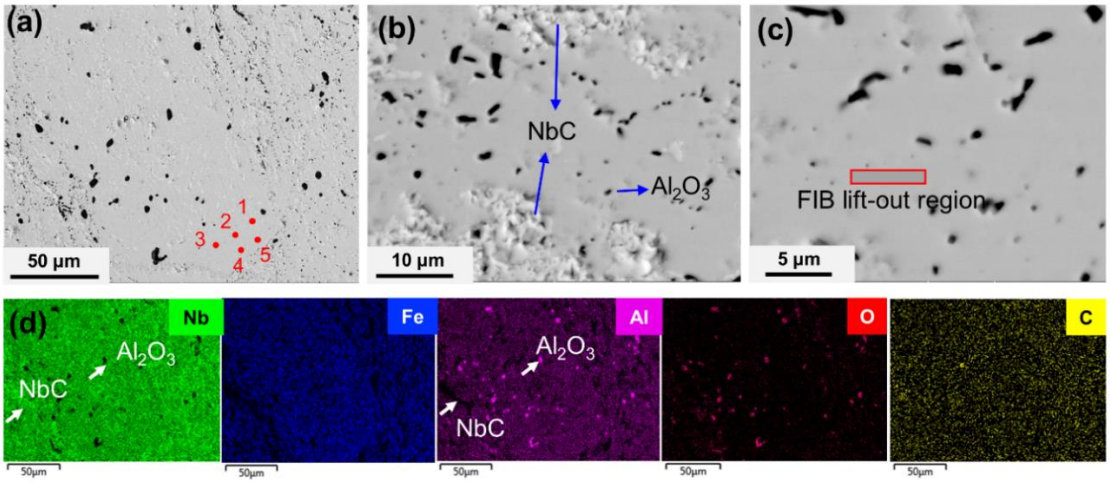

Figure 6-2 (a) Low magnification of SEM image and (d) EDS elemental mapping of S2; (b) high magnification of SEM image to show the three phases (white-NbC, grey-unknown phase, black-Al_2O_3) and (c) the region for FIB lift-out (marked by the red rectangle).

Table 6-3 EDS point analysis of the unknown phase from Figure 6.2

	1	2	3	4	5	Avg. ± Std. dev.
C, at.%	32.40	33.90	39.72	34.24	35.99	35.25±2.51
Al, at.%	23.00	22.40	20.01	21.86	20.87	21.63±1.07
Fe, at.%	10.60	10.50	8.70	8.28	8.39	9.29±1.04
Nb, at.%	34.00	33.10	31.56	35.62	34.75	33.81±1.40
Fe/(Nb+Fe)	0.23	0.24	0.21	0.19	0.19	0.22±0.02
(Nb+Fe)/Al	1.94	1.95	2.01	2.01	2.07	1.99±0.05

To further investigate the unknown phase, a TEM lamella was prepared from the position marked by red rectangle in **Figure 6.2c** by Focus ion beam lift-out method. **Figure 6.3a** is a bright-field TEM image of the unknown phase. The microstructure consists of grains with various orientations, as it can be observed from variation of the image contrast (mainly diffraction-contrast), and several small particles within the grains. To analyze the unknown phase and the particles, EDS analysis was performed on the region marked by red dash rectangle in **Figure 6.3a**. The EDS analysis (**Figure 6.3c** and **d**) clearly confirms presence of Al_2O_3 phases and composition of unknown phase having (Nb+Fe)/Al close to 2 and Fe/(Nb+Fe) close to 0.21. Therefore TEM-EDS results are consistent with the SEM-EDS analysis.

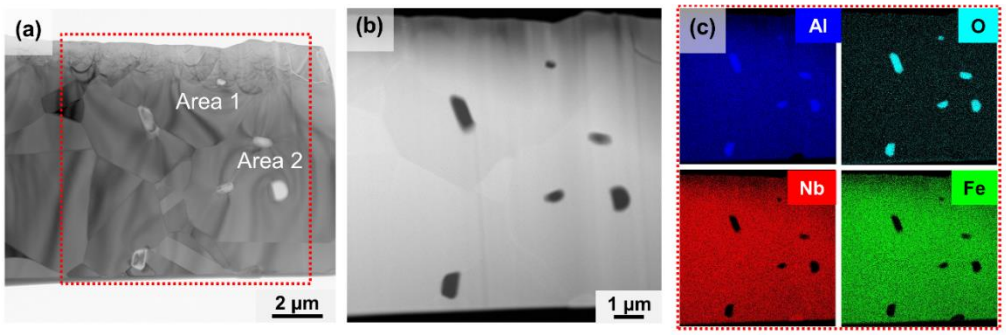

(d) **Chemical composition of the TEM lamella as measured by STEM-EDS results (at. %)**

	1	2	3	4	Avg. ± Std. dev.
C	12.19	5.10	4.64	4.96	6.72 ± 3.65
Al	29.83	32.94	31.95	31.93	31.66 ± 1.31
Fe	12.33	13.07	13.25	13.23	12.97 ± 0.43
Nb	45.65	48.89	50.16	49.88	48.65 ± 2.07
Fe/(Nb+Fe)	0.21	0.21	0.21	0.21	0.21 ± 0.00
(Nb+Fe)/Al	1.94	1.88	1.98	1.98	1.95 ± 0.05

Figure 6-3 (a) Bright-field TEM image; (b) a HAADF-STEM image of the region marked by the red dash rectangle in (a), with the corresponding EDS elemental maps shown in (c). (d) The table of chemical composition in different positions in the TEM lamella.

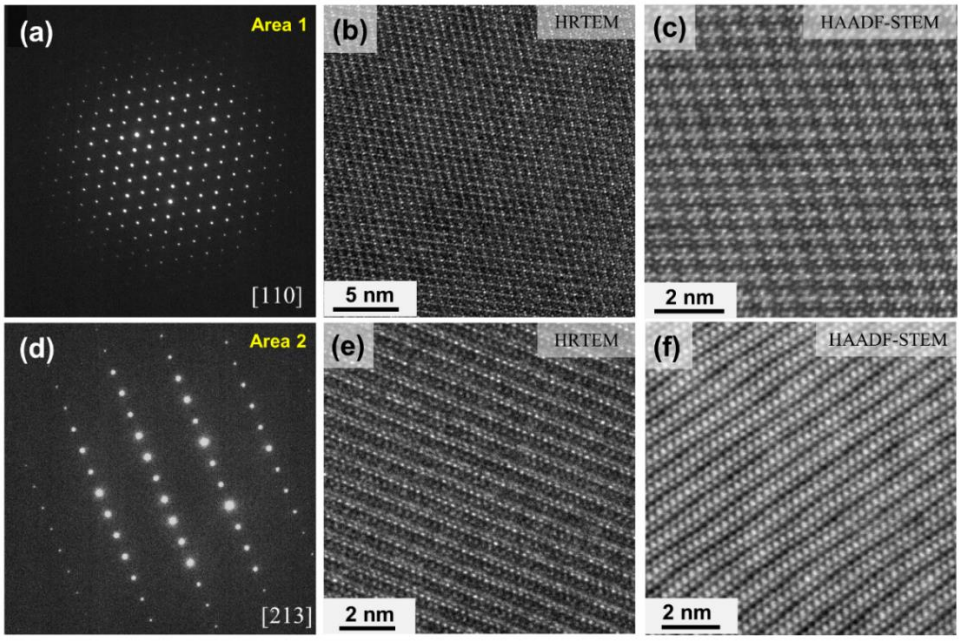

Figure 6-4 TEM results obtained from two areas marked in Fig. 3(a). (a)-(c) SAED pattern, HRTEM and HAADF-STEM images in [110] zone axis from Area 1; (d)-(f) SAED pattern, HRTEM and HAADF-STEM images in [213] zone axis from Area 2.

Two sets of selected area electron diffraction (SAED) patterns of the unknown phase from two areas with a different orientations of grains are shown in **Figure 6.4a** and **6.4d**. The patterns are indexed as a complex FCC structure (M_6C type) in [110] and [213] zone axis, respectively. The lattice is constant of this unknown phase is determined to be a =11.78 Å. Both the crystallographic structure and the lattice constant are consistent with the XRD results and the reported structure of η-carbide in the literature [139–141]. To further characterize structure of that phase, High-resolution TEM images and the HAADF-STEM images are collected along the [110] (**Figure 6.4b** and **6.4c**) and [213] (**Figure 6.4e** and **6.4f**) zone axes. The HAADF-STEM images - sometimes referred to as Z-contrast images - also provide information about structural variations across the sample on an atomic level because the brightness of an atomic column of HAADF-STEM image is directly proportional to the square of the Z value in that column (Z represents the average atomic number of the atoms in the column). Therefore, the appearance of the regular alternative brighter and darker spots (each spot represents one atomic column) in **Figure 6.4c** and **6.4f** corresponds to Nb/Fe/Al/C/Vacancy atoms in different columns. When those results are put in conjunction with EDS results, it is reasonable to assume that elements in the brighter spots are mainly Nb, with some amount of Fe, since both have higher Z value than Al and C.

To further confirm that HAADF-STEM image correspond to M_6C phase (or η-carbide), QSTEM simulated HAADF-STEM was carried out for Nb_4Al_2C. This phase has a complex FCC structure containing 112 atoms in one unit cell, namely 96 metal (M) and 16 carbon (C) atoms. The M in M_6C has three nonequivalent Wyckoff sites, denoted 16d,

48f, and 32e, while C in M_6C denoted 16c. The crystal structures of a Nb_4Al_2C unit cell projected in (110) and (100) planes are shown in **Figure 6.5a** and **6.5c**, while corresponding QSTEM simulated HAADF-STEM and BF-STEM images of the Nb_4Al_2C structure viewed from low-index [110] and [100] zone axes is shown in **Figure 6.5b** and **6.5d.** It is clear from **Figure 6.5** that the interatomic distances viewed from [110] are more distinguishable compared to those of [100]. Therefore, a detailed comparison between the simulated HAADF-STEM and the experimental images of the Nb_4Al_2C structure has been presented in **Figure 6.6**. A unit cell is indicated in **Figure 6.6b** by the white dashed rectangle and the atomic arrangement in the unit cell is indicated in detail. It is manifest that the simulated structure is highly consistent with the experimental observation, indicating the preferential selection of the M (32e) site for Al in the Nb_4Al_2C structure. The ratio of (48f +16d)/32e is equal to 2, which is also consistent with the molar ratio of (Nb+Fe)/Al measured by EDS (~close to 2).

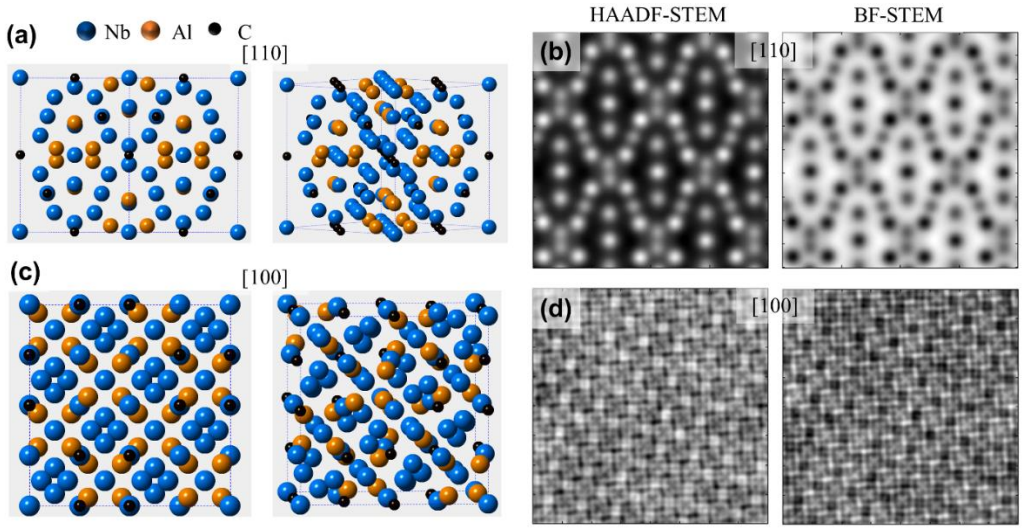

Figure 6-5(a) and (c): Nb_4Al_2C structure in (110) and (100) projection; (b) and (d): QSTEM simulated HAADF-STEM and BF-STEM images of the Nb_4Al_2C structure corresponding to structures (a) and (c).

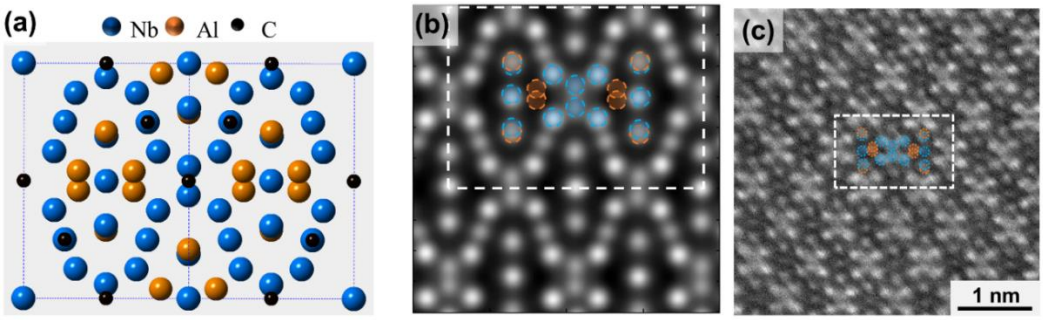

Figure 6-6 Comparison of the simulated and experimental HAADF-STEM images: (a) the 3D unit cell [110] projection of Nb_4Al_2C structure; (b): Simulated HAADF-STEM image corresponding to the structure shown in (a); (c): Experimental HAADF-STEM image of the $(Nb, Fe)_4Al_2C$ phase.

Results of SEM-EDS and STEM-EDS presented thus far clearly show that major phase that forms in sample S2 is η-carbide with $(Nb_{0.8},Fe_{0.2})_4Al_2C$ stoichiometry, and FCC crystal structure belonging to the space group of $Fd\bar{3}m$. The calculated XRD pattern of η-$(Nb_{0.8},Fe_{0.2})_4Al_2C$ generated by VESTA [142] and the experimental 2θ plus normalized intensity, including the hkl indices are displayed in **Figure 6.7**. All following XRD indexing of η-$(Nb_{0.8},Fe_{0.2})_4Al_2C$ is based on the values in this table. The lattice parameter determined by Rietveld refinement of XRD for sample S2 was found to be 11.660±0.001 Å and thus is close to the value of 11.78 Å obtained by HR-S/TEM .

Given the fact that when Nb, Fe, Al and C powders are mixed to reach targeted stoichiometry of $(Nb_{0.8},Fe_{0.2})_2AlC$, they reaction sinter and form newly discovered η-$(Nb_{0.8},Fe_{0.2})_4Al_2C$ and NbC, it is reasonable to assume that combination of those two phases is more thermodynamically stable, than hysterical $(Nb_{0.8},Fe_{0.2})_2AlC$ MAX phase solid solution. However, since sintering of phase-pure quaternary MAX phase solid solution sintering from all elemental powders high phase purity is challenging because many intermediate competing phases might form in those quaternary systems [143,144],

sample S3 with targeted stoichiometry same as that of S3, namely $(Nb_{0.8},Fe_{0.2})_2AlC$, has been reaction sintered starting from powder mixture of Nb_2AlC (from sample S1), Fe, Al and C.

(a)

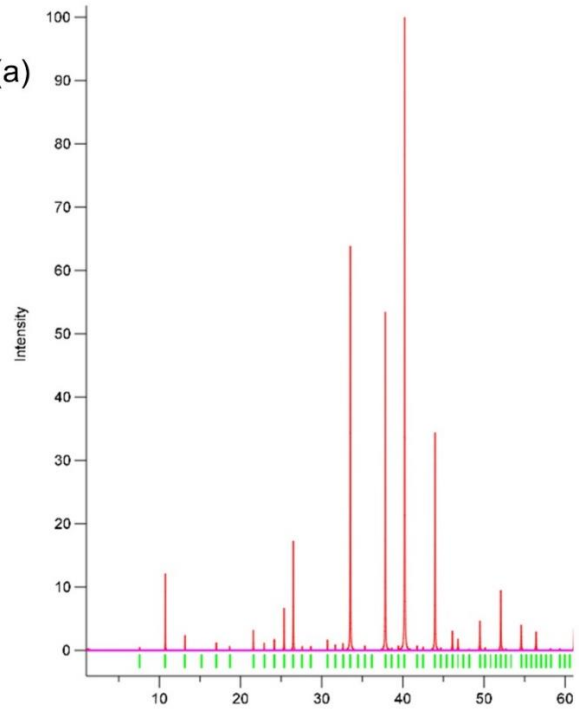

(b)

2θ	Normalized Intensity	hkl
13.16	5.58	111
21.58	5.79	220
26.50	52.86	222
30.70	6.79	400
33.53	70.90	331
37.83	65.92	224
38.64	0.68	500
39.44	0.54	431
40.22	100.00	333
41.76	1.04	432
42.50	0.52	215
43.97	93.38	440
46.79	2.55	442
49.48	7.15	260
52.08	15.11	226
56.41	4.68	711

Figure 6-7(a) The calculated XRD pattern of η-$(Nb_{0.8},Fe_{0.2})_4Al_2C$ phase based on the crystallography data from HR-STEM. (b) The experimental XRD information of η-$(Nb_{0.8},Fe_{0.2})_4Al_2C$. The peaks with negligible intensities are ignored.

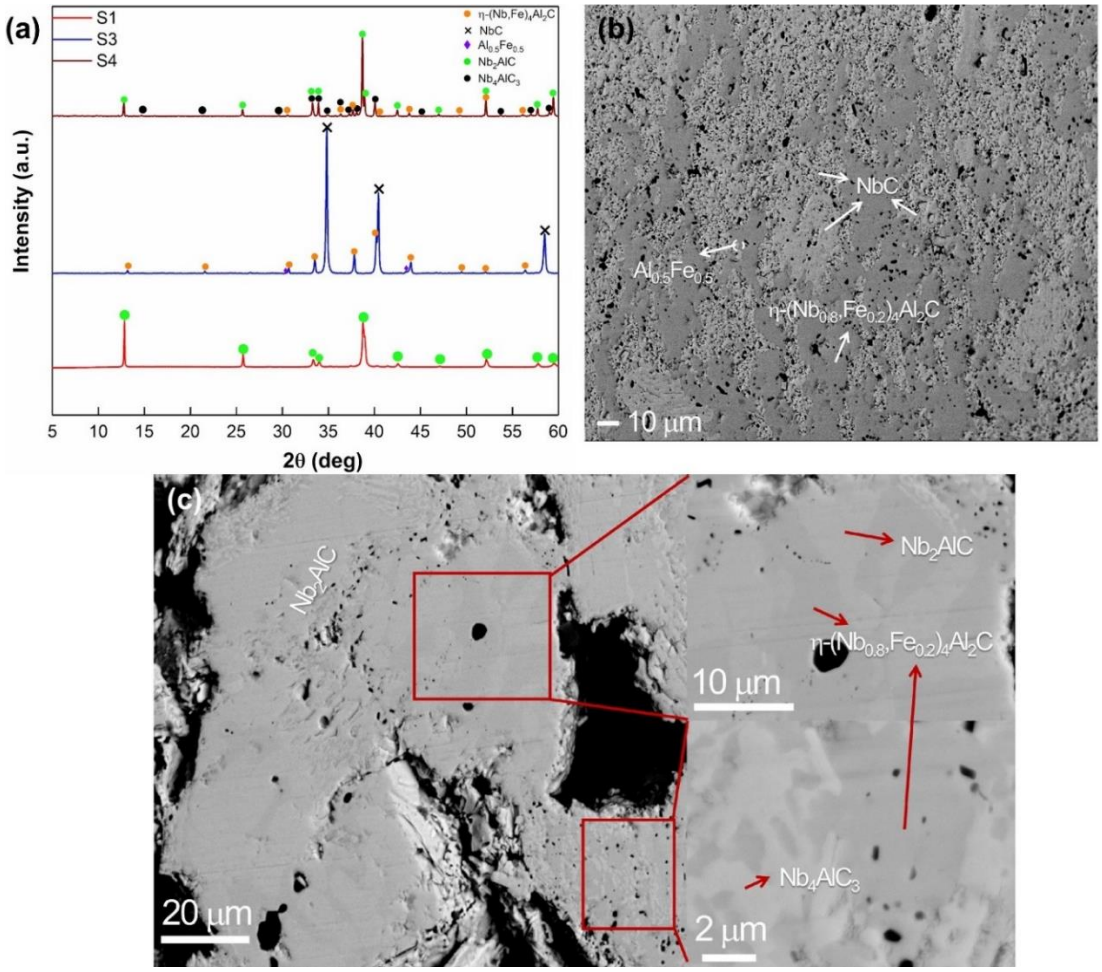

Figure 6-8 (a) The comparison between XRD patterns of S1, S3, and S4; (b) SEM image of S3, where η-$(Nb_{0.8},Fe_{0.2})_4Al_2C$, NbC, and $Al_{0.5}Fe_{0.5}$ were identified; (c) SEM images of S4, where η-$(Nb_{0.8},Fe_{0.2})_4Al_2C$, Nb_2AlC and Nb_4AlC_3 were identified using EDS. Areas under red squares are magnified and shown on the right. No Fe was detected by EDS neither in Nb_2AlC nor in Nb_4AlC_3.

The X-ray diffractogram of S3 (**Figure 6.8a**) as in the case of sample S1 also shows presence of η-$(Nb_{0.8},Fe_{0.2})_4Al_2C$ and NbC, and no presence of any MAX phase. However, unlike in the case of S1, $Al_{0.5}Fe_{0.5}$ intermetallic was also identified in XRD of sample S3. The presence of those phases was also confirmed in SEM and EDS (**Figure 6.8b**). This finding suggest that that addition of Fe to Nb_2AlC MAX phases causes its decomposition to NbC by Al diffusing out of the MAX phase and reacting with Fe to form

$Al_{0.5}Fe_{0.5}$ intermetallic. This intermetallic most mot likely further reacts with Al-depleted MAX phases or NbC to form more thermodynamically stable η-$(Nb_{0.8},Fe_{0.2})_4Al_2C$.

To further check if formation of η-$(Nb_{0.8},Fe_{0.2})_4Al_2C$ and NbC, rather than $(Nb_{0.8},Fe_{0.2})_2AlC$ MAX phase solid solutions in samples S2 and S3 is result of the limited solid solubility of Fe on Nb sublattice (i.e., less than 20%) in Nb_2AlC MAX phase, sample S4 has been reaction sintered with targeted stoichiometry of $(Nb_{0.97},Fe_{0.03})_2AlC$, using same sintering conditions as in the case of S2 and S3. As can be seen from XRD results in **Figure 6.6a**, η-$(Nb_{0.8},Fe_{0.2})_4Al_2C$ is present in the reaction sinter samples, but in smaller amount, besides the parent Nb_2AlC phase and a high n-order MAX phase Nb_4AlC_3. SEM images (back-scattered mode) of S4 in **Figure 6.6c** together with EDS analysis, also confirmed presence of those three phases after sintering. Noted here that no Fe was detected by EDS neither in Nb_2AlC nor in Nb_4AlC_3, suggesting complete insolubility of Fe in both Nb-based MAX phases. The formation of Nb_4AlC_3 in this case, further confirms our previous findings that addition of Fe promotes decomposition of Nb_2AlC due to Fe affinity to Al [145], causing it diffusion from Nb_2AlC. However, unlike in the case of sample S3, this decomposition of Nb_2AlC in S4 was incomplete and resulted in formation of Nb_4AlC_3, due to smaller Fe content . Decomposition of 211 MAX phases to 413 ones due to diffusion of Al from the MAX phases has been reported in other Al-based MAX phases, such as Ta_2AlC and V_2AlC [32,93]. Last but not least, it is reasonable to assume that further reaction of decomposed MAX phase formed FeAl intermetallic leads to the formation of η-$(Nb_{0.8},Fe_{0.2})_4Al_2C$ as the most thermodynamically stable in the Nb-Fe-Al-C system, even with a small amount of Fe (3 at.%).

As the results discussed thus far showed the favorable formation of η-$(Nb_{0.8},Fe_{0.2})_4Al_2C$ in Nb-Fe-Al-C system, the study was extended to synthesize predominantly single-phase η-$(Nb_{0.8},Fe_{0.2})_4Al_2C$ using a starting powder mixture with targeted 421 stoichiometry (sample S5). XRD, SEM, and EDS point analysis in **Figure 6.9** confirmed presence of primarily η-$(Nb_{0.8},Fe_{0.2})_4Al_2C$ phase with a small amount of NbC, Nb_2C and Nb_2Al secondary phases . The peak intensity of NbC was not noticeable as it represents in S2 (**Figure 6.1**) and S4 (**Figure 6.8a**).

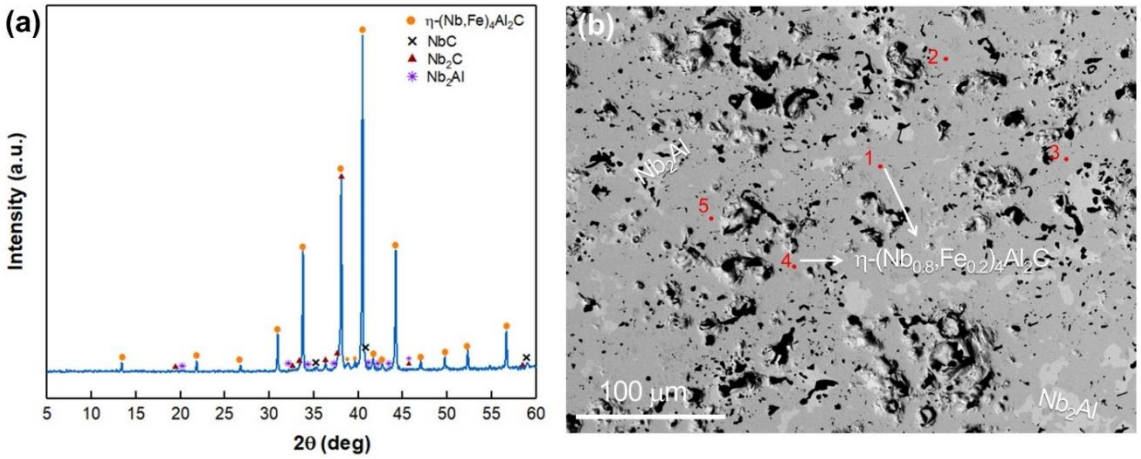

(c)

	1	2	3	4	5	Avg. ± Std. dev.
C	47.82	48.86	47.80	47.81	49.57	48.37±0.72
Al	16.95	16.76	17.16	16.95	16.44	16.85±0.24
Fe	7.56	7.40	7.53	7.59	7.30	7.48±0.11
Nb	27.67	26.98	27.51	27.64	26.70	27.30±0.39
Fe/(Nb+Fe)	21.46%	21.52%	21.49%	21.54%	21.47%	21.50%±0.03%
(Nb+Fe)/Al	2.08	2.05	2.04	2.08	2.07	2.06±0.01

Figure 6-9 (a) XRD pattern of sample S5; (b) SEM image of sample S5, where η-$(Nb_{0.8},Fe_{0.2})_4Al_2C$ and Nb_2Al were identified using EDS;(c) EDS point analysis of η-$(Nb_{0.8},Fe_{0.2})_4Al_2C$ phase.

Since Ni and Co are also iron-group elements, the study was extended to investigate if the η-carbide with 421-stoichiometry forms when 20% Ni or Co is added into Nb-Al-C system. As can be seen in **Figure 6.10 and Table 6-4**, SEM results with

EDS for sample S6 with targeted composition of $(Nb_{0.8},Ni_{0.2})_4Al_2C$, also confirms formation of $(Nb_{0.8},Ni_{0.2})_4Al_2C$. The dense η-carbide was enveloped with porous NbC, similar as in the case of sample S2 (**Figure 6.2a**). From the corresponding EDS mapping, distinction between $(Nb_{0.8},Ni_{0.2})_4Al_2C$ regions which have uniform Ni and Al distribution, NbC regions is clear. EDS point analysis on the dark grey areas in **Figure 6.10a** is listed in **Table 4** shows (Nb+Ni)/Al ratio close to 2, and Ni/(Ni+Nb) ratio close to 0.2 as expected for 421 η-carbide with the chemical formula of $(Nb_{0.8},Ni_{0.2})_4Al_2C$.

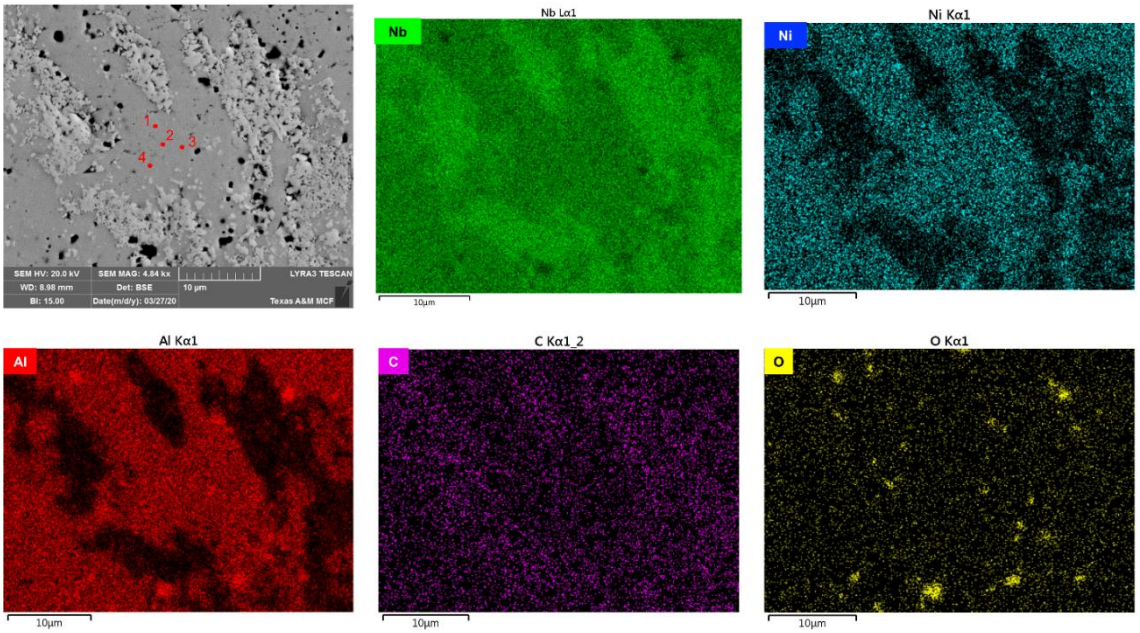

Figure 6-10 Low magnification of SEM image and EDS mapping of sample S6. 4 points were placed on $(Nb_{0.8},Ni_{0.2})_4Al_2C$ (dark grey region) to do EDS point analysis.

Table 6-4 EDS point analysis for sample S6 from Figure 6.10a.

	1	2	3	4	Avg. ± Std. dev.
C, at.%	40.50	40.61	40.43	42.05	40.90±0.67
Al, at.%	19.33	19.05	19.44	18.57	19.10±0.34
Ni, at.%	8.18	8.03	8.10	8.03	8.09±0.62
Nb, at.%	32.00	32.31	32.03	31.35	31.92±0.35
Ni/(Nb+Ni)	20.36%	19.91%	20.18%	20.39%	20.21%±0.19%
(Nb+Ni)/Al	2.08	2.12	2.06	2.12	2.10±0.02

The similar has been observed in the system with targeted composition of $(Nb_{0.8},Co_{0.2})_4Al_2C$, i.e., in sample S7. A dense light gray region in SEM images was surrounded by lighter gray porous phase that was identified as NbC based on EDS analysis (**Figure 6.11a** and **6.11b**). EDS analysis of the light gray phase (**Figure 6.11c**) shows (Nb+Co)/Al ratio of 2.18, and Co/(Co+Nb) ratio of 0.21, which is close to those expected for η- $(Nb_{0.8},Co_{0.2})_4Al_2C$.

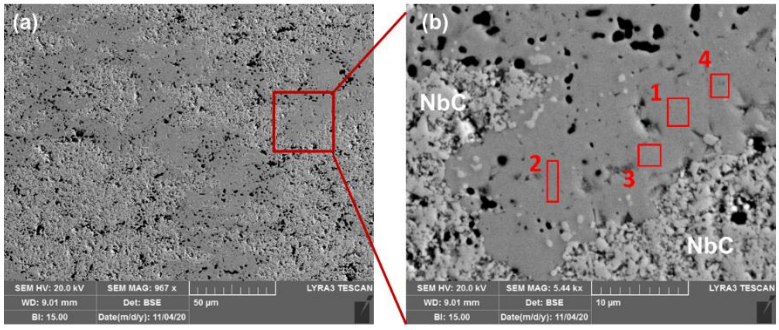

(c)

	1	2	3	4	Avg. ± Std. dev.
C	40.02	38.07	41.71	40.77	40.14±1.34
Al	18.29	18.94	19.07	19.10	18.85±0.33
Co	9.31	9.17	7.87	7.84	8.55±0.69
Nb	32.39	33.82	31.35	32.29	32.46±0.88
Co/(Nb+Ni)	22.33%	21.33%	20.07%	19.54%	20.81%±1.09%
(Nb+Co)/Al	2.28	2.27	2.06	2.10	2.18±0.10

Figure 6-11 (a) Low magnification and (b) high magnification SEM images of sample S7. The phase with a porous morphology is identified as NbC using EDS. (c) is the corresponding EDS point analysis dark gray regions marked with red boxes on (b).

6.4. Summary

In summary, the study of the phase stability Fe-Nb-Al-C, Ni-Nb-Al-C and Nb-Co-Al-C systems showed no formation of any quaternary carbide with MAX phase structure. Instead, new η-carbides with $(Nb_{0.8},Fe_{0.2})_4Al_2C$, $(Nb_{0.8},Ni_{0.2})_4Al_2C$, and $(Nb_{0.8},Co_{0.2})_4Al_2C$ are discovered to form and a most thermodynamically stable phase.

This, as well as fact that no MAX phase was present in those systems having Nb/(Nb+Fe) ratio equal to 0.2 as well as that detected MAX phase in the system having Nb/(Nb+Fe) ratio equal to 0.03 contains no Fe, suggests that solubility limit of Fe, and to the further extent Ni and Co in Nb2AlC is below any detectable value. This newly discovered η-carbides were found to crystalize in f.c.c structure having $Fd\bar{3}m$ space group.

7. CONCLUSIONS AND FUTURE WORK

This study focuses on synthesis and characterization of newly discovered V- and Nb-based MAX phase solid solutions. The resultant ameliorated properties of those solid solutions were analyzed as well, and key findings are summarized below.

In section 2, we report on phase pure Nb_2AlC that was synthesized for the first time from the Nb, Al and C elemental powder. Powder mixture with molar ratio Nb:Al:C=2:1.15:0.95 sintered using the PECS technique at 1600^{o}C for 30 min with a heating rate of 25^{o}C/min was corroborated to give Nb_2AlC with highest phase purity (>91 wt.%). Decreasing the excess amount of Al in the starting materials results in the formation of another MAX phase Nb_4AlC_3 while increasing the amount of excessive Al beyond the value used in the optimized recipe triggers the formation of profuse niobium-carbide and niobium-aluminides. Due to the applied pressure during the sintering, these niobium-aluminides were pushed toward edges of the sample and left a few Al-deficient areas, which in turn results in the formation of Nb_4AlC_3 once again. Moreover, increasing the sintering temperature to 1650^{o}C induced Nb_2AlC to decompose into Nb_4AlC_3 and another not commonly reported niobium-carbide, namely Nb_3Al_2C. The actual atomic percentages of Nb, Al, and C in Nb_2AlC is 52.29±0.52, 26.08±0.22, and 21.63±0.75, respectively, determined by WDS. HR-STEM confirmed the atomic structure of Nb_2AlC with two M-layers interleaved by an A-layer. The obtained Vickers hardness of as-prepared Nb_2AlC was 4.2 GPa and the bulk, shear, and Young's modulus are 184, 116, and 287 GPa, respectively. The method of synthesizing highly pure Nb_2AlC using the PECS technique can not only shed light on synthesizing other MAX phases using the same technique but

also promote the yield of related 2D materials (MXene) from the parent-materials-purity standpoint.

The results presented in Section 3 show that predominant single-phase $(Ti_xNb_{1-x})_2AlC$ over full composition range from x=0 to x=1 can be also reaction synthesized from the mixture of elemental powders by PECS. However, for each composition, processing parameters had to be adjusted to achieve high phase purity. A higher percentage of Nb within the green body, a higher sintering temperature is needed until the Nb% reaches 50% where all desired samples were prepared under 1600°C. The decreasing trend of lattice parameters *a* and *c* with an increasing percentage of Ti was obtained by Rietveld refinement of XRD results. That trend is in agreement with Vegard's law, which is also represented by Vickers hardness, Young's, and shear moduli. Besides target $(Ti_xNb_{1-x})_2AlC$ solid solution, other tiny amounts of impurities, i.e., niobium aluminum in different stoichiometries, niobium carbides, and titanium carbides were also discovered. EDS analysis confirmed the samples' 211-stoichiometry with Ti and Nb homogeneously arranged on the M-site. Unfortunately, no solid solution strengthening effect was observed while the compressive strength of Nb_2AlC was reported as 1.6 GPa for the first time, which is one of the highest ever reported values for any other MAX phases.

V_3AlC_2 MAX phase has been theoretically predicted but have not been experimentally synthesized to date due to the system being thermodynamically unstable at room temperature when compared to competitive phases. In Section 4, Ti is proposed as an alloying element to stabilize the V_3AlC_2 system and synthesize $(V_x,Ti_{1-x})_3AlC_2$ with x ranging from 0 to 0.9. $(V_x,Ti_{1-x})_3AlC_2$ with x=0-0.9 was reaction synthesized from the

elemental powder mixtures using PECS technique. The phase compounds and microstructure were analyzed by XRD, SEM, and EDS. It was found that $(V_x,Ti_{1-x})_3AlC_2$ was no more thermodynamically stable for x is greater than 0.9 due to decomposition into $(V_x,Ti_{1-x})_2AlC$ and $(V_x,Ti_{1-x})_4AlC_3$, which results from the outward diffusion of Al.

In Section 5, highly pure $(V_{1-x}Fe_x)_2AlC$ and V_2AlC were both synthesized using the PECS technique. The maximum solubility of Fe on the M-site of V_2AlC was found to me up to 3 at.%. Beyond the maximum solubility, the $(V_{1-x}Fe_x)_2AlC$ tended to be less thermodynamically stable as more secondary phases (AlFe and V_4AlC_3) forms. The reduced stability was validated both experimentally and computationally. Replacing V with Fe on M-sublattice of V_2AlC induces the decrease of PM-strength instead of enhancing it, which can be ascribed to the small AFM moments introduced by Fe substitution, resulting in the competition with PM-state of V_2AlC. The possibility of substituting the original M-site atoms with magnetic elements in the V_2AlC phase offers another great potential of fabricating magnetic MXene for further application-oriented studies.

The same idea of alloying MAX phase with Fe was applied to Nb-Al-C system, and even extended to alloying with Ni and Co. In Section 6, the phase stability of dissolving Fe into Nb-Al-C system or alloyed with Nb_2AlC was investigated. Although no quaternary carbide with MAX phase structure was detected in Nb-Fe-Al-C, the formation of a new η-carbide, η-$(Nb_{0.8},Fe_{0.2})_4Al_2C$ was found. This new phase crystalizes in f.c.c structure with the space group of $Fd\bar{3}m$.It turns out η-$(Nb_{0.8},Fe_{0.2})_4Al_2C$ is more thermodynamically stable than Nb_2AlC in Nb-Fe-Al-C system due to the fact that a small

amount of Fe added into the system will result in the decomposition of Nb_2AlC into η-$(Nb_{0.8},Fe_{0.2})_4Al_2C$ and high n-order MAX phase Nb_4AlC_3. Currently η-$(Nb_{0.8},Fe_{0.2})_4Al_2C$ cannot be synthesized as the predominant phase, the future works on optimizing sintering conditions and on obtaining physical and mechanical properties of this η-carbide are desired.

The results and discussions presented in this dissertation answered and solved essential questions that are required to better understand MAX phase solid solution's synthesis and tuned properties. To further increase the understanding of these new materials and/or expand the members of MAX phase family, the following questions should be investigated in the near future:

1. ***What is the effect of excessive Al on the final composition of other members of MAX phases, i.e., Hf_2AlC and Zr_2AlC?*** Our work elucidates the amount of Al in the starting powder mixture plays an essential role in determining final sample's purity. It would be efficiently useful to apply the same approach to synthesize other MAX phases, especially those members that are less studied, for example, Hf_2AlC and Zr_2AlC, but hold a lot of potential for different applications.
2. ***What is the trend of $(Ti_xNb_{1-x})_2AlC$ properties over the full composition?*** In our work, the change of elastic moduli, hardness, and compressive strength of $(Nb_xTi_{1-x})_2AlC$ over the full composition has been studied. However, as the good candidate for high temperature applications, it is essential to study how $(Nb_xTi_{1-x})_2AlC$'s thermal and mechanical properties over the full compositional range. In addition,

the study on oxidation resistance of $(Nb_xTi_{1-x})_2AlC$ under high temperature is needed.

3. ***What is the magnetic response of newly synthesized η-carbide $(Nb_{0.8}Fe_{0.2})_4Al_2C$, $(Nb_{0.8}Ni_{0.2})_4Al_2C$, and $(Nb_{0.8}Co_{0.2})_4Al_2C$?*** With the addition of Fe/Co/Ni, the newly synthesized quaternary carbide should display a different magnetic response comparing to that of ternary Nb_2AlC. However, to conduct the precise magnetic measurement, the specimen is required to be consisted of predominant single-phase, which means extra modifications on current sintering parameters are needed.
4. ***Can synthesis methods developed herein can be extended to synthesize multy-component MAX phases, i.e., medium or high entropy MAX pleases?*** Inspired by the concept of high-entropy (HE) material, which is to stabilize approximately equimolar mixtures to obtain a sturdier systems by maximizing the configurational entropy, it is reasonable to expect that HE-MAX phase --- defined as the MAX phase has equal to (medium-entropy, ME) or more than (HE) 3 elements alloyed on M, A, and X sites --- will possess unique chemical and physical properties, tailorable for even broader range of applications. The concepts of synthesizing MAX phase solid solutions with two elements on M site thus should be further expanded and explored for synthesis of HE-MAX phases. Moving further in that direction, we have already showed that my mixing Ti_2AlC, V_2AlC, and Nb_2AlC already powders site synthesized as a part of this thesis research, in the equimolar

ratio and their further reaction synthesis, can lead to formation of HE ($(Ti_{0.33}V_{0.33}Nb_{0.33})_2AlC$ MAX phase, **Figure 7.1**.

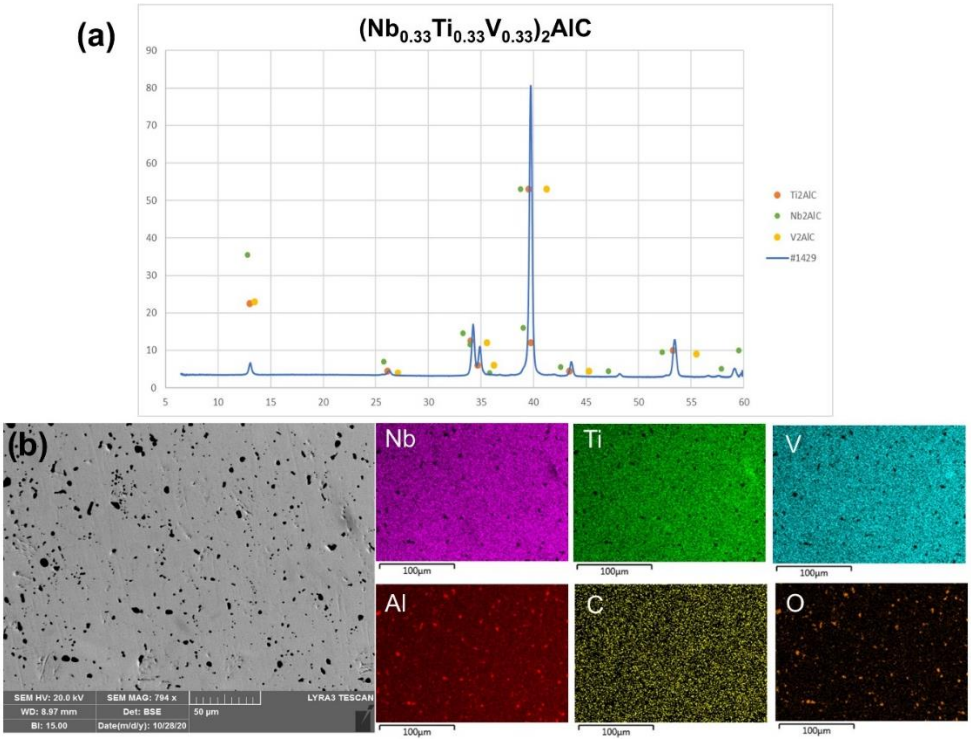

Figure 7-1 (a) XRD of $(Nb_{0.33}Ti_{0.33}V_{0.33})_2AlC$ and (b) SEM of HE-MAX area with corresponding EDS mapping images. The black spots were alumina corroborated by the EDS mapping results.

REFERENCES

[1] H.J. Rathod, T. Ouisse, M. Radovic, A. Srivastava, Room temperature crack-healing in an atomically layered ternary carbide, Science Advances. 7 (2021) : eabg 2549.

[2] M. Radovic, M.W. Barsoum, MAX phases: bridging the gap between metals and ceramics, American Ceramics Society Bulletin. 92 (2013) 20–27.

[3] M.W. Barsoum, M. Radovic, Elastic and Mechanical Properties of the MAX Phases, Annual Review of Materials Research. 41 (2011) 195–227.

[4] M. Radovic, M.W.W. Barsoum, A. Ganguly, T. Zhen, P. Finkel, S.R.R. Kalidindi, E. Lara-Curzio, On the elastic properties and mechanical damping of Ti_3SiC_2, Ti_3GeC_2, $Ti_3Si_{0.5}Al_{0.5}C_2$ and Ti_2AlC in the 300-1573 K temperature range, Acta Materialia. 54 (2006) 2757–2767.

[5] M.W. Barsoum, MAX Phases: Properties of Machinable Ternary Carbides and Nitrides, John Wiley & Sons, 2013.

[6] L. Zheng, J. Wang, X. Lu, F. Li, J. Wang, Y. Zhouw, $(Ti_{0.5}Nb_{0.5})_5AlC_4$: A New-Layered Compound Belonging to MAX Phases, Journal of the American Ceramic Society. 93 (2010) 3068–3071.

[7] W. Yu, M. Vallet, B. Levraut, V. Gauthier-Brunet, S. Dubois, Oxidation mechanisms in bulk Ti_2AlC: Influence of the grain size, Journal of the European Ceramic Society. 40 (2020) 1820–1828.

[8] M. Sokol, V. Natu, S. Kota, M.W. Barsoum, On the Chemical Diversity of the MAX Phases, Trends in Chemistry. 1 (2019) 1–14.

[9] S. Sridharan, H. Nowotny, STUDIES IN THE TERNARY SYSTEM Ti-Ta-Al AND IN THE QUATERNARY SYSTEM Ti-Ta-Al-C., Zeitschrift Fuer Metallkunde/Materials Research and Advanced Techniques. 74 (1983) 468–472.

[10] C. Hu, Q. Huang, Y. Bao, Y. Zhou, Sintering and Properties of Nb_4AlC_3 Ceramic, In Sintering of Ceramics-New Emerging Techniques. IntechOpen (2012) 141–158.

[11] C. Hu, F. Li, J. Zhang, J. Wang, J. Wang, Y. Zhou, Nb_4AlC_3: A new compound belonging to the MAX phases, Scripta Materialia. 57 (2007) 893–896.

[12] C.M. Hamm, T. Schäfer, H. Zhang, C.S. Birkel, Non-conventional Synthesis of the 413 MAX Phase V_4AlC_3, Zeitschrift Für Anorganische Und Allgemeine Chemie. 642 (2016) 1397–1401.

[13] Y. Zhou, F. Meng, J. Zhang, New MAX-Phase Compounds in the V–Cr–Al–C System, Journal of the American Ceramic Society. 91 (2008) 1357–1360.

[14] Z.J. Lin, M.S. Li, J.Y. Wang, Y.C. Zhou, High-temperature oxidation and hot corrosion of Cr_2AlC, Acta Materialia. 55 (2007) 6182–6191.

[15] D.W. Clark, S.J. Zinkle, M.K. Patel, C.M. Parish, High temperature ion irradiation effects in MAX phase ceramics, Acta Materialia. 105 (2016) 130–146.

[16] L. Hu, R. Benitez, S. Basu, I. Karaman, M. Radovic, Processing and characterization of porous Ti_2AlC with controlled porosity and pore size, Acta Materialia. 60 (2012) 6266–6277.

[17] R. Benitez, H. Gao, M. O'Neal, P. Lovelace, G. Proust, M. Radovic, Effects of microstructure on the mechanical properties of Ti_2AlC in compression, Acta Materialia. 143 (2018) 130–140.

[18] A. Mockute, P.O.Å. Persson, F. Magnus, A.S. Ingason, S. Olafsson, L. Hultman, J. Rosen, Synthesis and characterization of arc deposited magnetic $(Cr,Mn)_2AlC$ MAX phase films, Rapid Research Letters. 8 (2014) 420–423.

[19] P. Gudlur, A. Boczek, M. Radovic, A. Muliana, On characterizing the mechanical properties of aluminum-alumina composites, Materials Science and Engineering A. 590 (2014) 352–359.

[20] B. Manoun, S.K. Saxena, G. Hug, A. Ganguly, E.N. Hoffman, M.W. Barsoum, Synthesis and compressibility of $Ti_3(Al,Sn_{0.2})C_2$ and $Ti_3Al(C_{0.5},N_{0.5})_2$, Journal of Applied Physics. 101 (2007) 113523.

[21] A. Donchev, M. Schütze, E. Ström, M. Galetz, Oxidation behaviour of the MAX-phases Ti_2AlC and $(Ti,Nb)_2AlC$ at elevated temperatures with and without fluorine treatment, Journal of the European Ceramic Society. 39 (2019) 4595–4601.

[22] M.W. Barsoum, I. Salama, T. El-Raghy, J. Golczewski, H.J. Seifert, F. Aldinger, W.D. Porter, H. Wang, Thermal and electrical properties of Nb_2AlC, $(Ti,Nb)_2AlC$ and Ti_2AlC, Metallurgical and Materials Transactions A. 33 (2002) 2775–2779.

[23] B. Manoun, F. Zhang, S.K. Saxena, S. Gupta, M.W. Barsoum, On the compression behaviour of $(Ti_{0.5},V_{0.5})_2AlC$ and $(Ti_{0.5},Nb_{0.5})_2AlC$ to quasi-hydrostatic pressures above 50 GPa, Journal of Physics: Condensed Matter. 19 (2007) 246215.

[24] M. Naguib, G.W. Bentzel, J. Shah, J. Halim, E.N. Caspi, J. Lu, L. Hultman, M.W. Barsoum, New Solid Solution MAX phases: $(Ti_{0.5},V_{0.5})_3AlC_2$, $(Nb_{0.5},V_{0.5})_2AlC$, $(Nb_{0.5},V_{0.5})_4AlC_3$ and $(Nb_{0.8},Zr_{0.2})2$, Materials Research Letters. 2 (2014) 233–240.

[25] N. Sc, A. Max, M.W. Barsoum, J. Rosen, Synthesis of Two-Dimensional $Nb_{1.33}C$

(MXene) with Randomly Distributed Vacancies by Etching of the Quaternary Solid Solution $(Nb_{2/3}Sc_{1/3})_2AlC$ MAX Phase, ACS Applied Nano Materials. 1 (2018) 2455–2460.

[26] P. Cai, Q. He, L. Yang, Z. Huang, X. Liu, J. Yin, Y. Huang, Mechanical and thermal properties and microstructural evolution of Ta-doped Nb_4AlC_3, Ceramics International. 45 (2019) 9799–9806.

[27] M. Griseri, B. Tunca, S. Huang, M. Dahlqvist, J. Rosén, J. Lu, P.O.Å. Persson, L. Popescu, J. Vleugels, K. Lambrinou, Ta-based 413 and 211 MAX phase solid solutions with Hf and Nb, Journal of the European Ceramic Society. 40 (2020) 1829–1838.

[28] J. Yang, M. Naguib, M. Ghidiu, L.-M. Pan, J. Gu, J. Nanda, J. Halim, Y. Gogotsi, M.W. Barsoum, Two-Dimensional Nb-Based M_4C_3 Solid Solutions (MXenes), Journal of the American Ceramic Society. 99 (2016) 660–666.

[29] T. Lapauw, D. Tytko, K. Vanmeensel, S. Huang, P.-P. Choi, D. Raabe, E.N. Caspi, O. Ozeri, M. to Baben, J.M. Schneider, K. Lambrinou, J. Vleugels, $(Nb_x, Zr_{1-x})_4AlC_3$ MAX Phase Solid Solutions: Processing, Mechanical Properties, and Density Functional Theory Calculations, Inorganic Chemistry. 55 (2016) 5445–5452.

[30] S. Gupta, M.W. Barsoum, Synthesis and Oxidation of V2AlC and (Ti0.5,V0.5)2AlC in Air, Journal of The Electrochemical Society. 151 (2004) 24–29.

[31] J. Etzkorn, V_2AlC, V_4AlC_{3-x} ($x \approx 0.31$), and $V_{12}Al_3C_8$: Synthesis, Crystal Growth,

Structure, and Superstructure, Inorganic Chemistry. 46 (2007) 7646–7653.

[32] C. Hu, L. He, M. Liu, X. Wang, J. Wang, M. Li, Y. Bao, Y. Zhou, In Situ Reaction Synthesis and Mechanical Properties of V_2AlC, Journal of the American Ceramic Society. 91 (2008) 4029–4035.

[33] B. Wang, A. Zhou, Q. Hu, L. Wang, Synthesis and oxidation resistance of V_2AlC powders by molten salt method, International Journal of Applied Ceramic Technology. 14 (2017) 873–879.

[34] C.L. Yeh, W.J. Yang, Formation of MAX solid solutions $(Ti,V)_2AlC$ and $(Cr,V)_2AlC$ with Al_2O_3 addition by SHS involving aluminothermic reduction, Ceramics International. 39 (2013) 7537–7544.

[35] W.B. Tian, Z.M. Sun, H. Hashimoto, Y.L. Du, Synthesis, microstructure and properties of $(Cr_{1-x}V_x)_2AlC$ solid solutions, Journal of Alloys and Compounds. 484 (2009) 130–133.

[36] J.C. Schuster, H. Nowotny, C. Vaccaro, The ternary systems: CrAlC, VAlC, and TiAlC and the behavior of H-phases (M_2AlC), Journal of Solid State Chemistry. 32 (1980) 213–219.

[37] E.N. Caspi, P. Chartier, F. Porcher, F. Damay, T. Cabioc'h, Ordering of (Cr,V) Layers in Nanolamellar $(Cr_{0.5}V_{0.5})_{n+1}AlC_n$ Compounds, Materials Research Letters. 3 (2015) 100–106.

[38] C.M. Hamm, M. Dürrschnabel, L. Molina-Luna, R. Salikhov, D. Spoddig, M. Farle, U. Wiedwald, C.S. Birkel, Structural, magnetic and electrical transport properties of non-conventionally prepared MAX phases V_2AlC and $(V/Mn)_2AlC$, Submitted.

2 (2018) 483–490.

[39] Jimmy Thörnberg, Joseph Halim, Jun Lu, Rahele Meshkian, Justinas Palisaitis, Lars Hultman, P. O.Å. Persson, Johanna Rosen, Synthesis of $(V_{2/3}Sc_{1/3})_2AlC$ i-MAX phase and $V_{2-x}C$ MXene scrolls, Nanoscale. 11 (2019) 14720–14726.

[40] M. Dahlqvist, J. Lu, R. Meshkian, Q. Tao, L. Hultman, J. Rosen, Prediction and synthesis of a family of atomic laminate phases with Kagomé-like and in-plane chemical ordering, Science Advances. 3 (2017) 1–10.

[41] G. Deysher, C.E. Shuck, K. Hantanasirisakul, N.C. Frey, A.C. Foucher, K. Maleski, A. Sarycheva, V.B. Shenoy, E.A. Stach, B. Anasori, Y. Gogotsi, Synthesis of Mo_4VAlC_4 MAX Phase and Two-Dimensional Mo_4VC_4 MXene with Five Atomic Layers of Transition Metals, ACS Nano. 14 (2019) 204–217.

[42] Z.-Y. Jiao, S.-H. Ma, Y.-L. Guo, Theoretical study of mechanical, thermal and optical properties of $(Ti_{1-x}Nb_x)_3AlC_2$ solid solutions, The European Physical Journal B 2018 91:6. 91 (2018) 1–9.

[43] N. Li, Y. Mo, W.Y. Ching, The bonding, charge distribution, spin ordering, optical, and elastic properties of four MAX phases Cr_2AX (A = Al or Ge, X = C or N): From density functional theory study, Journal of Applied Physics. 114 (2013) 0–8.

[44] W. Luo, R. Ahuja, Magnetic $Fe_{n+1}AC_n$ (n = 1, 2, 3, and A = Al, Si, Ge) phases: from ab initio theory, Journal of Physics: Condensed Matter. 20 (2008) 064217.

[45] A. Mockute, M. Dahlqvist, J. Emmerlich, L. Hultman, J.M. Schneider, P.O.Å. Persson, J. Rosen, Synthesis and ab initio calculations of nanolaminated $(Cr,Mn)_2AlC$ compounds, Physical Review B. 87 (2013) 094113.

[46] A. Mockute, J. Lu, E.J. Moon, M. Yan, B. Anasori, S.J. May, M.W. Barsoum, J. Rosen, Solid Solubility and Magnetism upon Mn Incorporation in the Bulk Ternary Carbides Cr_2AlC and Cr_2GaC, Materials Research Letters. 3 (2015) 16–22.

[47] A.S. Ingason, M. Dahlqvist, J. Rosen, Magnetic MAX phases from theory and experiments; a review, J Phys Condens Matter. 28 (2016) 433003.

[48] S. Lin, P. Tong, B.S. Wang, Y.N. Huang, W.J. Lu, D.F. Shao, B.C. Zhao, W.H. Song, Y.P. Sun, Magnetic and electrical/thermal transport properties of Mn-doped $M_{n+1}AX_n$ phase compounds $Cr_{2-x}Mn_xGaC$ ($0 \leq x \leq 1$), Journal of Applied Physics. 113 (2013) 053502.

[49] A.S. Ingason, A. Petruhins, M. Dahlqvist, F. Magnus, A. Mockute, B. Alling, L. Hultman, I.A. Abrikosov, P.O.Å.Å. Persson, J. Rosen, A nanolaminated magnetic phase: Mn_2GaC, Materials Research Letters. 2 (2014) 89–93.

[50] M. Dahlqvist, A.S. Ingason, B. Alling, F. Magnus, A. Thore, A. Petruhins, A. Mockute, U.B. Arnalds, M. Sahlberg, B. Hjörvarsson, I.A. Abrikosov, J. Rosen, Magnetically driven anisotropic structural changes in the atomic laminate Mn_2GaC, Physical Review B. 93 (2016) 014410.

[51] A.S. Ingason, G.K. Pálsson, M. Dahlqvist, J. Rosen, Long-range antiferromagnetic order in epitaxial Mn_2GaC thin films from neutron reflectometry, Physical Review B. 94 (2016) 4–7.

[52] R. Meshkian, A.S. Ingason, U.B. Arnalds, F. Magnus, J. Lu, J. Rosen, A magnetic atomic laminate from thin film synthesis: $(Mo_{0.5}Mn_{0.5})_2GaC$, APL Materials. 3 (2015) 076102.

[53] Q. Tao, R. Salikhov, A. Mockute, J. Lu, M. Farle, U. Wiedwald, J. Rosen, Thin film synthesis and characterization of a chemically ordered magnetic nanolaminate $(V,Mn)_3GaC_2$, APL Materials. 4 (2016) 086109.

[54] Y. Li, J. Lu, M. Li, K. Chang, X. Zha, Y. Zhang, K. Chen, P.O.Å. Persson, L. Hultman, P. Eklund, S. Du, J.S. Francisco, Z. Chai, Z. Huang, Q. Huang, Multielemental single–atom-thick A layers in nanolaminated V_2(Sn, A)C(A = Fe, Co, Ni, Mn) for tailoring magnetic properties, Proceedings of the National Academy of Sciences of the United States of America. 117 (2020) 820–825.

[55] A. Talapatra, T. Duong, W. Son, H. Gao, M. Radovic, R. Arróyave, High-throughput combinatorial study of the effect of M site alloying on the solid solution behavior of M_2AlC MAX phases, Physical Review B. 94 (2016) 104106.

[56] K. Chen, Y. Chen, J. Zhang, Y. Song, X. Zhou, M. Li, X. Fan, J. Zhou, Q. Huang, Medium-entropy (Ti, Zr, Hf)$_2$SC MAX phase, Ceramics International. 47 (2021) 7582–7587.

[57] S.K. Nemani, B. Zhang, B.C. Wyatt, Z.D. Hood, S. Manna, R. Khaledialidusti, W. Hong, M.G. Sternberg, S.K.R.S. Sankaranarayanan, B. Anasori, High-Entropy 2D Carbide MXenes: $TiVNbMoC_3$ and $TiVCrMoC_3$, ACS Nano. 01 (2021) 44.

[58] M.W. Barsoum, The $M_{N+1}AX_N$ Phases: A New Class of Solids; Thermodynamically Stable Nanolaminates, Progress in Solid State Chemistry. 28 (2000) 201–281.

[59] M.W. Barsoum, The MAX Phases: Unique New Carbide and Nitride Materials, American Scientist. 89 (2013) 334–343.

[60] S. Li, G. Song, K. Kwakernaak, S. van der Zwaag, W.G. Sloof, Multiple crack healing of a Ti_2AlC ceramic, Journal of the European Ceramic Society. 32 (2012) 1813–1820.

[61] R. Benitez, W.H. Kan, H. Gao, M. O'Neal, G. Proust, M. Radovic, Room temperature stress-strain hysteresis in Ti_2AlC revisited, Acta Materialia. 105 (2016) 294–305.

[62] M.W. Barsoum, T. Zhen, S.R. Kalidindi, M. Radovic, A. Murugaiah, Fully reversible, dislocation-based compressive deformation of Ti_3SiC_2 to 1 GPa, Nature Materials. 2 (2003) 107–111.

[63] E.N. Hoffman, D.W. Vinson, R.L. Sindelar, D.J. Tallman, G. Kohse, M.W. Barsoum, MAX phase carbides and nitrides: Properties for future nuclear power plant in-core applications and neutron transmutation analysis, Nuclear Engineering and Design. 244 (2012) 17–24.

[64] M.W. Barsoum, T. El-Raghy, M. Ali, Processing and characterization of Ti_2AlC, Ti_2AlN, and $Ti_2AlC_{0.5}N_{0.5}$, Metallurgical and Materials Transactions A. 31 (2000) 1857–1865.

[65] X. Wang, Y. Zhou, Solid-Liquid Reaction Synthesis and Simultaneous Densification of Polycrystalline Ti_2AlC, Zeitschrift Für Metallkunde. 93 (2002) 66–71.

[66] W. Son, T. Duong, A. Talapatra, E. Prehn, Z. Tan, M. Radovic, R. Arróyave, Minimal effect of stacking number on intrinsic cleavage and shear behavior of $Ti_{n+1}AlC_n$ and $Ta_{n+1}AlC_n$ MAX phases, Journal of Applied Physics. 123 (2018)

225102.

[67] I.-H. Song, D.K. Kim, Y.-D. Hahn, H.-D. Kim, Investigation of Ti_3AlC_2 in the in situ TiC–Al composite prepared by the exothermic reaction process in liquid aluminum, Materials Letters. 58 (2004) 593–597.

[68] M. Radovic, M.W. Barsoum, T. El-Raghy, S.M. Wiederhorn, Tensile creep of coarse-grained Ti_3SiC_2 in the 1000–1200 °C temperature range, Journal of Alloys and Compounds. 361 (2003) 299–312.

[69] D.E. Hajas, M. to Baben, B. Hallstedt, R. Iskandar, J. Mayer, J.M. Schneider, Oxidation of Cr_2AlC coatings in the temperature range of 1230 to 1410 °C, Surface and Coatings Technology. 206 (2011) 591–598.

[70] J.C. Schuster, H. Nowotny, INVESTIGATIONS OF THE TERNARY SYSTEMS (Zr, Hf, Nb, Ta)-Al-C AND STUDIES ON COMPLEX CARBIDES., Zeitschrift Fuer Metallkunde/Materials Research and Advanced Techniques. 71 (1980) 341–346.

[71] I. Salama, M.W. Barsoum, Synthesis and mechanical properties of Nb_2AlC and $(Ti,Nb)_2AlC$, Journal of Alloys and Compounds. 347 (2002) 271–278.

[72] W. Zhang, N. Travitzky, C. Hu, Y. Zhou, P. Greil, Reactive hot pressing and properties of Nb_2AlC, Journal of the American Ceramic Society. 92 (2009) 2396–2399.

[73] C.L. Yeh, C.W. Kuo, An investigation on formation of Nb_2AlC by combustion synthesis of Nb_2O_5-Al-Al_4C_3 powder compacts, Journal of Alloys and Compounds. 496 (2010) 566–571.

[74] W. Zhou, K. Li, J. Zhu, S. Tian, Rapid synthesis of highly pure Nb_2AlC using the spark plasma sintering technique, Journal of Physics and Chemistry of Solids. 120 (2018) 218–222.

[75] N. Shahin, S. Kazemi, A. Heidarpour, Mechanochemical synthesis mechanism of Ti_3AlC_2 MAX phase from elemental powders of Ti, Al and C, Advanced Powder Technology. 27 (2016) 1775–1780.

[76] X. Duan, L. Shen, D. Jia, Y. Zhou, S. van der Zwaag, W.G. Sloof, Synthesis of high-purity, isotropic or textured Cr_2AlC bulk ceramics by spark plasma sintering of pressure-less sintered powders, Journal of the European Ceramic Society. 35 (2015) 1393–1400.

[77] I. Salama, T. El-Raghy, M.W. Barsoum, Oxidation of Nb_2AlC and $(Ti,Nb)_2AlC$ in air, Journal of The Electrochemical Society. 150 (2003) 152–158.

[78] C. Hu, Y. Sakka, H. Tanaka, T. Nishimura, S. Grasso, Low temperature thermal expansion, high temperature electrical conductivity, and mechanical properties of Nb_4AlC_3 ceramic synthesized by spark plasma sintering, Journal of Alloys and Compounds. 487 (2009) 675–681.

[79] C. Magnus, W.M. Rainforth, Spark plasma sintering (SPS) synthesis and tribological behaviour of MAX phase composite of the family $Ti_{n+1}SiC_n$ (n = 2), Wear. 438–439 (2019) 203062.

[80] L. Hu, A. Kothalkar, G. Proust, I. Karaman, M. Radovic, Fabrication and characterization of $NiTi/Ti_3SiC_2$ and $NiTi/Ti_2AlC$ composites, Journal of Alloys and Compounds. 610 (2014) 635–644.

[81] H. Gao, R. Benitez, W. Son, R. Arroyave, M. Radovic, Structural, physical and mechanical properties of $Ti_3(Al_{1-x}Si_x)C_2$ solid solution with x=0–1, Materials Science and Engineering A. 676 (2016) 197–208.

[82] O. Guillon, J. Gonzalez-Julian, B. Dargatz, T. Kessel, G. Schierning, J. Räthel, M. Herrmann, Field-assisted sintering technology/spark plasma sintering: Mechanisms, materials, and technology developments, Advanced Engineering Materials. 16 (2014) 830–849.

[83] Z.A. Munir, U. Anselmi-Tamburini, M. Ohyanagi, The effect of electric field and pressure on the synthesis and consolidation of materials: A review of the spark plasma sintering method, Journal of Materials Science. 41 (2006) 763–777.

[84] R. Orrù, R. Licheri, A.M. Locci, A. Cincotti, G. Cao, Consolidation/synthesis of materials by electric current activated/assisted sintering, Materials Science and Engineering: R: Reports. 63 (2009) 127–287.

[85] R. Marder, C. Estournès, G. Chevallier, R. Chaim, Numerical model for sparking and plasma formation during spark plasma sintering of ceramic compacts, Journal of Materials Science. 50 (2015) 4636–4645.

[86] M. Radovic, E. Lara-Curzio, L. Riester, Comparison of different experimental techniques for determination of elastic properties of solids, Materials Science and Engineering A. 368 (2004) 56–70.

[87] K. Flynn, M. Radovic, Evaluation of defects in materials using resonant ultrasound spectroscopy, Journal of Materials Science. 46 (2011) 2548–2556.

[88] P. Gudlur, A. Forness, J. Lentz, M. Radovic, A. Muliana, Thermal and mechanical

properties of Al/Al_2O_3 composites at elevated temperatures, Materials Science and Engineering: A. 531 (2012) 18–27.

[89] A. Migliori, J.L. Sarrao, Resonant ultrasound spectroscopy : applications to physics, materials measurements, and nondestructive evaluation, Wiley, New York, NY, 1997.

[90] D.W. Hetzner, Microindentation Hardness Testing of Materials Using ASTM E384, Microscopy and Microanalysis. 9 (2003) 708–709.

[91] M.T. Agne, M. Radovic, G.W. Bentzel, M.W. Barsoum, Stability of V_2AlC with Al in 800-1000 °C temperature range and in situ synthesis of V_2AlC/Al composites, Journal of Alloys and Compounds. 666 (2016) 279–286.

[92] R. Benitez, W.H. Kan, H. Gao, M. O'Neal, G. Proust, A. Srivastava, M. Radovic, Mechanical properties and microstructure evolution of Ti_2AlC under compression in 25–1100 °C temperature range, Acta Materialia. 189 (2020) 154–165.

[93] C.L. Yeh, Y.G. Shen, Effects of Al content on formation of Ta_2AlC by self-propagating high-temperature synthesis, Journal of Alloys and Compounds. 482 (2009) 219–223.

[94] C. Hu, J. Zhang, Y. Bao, J. Wang, M. Li, Y. Zhou, In-situ reaction synthesis and decomposition of Ta_2AlC, International Journal of Materials Research. 99 (2008) 8–13.

[95] C. Hu, F. Li, L. He, M. Liu, J. Zhang, J. Wang, Y. Bao, J. Wang, Y. Zhou, In Situ Reaction Synthesis, Electrical and Thermal, and Mechanical Properties of Nb_4AlC_3, Journal of the American Ceramic Society. 91 (2008) 2258–2263.

[96] J. Wang, Y. Zhou, Dependence of elastic stiffness on electronic band structure of nanolaminate M_2AlC (M=Ti,V,Nb, and Cr) ceramics, Physical Review B - Condensed Matter and Materials Physics. 69 (2004) 1–9.

[97] M.W. Barsoum, L. Farber, T. El-Raghy, Dislocations, kink bands, and room-temperature plasticity of Ti_3SiC_2, Metallurgical and Materials Transactions A. 30 (1999) 1727–1738.

[98] J.M. Molina-Aldareguia, J. Emmerlich, J.-P. Palmquist, U. Jansson, L. Hultman, Kink formation around indents in laminated Ti_3SiC_2 thin films studied in the nanoscale, Scripta Materialia. 49 (2003) 155–160.

[99] S. Basu, N. Obando, A. Gowdy, I. Karaman, M. Radovic, Long-Term Oxidation of Ti_2AlC in Air and Water Vapor at 1000–1300°C Temperature Range, Journal of The Electrochemical Society. 159 (2011) 90–96.

[100] M. Radovic, M.W.W. Barsoum, A. Ganguly, T. Zhen, P. Finkel, S.R.R. Kalidindi, E. Lara-Curzio, On the elastic properties and mechanical damping of Ti_3SiC_2, Ti_3GeC_2, $Ti_3Si_{0.5}Al_{0.5}C_2$ and Ti_2AlC in the 300-1573 K temperature range, Acta Materialia. 54 (2006) 2757–2767.

[101] P. Gudlur, A. Forness, J. Lentz, M. Radovic, A. Muliana, Thermal and mechanical properties of Al/Al_2O_3 composites at elevated temperatures, Materials Science and Engineering: A. 531 (2012) 18–27.

[102] P. Naik Parrikar, R. Benitez, H. Gao, M. Radovic, A. Shukla, The Effect of Grain Size on Deformation and Failure of Ti_2AlC MAX Phase under Thermo-Mechanical Loading, Experimental Mechanics 2017 57:5. 57 (2017) 675–685.

[103] D. Sauceda, P. Singh, A.R. Falkowski, Y. Chen, T. Doung, G. Vazquez, M. Radovic, R. Arroyave, High-throughput reaction engineering to assess the oxidation stability of MAX phases, Npj Computational Materials. 7 (2021) 1–13.

[104] Z. Zhan, Y. Chen, M. Radovic, A. Srivastava, Non-classical crystallographic slip in a ternary carbide - Ti_2AlC, Mater. Res. Lett. 8 (2020) 275–281.

[105] Z. Sun, S. Li, R. Ahuja, J.M. Schneider, Calculated elastic properties of M_2AlC (M = Ti, V, Cr, Nb and Ta), Solid State Communications. 129 (2004) 589–592.

[106] M. Barsoum, I. Salama, T. El-Raghy, J. Golczewski, H. Seifert, F. Aldinger, W. Porter, H. Wang, Thermal and electrical properties of Nb_2AlC, $(Ti,Nb)_2AlC$ and Ti_2AlC, Metallurgical and Materials Transactions A. 33 (2002) 2775–2779.

[107] G.W. Bentzel, N.J. Lane, S.C. Vogel, K. An, M.W. Barsoum, E.N. Caspi, A high-temperature neutron diffraction study of Nb_2AlC and TiNbAlC, Journal of the American Ceramic Society. 98 (2015) 940–947.

[108] R. Benitez, H. Gao, M. O'Neal, P. Lovelace, G. Proust, M. Radovic, Effects of microstructure on the mechanical properties of Ti_2AlC in compression, Acta Materialia. 143 (2018) 130–140.

[109] Z.-Z. Yang, E.R. Davidson, Evaluation of a Characteristic Atomic Radius by an Ab Initio Method, Int. Journal of Quantum Chemistry. 62 (1997) 47–53.

[110] G. Bergerhoff, R. Hundt, R. Sievers, I.D. Brown, The Inorganic Crystal Structure Data Base, Journal of Chemical Information and Computer Sciences. 23 (1983) 66–69.

[111] K.T. Jacob, S. Raj, L. Rannesh, Vegard's law: A fundamental relation or an

approximation, Materials Research and Advanced Techniques. 98 (2007) 776–779.

[112] H. Gao, R. Benitez, W. Son, R. Arroyave, M. Radovic, Structural, physical and mechanical properties of $Ti_3(Al_{1-x}Si_x)C_2$ solid solution with x=0–1, Materials Science and Engineering A. 676 (2016) 197–208.

[113] T. Cabioc'h, P. Eklund, V. Mauchamp, M. Jaouen, Structural investigation of substoichiometry and solid solution effects in $Ti_2Al(C_x,N_{1-x})_y$ compounds, Journal of the European Ceramic Society. 32 (2012) 1803–1811.

[114] T.H. Scabarozi, Combinatorial investigation of nanolaminate ternary carbide thin films, Drexel University, 2009.

[115] C.L. Yeh, W.J. Yang, Combustion Synthesis of $(Ti,V)_2AlC$ Solid Solutions, Advanced Materials Research. 909 (2014) 19–23.

[116] S. Gupta, M.W. Barsoum, Synthesis and Oxidation of V_2AlC and $(Ti_{0.5}V_{0.5})_2AlC$ in Air, Journal of The Electrochemical Society. 151 (2004) 24–29.

[117] B. Cordero, V. Gómez, A.E. Platero-Prats, M. Revés, J. Echeverría, E. Cremades, F. Barragán, S. Alvarez, Covalent radii revisited, Journal of the Chemical Society. Dalton Transactions. (2008) 2832–2838.

[118] X. He, Y. Bai, C. Zhu, Y. Sun, M. Li, M.W. Barsoum, General trends in the structural, electronic and elastic properties of the M_3AlC_2 phases (M = transition metal): A first-principle study, Computational Materials Science. 49 (2010) 691–698.

[119] A.S. Ingason, A. Mockute, M. Dahlqvist, F. Magnus, S. Olafsson, U.B. Arnalds, B. Alling, I.A. Abrikosov, B. Hjörvarsson, P.O.Å. Persson, J. Rosen, Magnetic Self-

Organized Atomic Laminate from First Principles and Thin Film Synthesis, Physical Review Letters. 110 (2013) 195502.

[120] N. Ouabadi, V. Gauthier-Brunet, T. Cabioc'h, G.-P. Bei, S. Dubois, Y. Zhou, Formation Mechanisms of Ti_3SnC_2 Nanolaminate Carbide Using Fe as Additive, Journal of the American Ceramic Society. 96 (2013) 3239–3242.

[121] T. Lapauw, B. Tunca, T. Cabioc 'h C, J. Vleugels, K. Lambrinou, Reactive spark plasma sintering of Ti_3SnC_2 , Zr_3SnC_2 and Hf_3SnC_2 using Fe, Co or Ni additives, Journal of the European Ceramic Society. 37 (2017) 4539–4545.

[122] S. Lin, Y. Huang, L. Zu, X. Kan, J. Lin, W. Song, P. Tong, X. Zhu, Y. Sun, Alloying effects on structural, magnetic, and electrical/thermal transport properties in MAX-phase $Cr_{2-x}M_xGeC$ (M= Ti, V, Mn, Fe, and Mo), Journal of Alloys and Compounds. 680 (2016) 452–461.

[123] C.M. Hamm, J.D. Bocarsly, G. Seward, U.I. Kramm, C.S. Birkel, Non-conventional synthesis and magnetic properties of MAX phases $(Cr/Mn)_2AlC$ and $(Cr/Fe)_2AlC$, J. Mater. Chem. C. 5 (2017) 5700–5708.

[124] C.C. Lai, A. Petruhins, J. Lu, M. Farle, L. Hultman, P. Eklund, J. Rosen, Thermally induced substitutional reaction of Fe into Mo_2GaC thin films, Materials Research Letters. 5 (2017) 533–539.

[125] G. Kresse, J. Hafner, Ab initio molecular dynamics for liquid metals, Physical Review B. 47 (1993) 558–561.

[126] D. Joubert, From ultrasoft pseudopotentials to the projector augmented-wave method, Physical Review B - Condensed Matter and Materials Physics. 59 (1999)

1758–1775.

[127] A. Van De Walle, P. Tiwary, M. De Jong, D.L. Olmsted, M. Asta, A. Dick, D. Shin, Y. Wang, L.Q. Chen, Z.K. Liu, Efficient stochastic generation of special quasirandom structures, Calphad: Computer Coupling of Phase Diagrams and Thermochemistry. 42 (2013) 13–18.

[128] J.P. Perdew, K. Burke, M. Ernzerhof, Generalized gradient approximation made simple, Physical Review Letters. 77 (1996) 3865–3868.

[129] M. Hossein-Zadeh, O. Mirzaee, H. Mohammadian-Semnani, M. Razavi, Microstructure investigation of V_2AlC MAX phase synthesized through spark plasma sintering using two various sources V and V_2O_5 as the starting materials, Ceramics International. 45 (2019) 23902–23916.

[130] L. Vegard, Die Konstitution der Mischkristalle und die Raumfüllung der Atome, Zeitschrift Für Physik. 5 (1921) 17–26.

[131] W. Jeitschko, H. Nowotny, F. Benesovsky, Kohlenstoffhaltige ternäre Verbindungen (H-Phase), Monatshefte Für Chemie. 94 (1963) 672–676.

[132] K. V. Sobolev, K.K. Kolincio, A. Emelyanov, A. Mielewczyk-Gryń, M. Gazda, M. Roman, A. Pazniak, V. Rodionova, Evolution of magnetic and transport properties in $(Cr_{1-x}Mn_x)_2AlC$ MAX-phase synthesized by arc melting technique, Journal of Magnetism and Magnetic Materials. 493 (2020) 165642.

[133] D. Pinek, T. Ito, M. Ikemoto, K. Yaji, M. Nakatake, S. Shin, T. Ouisse, Unified description of the electronic structure of M_2AC nanolamellar carbides, PHYSICAL REVIEW B. 100 (2019) 75144.

[134] P. Singh, D. Sauceda, R. Arroyave, The effect of chemical disorder on defect formation and migration in disordered max phases, Acta Materialia. 184 (2020) 50–58.

[135] F.L. Meng, Y.C. Zhou, J.Y. Wang, Strengthening of Ti_2AlC by substituting Ti with V, Scripta Materialia. 53 (2005) 1369–1372.

[136] M.W. Barsoum, T. El-Raghy, M. Ali, Processing and characterization of Ti_2AlC, Ti_2AlN, and $Ti_2AlC_{0.5}N_{0.5}$, Metallurgical and Materials Transactions A 2000 31:7. 31 (2000) 1857–1865.

[137] L. Cai, Z. Huang, W. Hu, Y. Chen, Z. Tan, M. Radovic, Effects of Al substitution with Si and Sn on tribological performance of Ti_3AlC_2, Ceramics International. 47 (2021) 6352–6361.

[138] C. Koch, Determination of core structure periodicity and point defect density along dislocations, Arizona State University, 2002.

[139] H. Holleck, F. Thümmler, Ternäre Komplex-carbide, -nitride, Berg- u. Hüttenm. Mh. 110 (1965) 171–172.

[140] E. Reiffenstein, H. Nowotny, F. Benesovsky, Einige neue η-Carbide, Monatshefte Für Chemie Und Verwandte Teile Anderer Wissenschaften. 96 (1965) 1543–1546.

[141] H. Holleck, F. Thümmler, Ternäre Komplex-carbide,-nitride und-oxide mit teilweise aufgefüllter Ti_2Ni-Struktur, Monatshefte Für Chemie/Chemical Monthly. 98 (1967) 133–134.

[142] K. Momma, F. Izumi, IUCr, VESTA 3 for three-dimensional visualization of crystal, volumetric and morphology data, Journal of Applied Crystallography. 44

(2011) 1272–1276.

[143] B. Systems, C-Fe-Nb (Carbon-Iron-Niobium), Journal of Phase Equilibria. 24 (2003) 57–61.

[144] F. Stein, C. He, O. Prymak, S. Voß, I. Wossack, Phase equilibria in the Fe-Al-Nb system: Solidification behaviour, liquidus surface and isothermal sections, Intermetallics. 59 (2015) 43–58.

[145] L. Eleno, K. Frisk, A. Schneider, Assessment of the Fe-Ni-Al system, Intermetallics. 14 (2006) 1276–1290.